ON THE RESPONSE OF THE UPPER ATMOSPHERE TO SOLAR FLARES

by

David J. Pawlowski

A dissertation submitted in partial fulfillment
of the requirements for the degree of
Doctor of Philosophy
(Space and Planetary Physics)
in The University of Michigan
2009

Doctoral Committee:

Associate Professor Aaron J. Ridley, Chair
Professor Dennis S. Bernstein
Professor Stephen W. Bougher
Professor Andrew Nagy

© David J. Pawlowski 2009
All Rights Reserved

ACKNOWLEDGEMENTS

Perhaps the most important key to success for a graduate student, or any young scientist for that matter, is to have mentors, advisors, and instructors who have both an extensive knowledge of the fields and methods pertinent to the students research, as well as the skills and desire to share such knowledge. As one of these students, I could not have been more fortunate throughout my studies at the University of Michigan, where not only do my advisor, Professor Aaron J. Ridley, and dissertation committee members, Professors Dennis S. Bernstein, Andrew F. Nagy, and Stephen W. Bougher possess these qualities, so do all of the faculty who have guided me either through course work, or through interaction in other ways, be it meetings, discussions, or personal communication. The guidance provided here, at all levels, provides students with every opportunity to be successful in their endeavors as scientists. Being a part of the Atmospheric, Oceanic, and Space Sciences community, as well as the greater College of Engineering community, has been, and will continue to be, a great privilege.

I would like to express a great deal of appreciation towards Professor Ridley for his role as my advisor. He has a great deal of knowledge that has greatly contributed to all of my studies. In addition, his confidence and motivation are contagious, and have helped me succeed at times when I thought I might not. Prof. Ridley's understanding of the times that it is best to let me work independently vs. when it is appropriate to more actively advise, is perhaps his greatest quality as an advisor, and has prepared me well for the next steps in my career as a scientist.

I would like to also, again, acknowledge my other dissertation committee mem-

bers, Professors Bernstein, Nagy and Bougher. Their comments and suggestions have significantly improved my thesis. A great deal of thanks also goes to K.C. Hansen, Darren DeZeeuw, Mike Liemohn, Gabor Toth, and Tamas Gombosi for support on everything from computational issues to the correct sizing of power point graphics, as well as all of the administrative support from Jan Beltran, Genel Frye, Margaret Reid and Sue Griffin, who have helped me go through 4 years of graduate school without purchasing a single 3-ring binder. In addition, Jerry Keeler and Joyce Penner have provided me with many tools to use in the future as an instructor of university level courses.

My success as a graduate student would not have been possible without the tremendous amount of support from a long list of current and past graduate students, many from other institutions, including, Yiqun Yu, Yue Deng, Amanda Brecht, Tami McDunn, Arnoud Valeille, Dan Welling, Raluca Ilie, Dalal Najib, Matt Trantham, Alex Glocer, Ofer Cohen, Lynne Gratz, Tyler Cornelius, and Mike Christensen, to name a few, who have all had an influence on the science, technique, or motivation that went into this thesis. I would also like to thank my parents, Dan and Linda, as well as my sister, Lauren, who have always tried so hard to understand my response when they ask the question, "what are you working on?"

Finally, thank you to my wife, Lindsay, for more than 11 years of support, so that I can finally be finished with college. Lindsay is always first and foremost concerned that I use my life in a way that makes me happy, and has never found fault in my many transitions between fields of study. I think she finally realized that I knew, for sure, what I would be doing with my life when she decided we would have kids, and that at the time, the impending birth of our first child would provide me with the motivation to finish my Ph. D.

TABLE OF CONTENTS

LIST OF FIGURES

Figure

LIST OF TABLES

ABSTRACT

ON THE RESPONSE OF THE UPPER ATMOSPHERE TO SOLAR FLARES

by

David J. Pawlowski

Chair: Aaron J. Ridley

Over the past several decades, modern civilizations have become increasingly dependent on spacecraft that reside in the near-Earth space environment. For this reason, scientists and engineers have been interested in understanding the causes of perturbations to the background state of the Earth's upper atmosphere, and to quantify the impact of these events. As a result of the states of the thermosphere and ionosphere being directly dependent on the incident radiation from the sun, it is expected that sudden changes in the solar radiative output should cause significant changes in the upper atmosphere. Such dynamics are investigated in this study, specifically the manner in which solar flares affect the density, circulation, and temperature of the Earth's thermosphere and ionosphere. A global model of this region is used to examine how the upper atmosphere responds to such transient events. In order to quantify the response, the model is run during realistic events in order to understand the magnitudes of the resulting perturbations to the global ionosphere-thermosphere system. In the thermosphere, density perturbations of approximately 15% are found to occur on the dayside within 1.5 hours after the start of a solar flare. The addition of solar energy to the dayside launches a traveling atmospheric disturbance which propagates

towards the night-side at the local sound speed plus the background velocity. As the disturbance converges on itself near the midnight sector, density enhancements almost as large as those seen on the day-side can occur. Furthermore, these night-side neutral perturbations cause both enhancements and depletions in the night-side electron density.

In addition, theoretical simulations are performed to study the effects that the major characteristics of solar flares have on the atmosphere. In particular, dynamics resulting from changes in the total integrated energy, flare magnitude, and relevant time scales are investigated. The most important characteristic in determining the thermospheric response is the total integrated energy, since it is linearly correlated to both the global average and global maximum thermospheric density perturbation. Also, the peak flare magnitude has a strong influence on the maximum day-side response, though not the global average perturbation. Finally, as a consequence of the slow response of thermospheric cooling processes to the additional energy being absorbed, the flare decay time is the most important factor in determining the time of the maximum global average density response in the thermosphere.

CHAPTER I

Introduction

In 1901, Gulglielmo Marconi succeeded in transmitting the first trans-Atlantic radio signals. The idea that the deflection of radio waves around the Earth is caused by an ionized layer of the Earth's upper atmosphere which is formed by the absorption of incident solar extreme ultraviolet radiation was suggested less than a year later. At that point, in all but name, the ionosphere had been discovered. This discovery marked the beginning of a profound interest in the ionosphere, as well as the overlapping neutral atmosphere, or thermosphere, that affects it.

Since the beginning of the 20^{th} century, the number of technologies that have been developed which enable scientists to study the upper atmosphere is staggering. Measurements made by rockets, satellites, ground based radars and cameras, have all lead to a thorough knowledge of the large-scale features of the upper atmosphere. Enough data have been collected to produce empirical models that can crudely estimate the state of the thermosphere and ionosphere under almost any combination of circumstances. The invention of the computer has allowed scientists to examine the fundamental physics governing this region, and to develop high-resolution global models to self-consistently predict the dynamics of the system. Also, smaller scale models have been used to examine local processes in great detail. Yet, since modern civilizations have become increasingly reliant on Earth orbiting spacecraft for tech-

nologies such as communications and navigation in the past several decades, the need for further understanding of the upper atmosphere continues to grow. Scientists are now more than ever interested in the effect that transient features have on the system. An understanding of the manner in which the thermosphere behaves under dynamic forcing is important, not only because of the influence the neutral atmosphere has on the ionosphere, but also because changes in the thermosphere can directly affect the drag experienced by an Earth orbiting satellite, making satellite tracking and velocity prediction extremely difficult. In addition, perturbations in the state of the ionosphere can lead to problems such as significant degradation of GPS signals and an inability to communicate at great distances.

1.1 Earth's atmosphere

Since the 1960s, studies of the thermosphere have resulted in a fairly complete knowledge of the climatology of the entire atmosphere. The variations in temperature with altitude suggest that the atmosphere can be broken up into distinct regions, the troposphere, stratosphere, mesosphere, thermosphere and ionosphere, each dominated by different processes. Figure 1.1 shows the vertical temperature structure of Earth's atmosphere. The troposphere is the lowest part of the atmosphere and resides from the surface to roughly 10 km. In this region, the solar radiation that reaches and is absorbed by the surface is re-radiated at infrared wavelengths. This causes the temperature to be highest at the surface and to steadily decline as altitude increases. Because of this, the atmosphere is unstable, and therefore, this region of the atmosphere experiences what is historically referred to as weather. Above the tropopause exists a layer of ozone molecules that absorb any solar ultraviolet radiation that reaches this far down into the atmosphere. The absorbed energy breaks up these molecules and in the process, adds heat to this region of the atmosphere, resulting in an increase in temperature. At about 45 km the temperature maximizes

at the stratopause, and again begins to decrease throughout the mesosphere due to the relatively low amount of absorption of solar radiation. The base of the thermosphere occurs at roughly 90 km, where the temperature again begins to increase as a result of the absorption of photons. Below about 500 km, the Earth's atmosphere is still considered to be a collisional medium. This means that for a given particle, the probability that it will encounter a collision with another particle is greater than 1. Above this altitude, this probability falls off, and the particles tend to follow ballistic trajectories. This region of the atmosphere is called the exosphere, and plays an important role in determining atmospheric escape (*Jeans*, 1925; *Tinsley et al.*, 1986).

The ionosphere is the electrically charged part of the atmosphere that overlaps the thermosphere. In the ionosphere, free electron-ion pairs exist. Because of different processes that create and transport the electrons and ions, the ionosphere can be broken up into several regions based on where local maxima in the electron density occur. The right side of Figure 1.1 shows a typical altitude profile of the electron density, which consists of the D, E, F1 and F2 regions.

Within the Earth, motion of the liquid outer core is responsible for the production of a strong dynamo magnetic field that extends deep into the near-Earth space environment. Close to the Earth, the magnetic field can be approximated by a dipole field located near the center of the Earth, with the north–south axis slightly offset from the rotational axis of the Earth. This magnetic field acts as a barrier to the sun's expanding atmosphere, or the solar wind, and the interaction between the solar wind and the field results in a tear-drop shaped cavity that surrounds the Earth called the magnetosphere. Furthermore, this interaction causes the existence of several current systems and particle populations that in turn may interact with the upper atmosphere. Figure 1.2 shows a sketch of the inner magnetosphere, along with some of the major current systems.

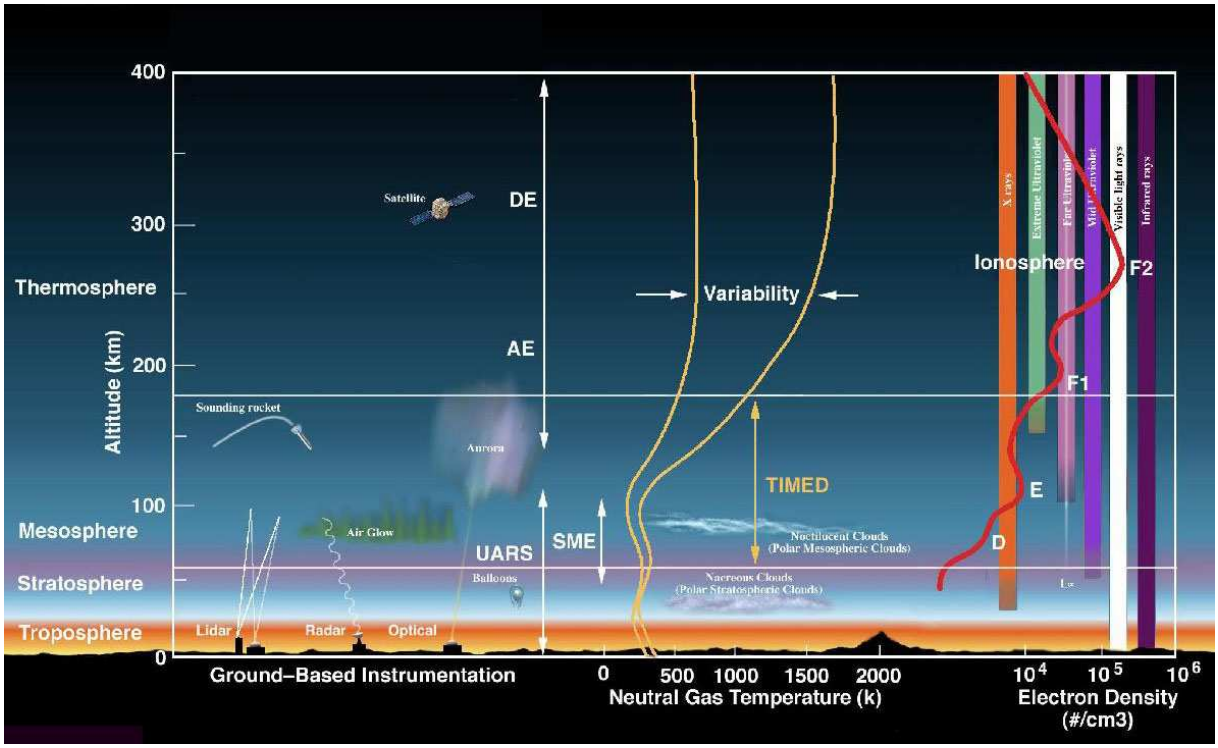

Figure 1.1: The different regions of the Earth's atmosphere along with the temperature and electron density altitude profiles. The solid bars on the right illustrate the penetration depths of different regions of the solar spectrum. Courtesy of the Center for Space Weather Modeling.

1.1.1 General structure of the thermosphere

The thermosphere extends from approximately 90 km up to about 500 km. The temperature in the lower thermosphere increases up to an altitude of 250 km due to the absorption of solar radiation in the soft X-ray and extreme ultraviolet (EUV) wavelengths (.1-200 nm, Figure 1.3). At higher altitudes, the gas is so rarefied that there is very little absorption of solar radiation. In addition, thermal conduction is very efficient due to the high temperatures, and as such, the temperature becomes constant with altitude. This temperature is highly dependent on solar activity level and can range from around 1000 K to more than 2000 K.

One of the basic assumptions made about the thermosphere is that it generally is in a state of hydrostatic equilibrium. This implies that the force due to gravity is

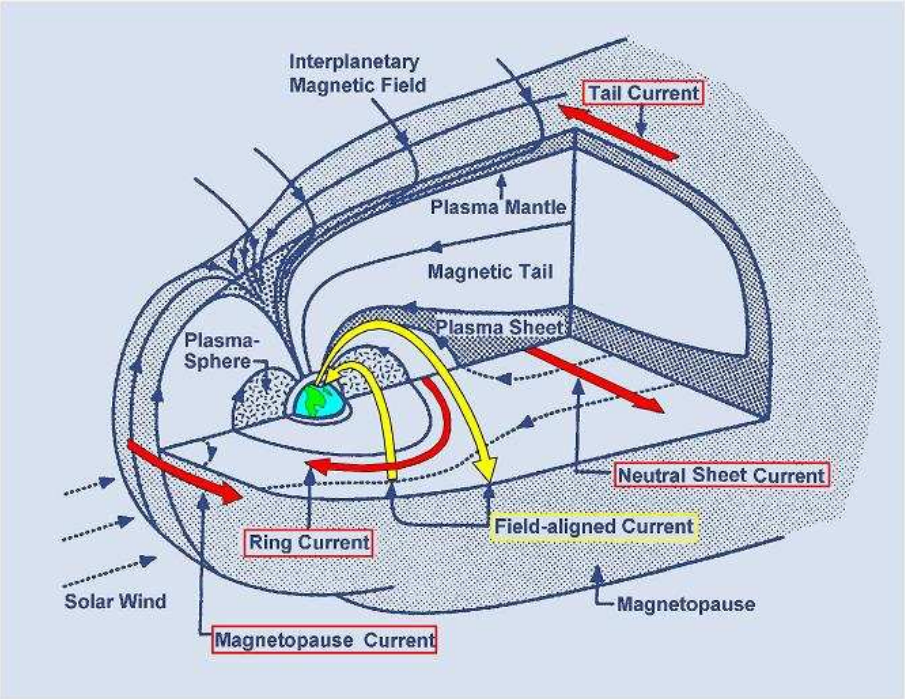

Figure 1.2: Sketch of the inner magnetosphere along with the major current systems (*Kivelson and Russell*, 1995).

balanced by the pressure gradient force in the vertical direction. In other words, the vertical momentum equation can be written as:

$$\rho g = -\nabla P, \tag{1.1}$$

where ρ is the mass density, g is the acceleration due to gravity, and P is the pressure. The pressure can be written as:

$$P = nkT, \tag{1.2}$$

where n is the number density, $k = 1.38e^{-23} J/K$ is Boltzmann's constant, and T is the temperature, and therefore the solution to 1.1 is

$$n(z) = n_0 exp(\frac{z - z_0}{H}), \tag{1.3}$$

where $H = \frac{KT}{\overline{m}g}$ is the neutral scale height, z is altitude, n_0 is a reference density

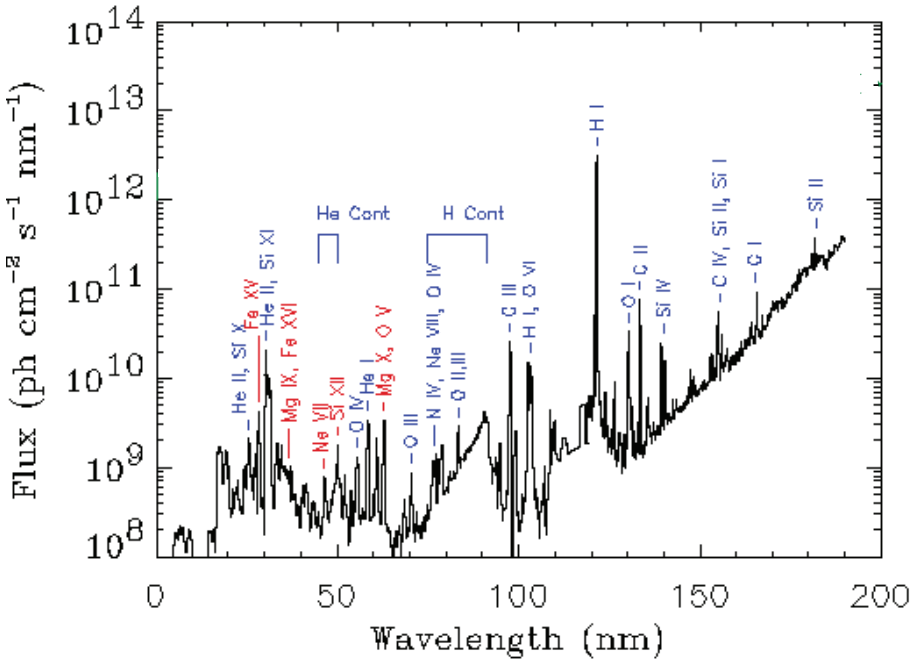

Figure 1.3: The solar extreme ultraviolet spectrum (0 – 200 nm) and the sources of some of the dominate lines. Courtesy of Laboratory of Solar Physics.

taken at reference altitude z_0, and $\overline{m}$ is the number density weighted mass . The scale height corresponds to the distance at which the density decreases by a factor of e^1. Equation 1.3 indicates that while the density falls off exponentially with altitude, the rate at which it does so is determined by the temperature, mass, and gravity.

Compositionally, the major chemical species at the base of the thermosphere are molecular nitrogen and molecular oxygen, and to a lesser degree, atomic oxygen. Nitric oxide and atomic nitrogen are also present in smaller quantities, but are important because of their involvement in chemical reactions with the major species. In the lower thermosphere, the atmosphere is still considered to be well mixed (*Fuller-Rowell and Rees*, 1992) and chemical transport is dominated by eddy diffusion. This means that while the total mass density decays with altitude, the mixing ratios of the individual species remains constant. Above the homopause (between 110 and 120 km (*Blum and Schuchardt*, 1978; *Hall et al.*, 2008)), the eddy diffusive regime gives way to a molecular diffusive regime, in which each of the species decays vertically

according to their own scale height:

$$H_s = \frac{kT_s}{m_s g}, \tag{1.4}$$

where the subscript, s, denotes the individual species. Since the scale height is dependent on the molecular weight of the species, m_s, the heavier molecules tend to decay faster with altitude than the light species. This results in a transition from a molecular dominated lower thermosphere, where N_2 is the main constituent, to an atomic dominated middle and upper thermosphere, where atomic oxygen is the main constituent, which generally occurs near the 200 km level.

1.1.2 Thermospheric energy sources and losses

The main source of energy to the upper atmosphere is the sun. Solar radiation in the EUV wavelengths is absorbed from 90 - 200 km, and as the radiation enters the Earth's atmosphere, it is attenuated by the presence of an absorbing medium depending on the absorption cross section for a given wavelength and species. As the photons coming down into the thermosphere pass through more gas, there are progressively fewer photons that can penetrate to lower altitudes. Therefore, at a given altitude, the total amount of absorbed radiation is dependent on the intensity at the top of the atmosphere and the integral of the density times the absorption cross section from the given altitude to the top of the atmosphere (*Chapman*, 1931). This integral is known as the optical depth, or τ, and it is important because it gives an indication as to the altitude where the most amount of energy is being absorbed. Essentially, this occurs where there is a balance between the number of absorbing particles and the remaining solar intensity. Typically, a reference value of $\tau = 1$ indicates the altitude at which most of the solar energy is being deposited. The optical depth is a function of wavelength, thus the total intensity at a given altitude

is a function of altitude, solar zenith angle, wavelength, and, since the absorbtion cross sections are dependent on them, the species.

When the radiation is absorbed, it can lead to either the breaking apart of a neutral molecule (photodissociation), the removal of an electron from a neutral atom or molecule (ionization), or excitation of the neutral or ion particle (photo-excitation). In general, the incident photon has more energy than the amount required to perform the dissociation or ionization. In the case of ionization, the excess energy is taken by the newly released electron. Depending on the remaining energy, this photoelectron is now able to further dissociate or ionize the gas, or, through columb interactions, the energy can be transported to the thermal electrons, and further, to the ions. Eventually, some of this energy is transferred to the neutrals via ion–neutral collisions.

When the initial photon dissociates a neutral molecule, the excess energy is again able to take a number of paths. In some cases, this energy simply goes into heating of the neutral gas. In others, this energy results in one or more of the products of the dissociation to be in an excited state. These excited species can then spontaneously emit a photon. This phenomenon is referred to as airglow. On the other hand, the excited particle can loose its energy via quenching, or a collision with another particle. In this case, the energy is taken up in the form of heating of the neutral gas.

The manner in which energy from the absorption of solar radiation trickles down through various channels, ultimately being deposited into neutral heating is quite complicated. *Torr et al.* (1980) performed a detailed study of this transport of energy for different solar conditions. Figure 1.4 shows the major energy loss process for the solar input. In the lower thermosphere, not only is O_2 directly dissociated by the incoming Schumann-Runge continuum radiation, but in addition, every ionization leads to a dissociation of an O_2 molecule. For this reason, a significant portion of the total incident EUV energy goes into dissociation of O_2. At higher altitudes, much of the absorbed solar energy is either re-radiated away in the form of airglow, or

transfered from the photoelectrons to the thermal electrons. As mentioned above, collisions between the electrons and ions, and subsequently, ions and neutrals provide a path for some of this energy to contribute to neutral heating. Ultimately, the

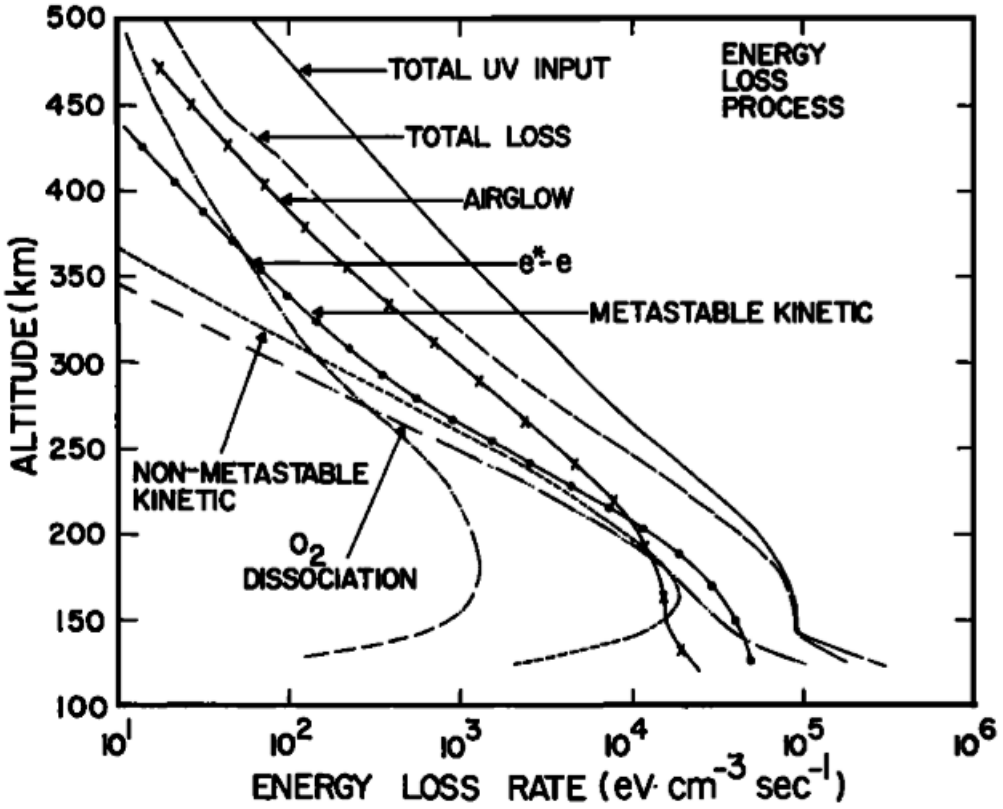

Figure 1.4: Altitude profile of the major loss processes for solar EUV radiation incident on the thermosphere. (*Torr et al.*, 1980).

photodissociation and photoionization processes result in the formation of reactive species which can then interact with the background gas. The subsequent exothermic chemical reactions that become possible are one of the most important sources of heat to the thermosphere. In Figure 1.4, these processes are denoted by the non-metastable kinetic line, which are reactions that involve only ground state reactants, and the metastable kinetic line.

The main result of the *Torr et al.* (1980) study is the use of this analysis to produce a neutral heating efficiency, or the ratio of the amount of energy that goes into heating of the neutral gas to the total incident solar energy. Altitude profiles of

the heating efficiency are shown in Figure 1.5 for solar minimum and solar maximum conditions. This ratio allows for the prediction of the amount of neutral heating for realistic events based only on a knowledge of the incident solar spectrum, enabling scientists to calculate the neutral temperature in the thermosphere.

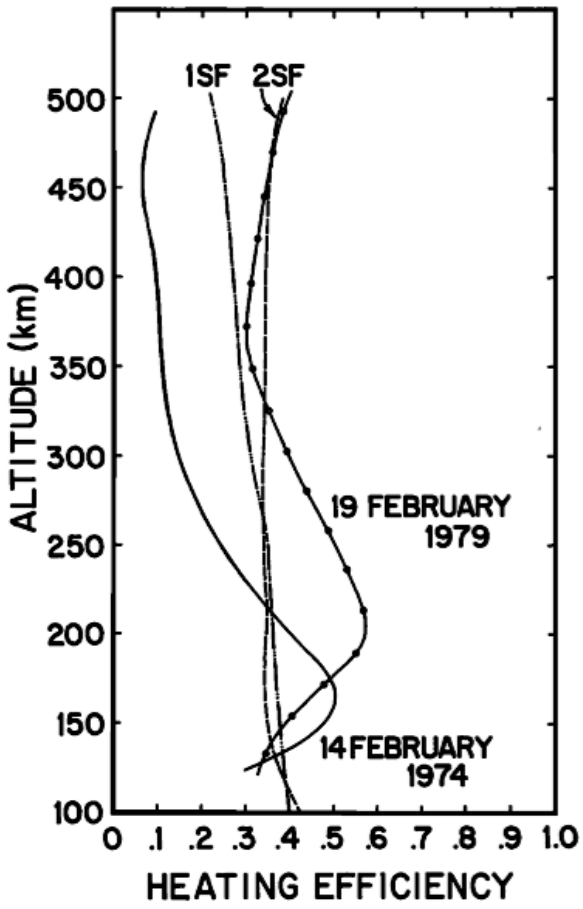

Figure 1.5: Altitude profile of the heating efficiency calculated for solar minimum conditions (1974) and solar maximum conditions (1979) over Millstone Hill observatory for a solar zenith angle of 60° (*Torr et al.*, 1980).

Solar EUV radiation is almost always the main source of energy to the mid- and low-latitudes. In the high-latitudes, however, the Earth's magnetic field is nearly vertical. This means that charged particles in the magnetosphere, which are confined to the field lines, can reach the upper atmosphere. This phenomenon is referred to as particle precipitation, and is the driving mechanism behind the aurora (*Vickrey et al.*, 1982; *Frahm et al.*, 1997; *Onsager and Lockwood*, 1997). During geomagnetic

storms and substorms, the influx of particles into the upper atmosphere from the magnetosphere is highly dynamic, and can become a very significant source of energy to the atmosphere (e.g. *Roble et al.*, 1987; *Codrescu et al.*, 1997; *Deng and Ridley*, 2006). Another consequence of the nearly vertical field lines is that the magnetospheric, or convection, electric field that results from the relative motion of the solar wind past the Earth can be mapped down to ionospheric heights. At times when the solar wind or interplanetary magnetic field (IMF) is dynamic, this electric field can also change quite rapidly. At thermospheric altitudes, the ion velocity reacts almost instantly to changing electric fields. However, the neutral atmosphere is dense compared to the ionosphere, therefore, the neutral velocity reacts sluggishly to the drag force imposed by the ions. Since the ion velocity can be constantly changing, there is always a difference between the ion velocity and the neutral velocity, resulting in frictional heating that can be a very significant source of heat to the thermosphere. During large geomagnetic storms, this Joule heating can become the largest source of energy to the thermosphere (e.g. *Foster et al.*, 1983; *Roble et al.*, 1987; *Codrescu et al.*, 1995; *Deng et al.*, 2009).

The lower atmosphere can also provide energy to the thermosphere. Gravity waves and tides launched by topography, convection, and latent heat release in the troposphere propagate vertically and deposit their energy in the lower thermosphere. In recent years, the study of the creation of these waves, propagation, and dissipation has been an active topic or research (e.g. *Walterscheid et al.*, 2001; *Forbes*, 2007; *Oberheide and Forbes*, 2008). Unlike the other energy sources, which are typically limited to a particular region of the thermosphere or solar zenith angle, gravity waves can occur in more random and localized regions. While topographical features are fixed to the Earth, and there are certainly locations on the globe that are more prone to large scale convective activity, the prediction of gravity wave excitation can still be quite uncertain (*Kim et al.*, 2003).

The major thermospheric mechanisms for the removal of energy from the system are conduction and radiative cooling. Figure 1.6 shows an altitude profile of the global cooling rates. Above 200 km, molecular thermal conduction plays the dominant role

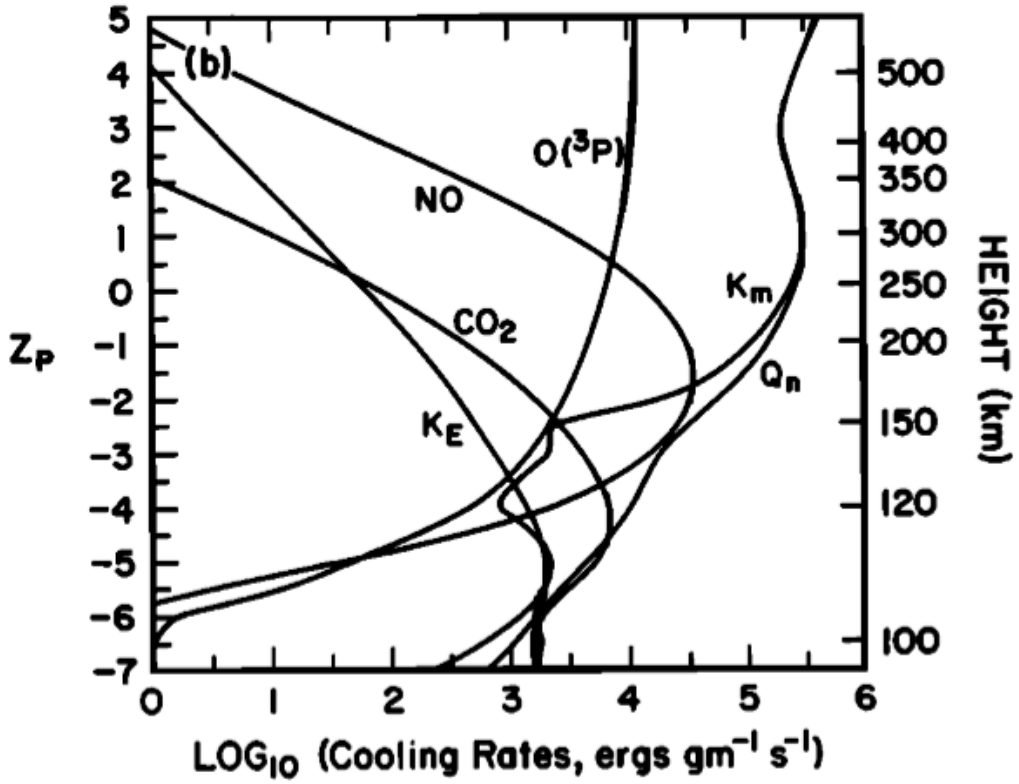

Figure 1.6: Altitude profile of the thermospheric cooling rates (*Roble et al.*, 1987). Q_n denotes the total neutral heating rate, K_m is the molecular thermal conduction, K_E is the eddy thermal conduction, NO is the nitric oxide radiative cooling from the 5.3 μm emission, O(3P) is cooling due to 63 μm and 147 μm emission of atomic oxygen, and CO_2 is the 15 μm cooling from carbon dioxide.

in cooling the thermosphere. This is because the conduction is proportional to the temperature gradient and the temperature itself, which maximizes at roughly 250 km, as well as because the radiative cooling mechanisms are all dependent on the respective densities of the radiators, which are quickly decreasing with altitude. Below the homopause, the eddy conduction acts to reduce the temperature gradient through turbulence, mixing the warmer thermospheric air with the cooler air below.

Figure 1.6 shows that between about 110 and 190 km, radiative cooling processes

provide the dominant cooling rates. Cooling due to the deactivation of the 1^{st} excited vibrational state of nitric oxide, which gives off a photon at 5.3μm is the most important cooling agent. The excited NO is a result of the chemical reaction:

$$NO_{v=0} + M \rightarrow NO_{v=1} + M(k_{10}) \tag{1.5}$$

where M is another molecule or atom and k_{10} is a rate coefficient. Atomic oxygen is the most efficient reactant for producing $NO_{v=1}$ due to its density and the value of K_{10}. This means that even though the NO density is relatively small, the NO cooling rate can still dominate, especially for solar maximum conditions. Still, cooling due to the 15μm emission of CO_2 is quite important in the upper mesosphere and lower thermosphere, and fine structure cooling due to atomic oxygen is significant throughout the thermosphere.

1.1.3 Sources of dynamic forcing

The major dynamics observed in the thermosphere are a result of external dynamical forcing. In 1843, by looking at historical data of sunspot numbers (Figure 1.7), Samuel Schwabe found that solar activity exhibited a periodic cycle of approximately 11 years. As discused in the previous section, the ionosphere-thermosphere system is driven from the top of the atmosphere through coupling with the magnetosphere, as well as through direct coupling with the sun, via radiation, and the solar wind via the magnetospheric cusps. All of these sources of forcing are affected by the solar cycle, and, in general are more dynamic during solar maximum.

1.1.3.1 Magnetospheric forcing variability

During the active part of the solar cycle, or solar maximum, the solar magnetic field becomes highly structured and it is common to observe sudden changes in the

magnitude of the IMF as well as its orientation. Changes in both of these things, as well as in the solar wind velocity, have an affect on the magnitude of the magnetospheric electric field. As mentioned above, variability in the magnetospheric can result in significant amounts of Joule heating in the thermosphere and ionosphere.

In addition, when the direction of the magnetic field suddenly turns southward, the configuration of the magnetosphere can significantly change as a result of the "turning-on" of dayside magnetosphere reconnection (*Sauvaud et al.*, 1987). This allows an influx of solar wind plasma, and can lead to the development of a substorm (e.g. *Lyon et al.*, 1981; *Uritsky et al.*, 2001; *Zhou and Tsurutani*, 2001). During substorms, enhanced reconnection in the magnetospheric tail can accelerate particles towards the Earth, leading to enhanced levels of particle precipitation at high-latitudes, particularly near the midnight sector.

Sometimes, the solar wind and IMF are disturbed as a result of a coronal mass ejection (CME) (*Munro et al.*, 1979; *Hundhausen*, 1993). A CME is generally associated with a disturbance in the IMF magnitude, orientation, and solar wind speed, and since CMEs usually propagate through the heliosphere at super sonic speeds, they are lead by a shock. The interaction of such a feature with the Earth's magnetosphere can cause significant changes in the convection electric field, reconnection rates, and current systems throughout the magnetosphere. The result of these disturbances can be a geomagnetic storm, which are global in nature, and can significantly perturb the upper atmosphere system. There are many studies in which data provided by several of the upper atmospheric and ground based instruments have been examined in order to investigate the response of the thermosphere to dynamic conditions such as geomagnetic storms (e.g. *Hernandez et al.*, 1982; *Burnside et al.*, 1991; *Forbes et al.*, 1996; *Sutton et al.*, 2005).

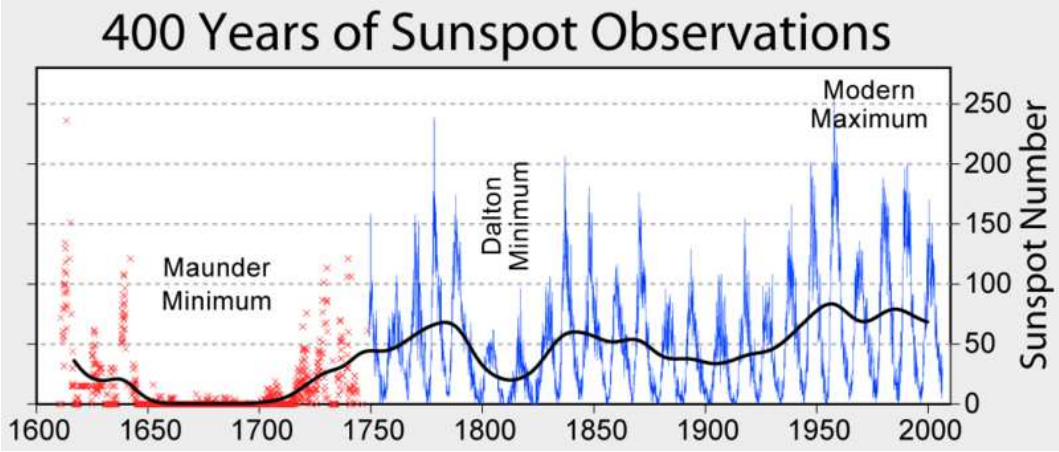

Figure 1.7: Time line of the last 400 years of sunspot observations

1.1.3.2 Solar radiative variability

In addition to dynamic forcing due to magnetospheric variability, the forcing due to direct coupling with the Sun can be highly variable. The Sun radiates throughout the entire spectrum, which is shown in Figure 1.8, and is strongest in the visible and infrared wavelengths. The total amount of energy which is input into the Earth's atmosphere over the entire spectrum is equal to 1366.1 W/m^2. This number varies by about 0.37% from solar minimum to solar maximum, which is why the number is referred to as the Solar Constant: it does not change very much. However, the solar radiation at EUV (1–100 nm) and soft X-ray (0.1–1 nm) wavelengths does vary significantly. Since this part of the spectrum is absorbed by the thermosphere, this variability has an effect on the state of the upper atmosphere.

Forcing due to solar radiation in this part of the spectrum can display variability which occurs on several different time scales. The longest of these is the 11 year solar cycle. Historically, since EUV and soft X-ray radiation is absorbed far above the surface of the Earth, measurements of this part of the spectrum have only been available for small intervals of time. In order to have knowledge of the EUV spectrum when measurements were not available, it was found that the solar flux at 10.7 cm, which could be measured at the surface, correlated well with changes in the EUV

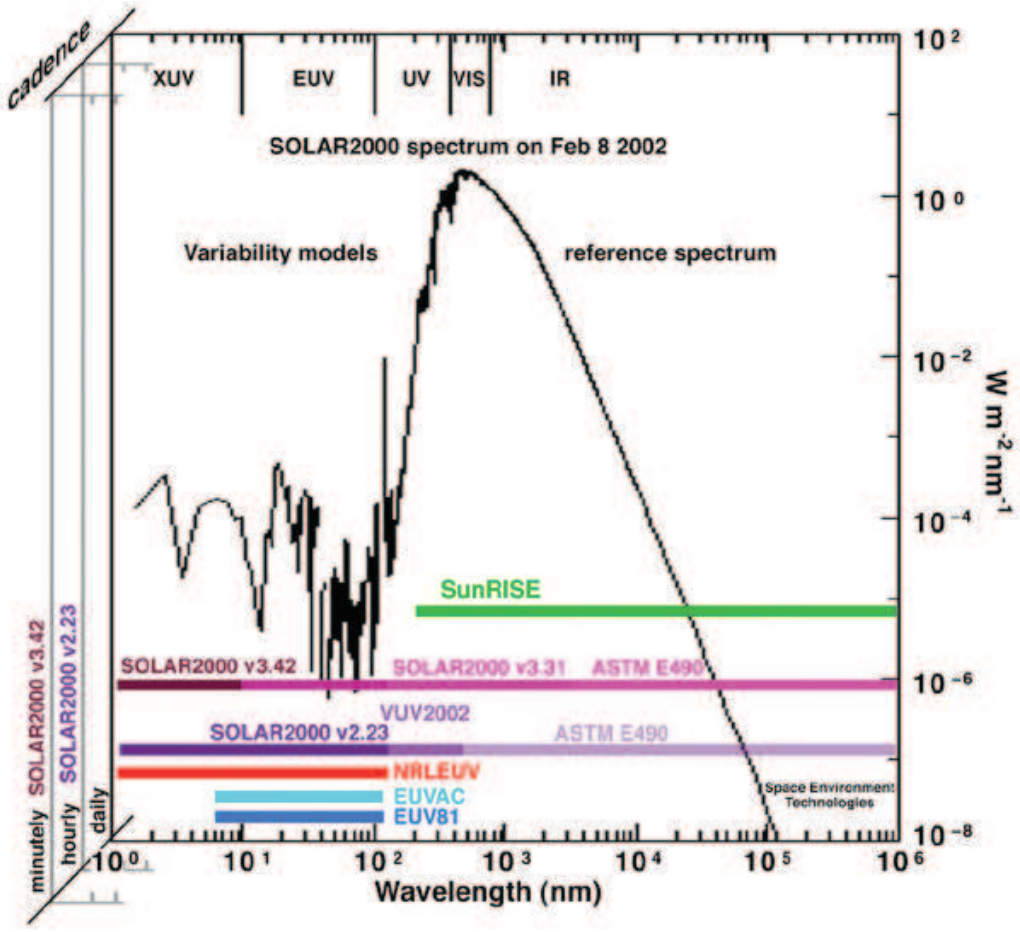

Figure 1.8: The solar spectrum and some models which are used to represent it.

spectrum (e.g. *Donnelly*, 1976; *Hinteregger et al.*, 1981; *Richards et al.*, 1994; *Woods and Rottman*, 2002). This $F_{10.7}$ proxy has been used extensively in order to have knowledge of the EUV flux during time periods of interest. Figure 1.9 shows a plot of the solar radio flux at 10.7 cm from 1966 until 2009, and indicates that the solar flux has a distinct periodicity of approximately 11 years. This variability has significant implications for the thermosphere. Figure 1.10 shows a plot of the thermospheric density at 390 km using the Mass Spectrometer Incoherent Scatter (MSIS) empirical model (*Hedin*, 1991), for solar minimum ($F_{10.7}$ = 70) and solar maximum ($F_{10.7}$ = 230) conditions. The maximum thermospheric neutral density during solar minimum, in this case, is about an order of magnitude smaller than that during solar maximum. While each solar cycle is different in that there may be a deeper minimum, stronger

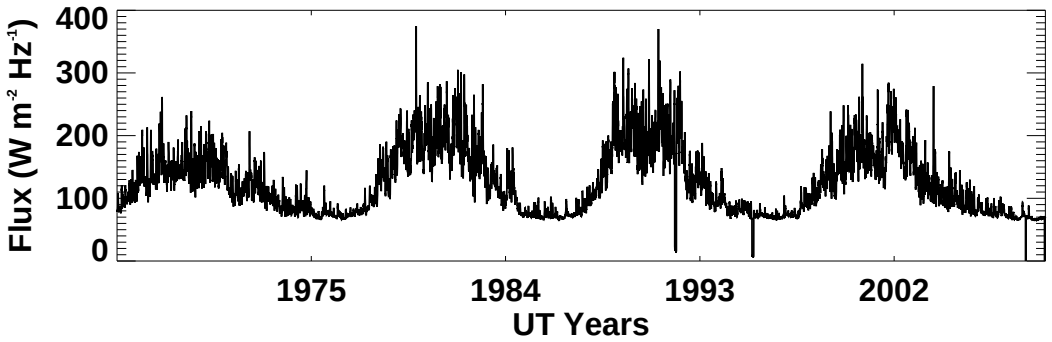

Figure 1.9: The solar flux at 10.7 cm from January 1, 1966 to January 1, 2009.

maximum, or the length of a particular minimum or maximum may be longer or shorter than history suggests, the periodic nature of the solar cycle makes predictions of the thermospheric density variations throughout the solar cycle easier than predictions of shorter term variability.

One of these sources of shorter term variability is associated with the 27 day solar rotation. Since the solar flux at Earth is only dependent on the side of the Sun that faces Earth, features in the photosphere that have a longevity of more than a month can cause the EUV flux to have a periodic structure on the order of a solar rotation. Figure 1.11 shows this periodicity for the year 2000 using $F_{10.7}$ observations. Thermospheric variability associated with the solar rotation is more difficult to predict than that associated with the solar cycle because there is very little information on what is happening on the side of the Sun that faces away from the Earth. Features that were present on the Earth-facing side may intensify, weaken, or disappear altogether as the Sun rotates. In addition, completely new features may appear on the backside of the Sun. Still, historical observations provide some insight into the manner in which the radiative output will vary on the order of 27 days.

In addition to solar variability due to the solar cycle and rotational period, other studies have found periodicity on time scales of 7, 9 and 13.5 days, among others (*Emery et al.*, 2009). These features are due to periodicity in the solar wind velocity and magnetic field as opposed to solar radiation, and the response of the thermosphere

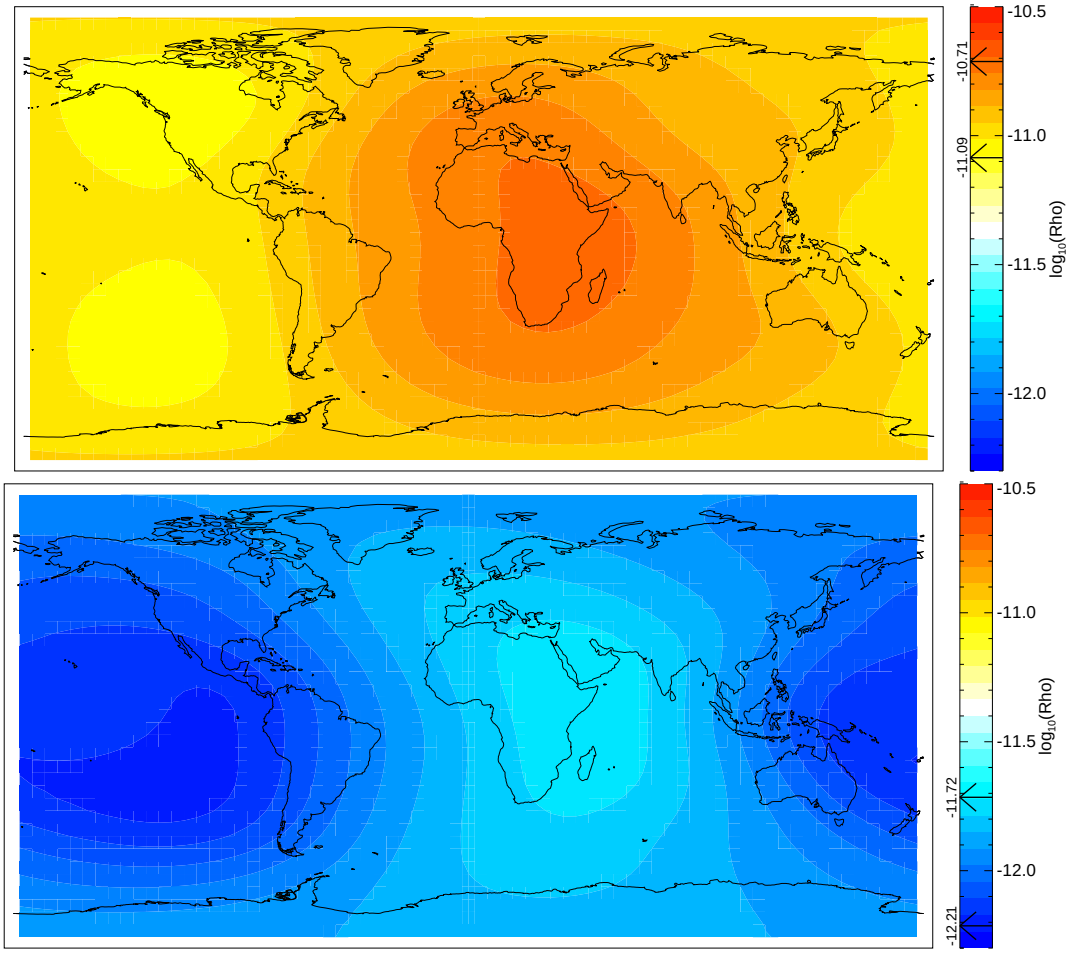

Figure 1.10: Log of the neutral density at 390 km above the surface for solar maximum (top) and solar minimum conditions from the MSIS model.

to these features is a current topic of study within the community.

In addition to sources of variability that have a related periodicity, there are also features that are spontaneous and transient in nature. CMEs are one such feature and have important implications for the upper atmosphere because they are a trigger for geomagnetic storms. Other important transient features that can result in significant perturbations to the ionosphere-thermosphere system are solar flares. Solar flares are sudden, rapid, and intense variations in the radiative emission of the solar atmosphere. They occur when magnetic energy built up in the solar atmosphere is suddenly released. The increase in the radiation occurs throughout the electromagnetic spectrum, however, the largest increases occur at X-ray and EUV wavelengths,

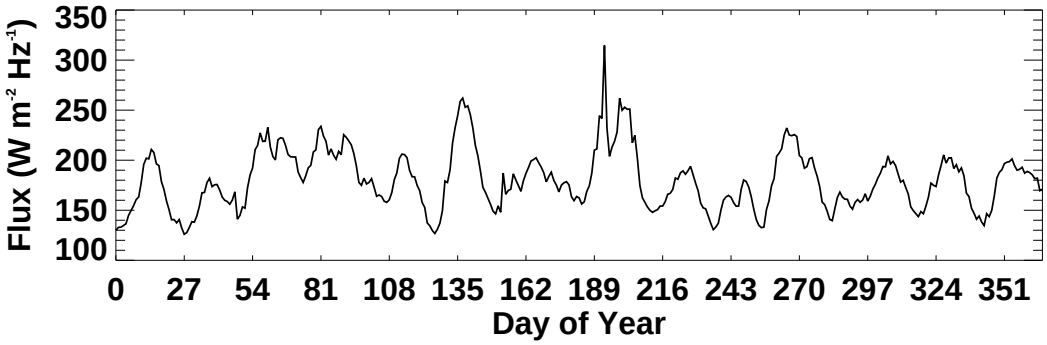

Figure 1.11: $F_{10.7}$ for the year 2000 indicating the 27 day periodicity of the solar flux.

and thus significant thermosphere perturbations can result.

1.2 Solar flares

The response of the upper atmosphere to a solar flare is difficult to predict because no two flares are the same and the state of the atmosphere just before a flare is always different. Flares are typically classified based on the maximum magnitude of the solar flux in the .1-.8 nm region of the spectrum throughout the duration of the flare. Observations of this wavelength range have been made by the Geostationary Operational Environmental Satellites (GOES) since 1985. C-class flares are the smallest flares, and are considered to occur when a transient radiation event occurs where the flux goes above 10^{-6} W/m^2. The minimum flux value for a medium-sized, or M-class, flare is 10^{-5} W/m^2. X-class flares are the largest, and they are considered to occur when the flux goes above 10^{-4} W/m^2. Within each category, flares are further divided up into 9 subdivisions ranging from 1–9. For example, if an X-class flare occurs that has a 1–8 $\mathring{A}$ flux of 2x10^{-4} W/m^2, it would be cataloged as a X2 flare. For a flux of 13x10^{-4} W/m^2, it would be a X13 flare, and so on. Figure 1.12 shows that solar flares follow the 11 year solar cycle, with the majority occurring during solar maximum.

Only recently have studies been performed to quantify the upper atmospheric

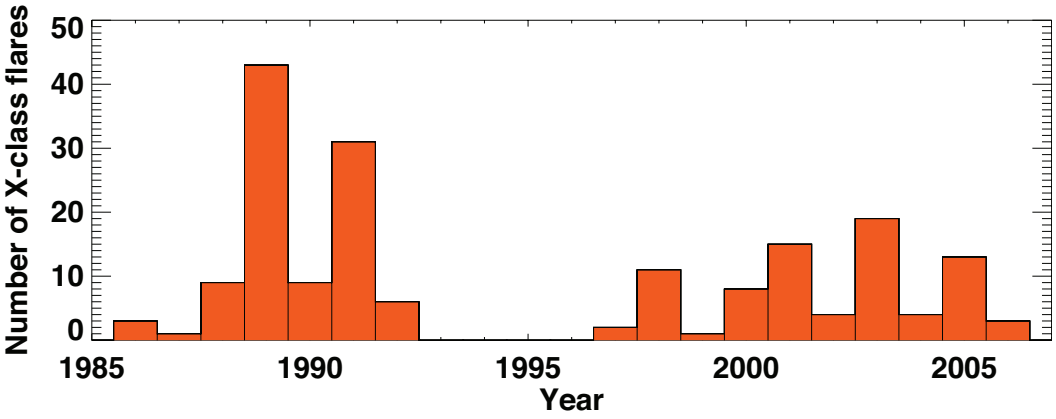

Figure 1.12: Number of x-class flares that have occurred each year since 1985.

response to flares using observations (*Sutton et al.*, 2006; *Liu et al.*, 2007). While this work is invaluable to the community, it is difficult to separate out the effects due to the different physical drivers when using data or event studies. For example, when studying the thermosphere during storm-time, both magnetospheric and solar forcing may contribute to the observed perturbation in the system. This is one reason why global models of the ionosphere-thermosphere system are extremely useful (*Roble et al.*, 1988; *Fuller-Rowell and Rees*, 1980). When using a model, it is possible to investigate the response of the atmosphere due to different forcings individually, simply by ignoring, or holding constant, other sources of dynamics. Another issue is that instruments cannot offer measurements at all scales. Ground-based instruments provide data at high temporal resolution, but at a fixed location, while space-based instruments can provide data on global scales, but the temporal resolution is restricted by the rate of precession of the satellite. Models, however, have the ability to simulate the response of the upper atmosphere to a variety of conditions, globally, and at time increments as small as the user chooses. While models have a global perspective, the physics within the are constrained and they suffer because of the inherent numerical schemes that drive them. Therefore, models have limitations also, but they can be a significant tool to utilize when attempting to understand how the system responds to drivers. For these reasons, this work makes use of the Global

Ionosphere–Thermosphere Model (GITM) (*Ridley et al.*, 2006) to examine the effects of solar flares on the global upper atmosphere.

Sutton et al. (2006) examines one of the strongest solar flares in recorded history, the Halloween flare that occurred on October 28, 2003. The Halloween flare, which was classified as X17, began at approximately 11:00 UT and ended roughly 11 hours later. The magnitude and length of this flare indicates that the total amount of energy added to the atmosphere as a result of increased solar radiation was quite substantial. Figure 1.13 shows that the energy input due to the .1–.8nm region of the spectrum during the Halloween flare was 3.5 J/m^2 above the background. The majority of the X-class flares that have occurred in the past 25 years have supplied significantly less energy into the thermosphere. *Sutton et al.* (2006) found that for the Halloween flare, the dayside thermosphere at low-latitudes was perturbed by as much as 60% during this flare. The magnitude of this perturbation suggests that only large solar flares have a significant influence on the thermosphere. The focus of this thesis is on the types of flares that occur only a handful of times per solar cycle.

While there has been substantial interest in further understanding the effects of external dynamics on the ionosphere–thermosphere system in the past several years, aside from the studies mentioned, little has been done to understand the response of the system, in detail, to solar flares. Specifically, the following questions still need to be addressed: (1) How does the thermosphere respond to large solar flares on a global scale? (2) Do the perturbations in the neutral atmosphere that result from these flares have an effect on the ionosphere? (3) How do the different characteristics of a flare, such as energy, magnitude, and timing, affect the response? The goal of this work is to provide answers to these questions using GITM as well as observations of the thermosphere. Chapters III and IV focus on investigating the atmospheric response to a real flare event, primarily using GITM. In Chapter V, GITM is further used to study the effect of individual flare characteristics on the system, using idealized

simulations. Finally, Chapter VI, a brief analysis of available observations of the thermosphere under solar flare conditions is presented.

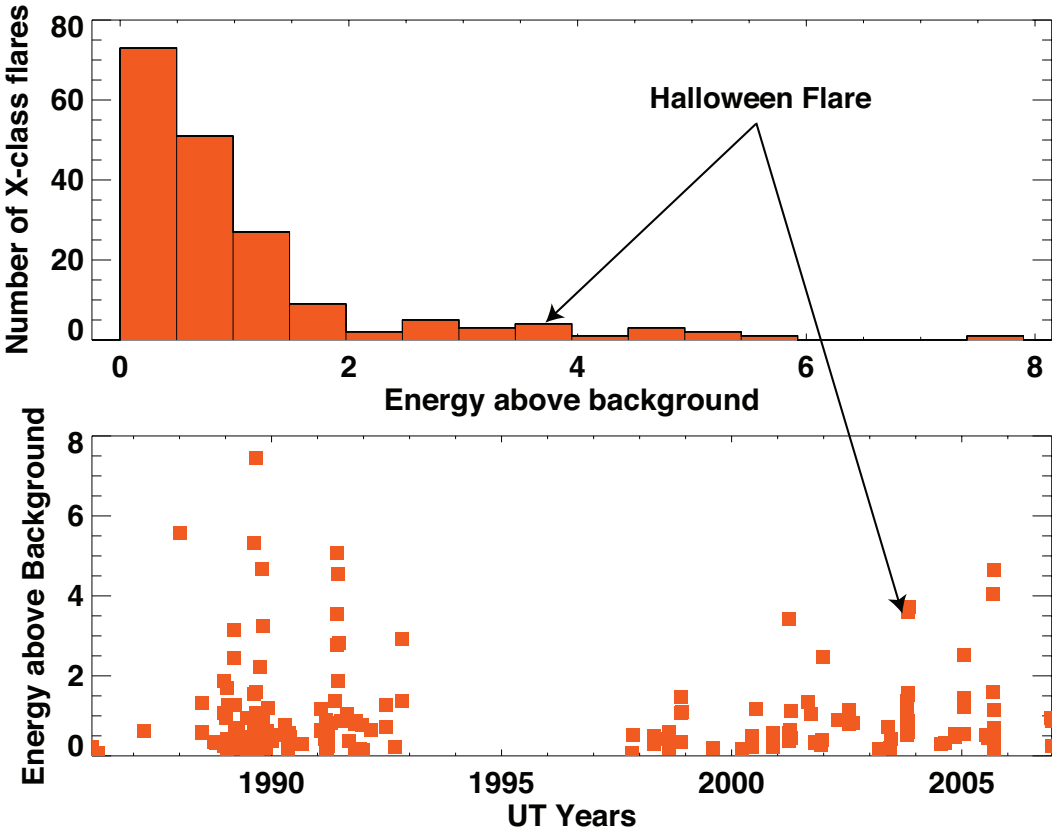

Figure 1.13: X-class solar flares since 1985. (Top) Histogram of the number of X-class flares that have a certain energy above background (1–8$\mathring{A}$, J/m^2). (Bottom) The energy above background (1–8$\mathring{A}$,J/m^2) for each flare plotted by year.

1.2.1 Data studies

Before beginning the body of this thesis, a few notes about the motivation for using a model to study how the atmosphere responds to a solar flare and how data can affect such a study are in order.

1.2.1.1 Observations of the EUV spectrum

In order to study the response of the thermosphere to solar flares, it is important to have a detailed knowledge of the soft X-ray and EUV spectrum. As previously

mentioned, historically, there have been few measurements of this part of the spectrum. However, in 2001, continuous measurements of the wavelength region from 0.5 – 194 nm have been available thanks to the the Solar EUV Experiment (SEE) onboard the Thermosphere Ionosphere Mesosphere Energetics and Dynamics (TIMED) spacecraft. The SEE instrument (*Woods et al.*, 2005) makes measurements of the EUV spectrum using the EUV Grating Spectrograph, which covers the wavelength range from 26 to 194 nm, and the X-Ray Photometer System, which covers 0.5 to 34 nm.

While the SEE observations are immensely valuable to the aeronomy community, measurements are made only once every 90 minutes due to the 3% duty cycle allotted to the instrument. During a solar flare, *Woods et al.* (2004) shows that the soft X-rays can increase by two orders of magnitude in around 10 minutes. Also, some of the strongest solar flares can last less than 2 hours, which means that SEE provides only three or four measurements of the solar irradiance during such flares. For this reason, *Chamberlin et al.* (2007) developed the Flare Irradiance Spectral Model (FISM). FISM is a method used for interpolating the SEE observations based on the higher temporal resolution GOES X-Ray measurements. The result of FISM is a soft X-Ray and EUV dataset that spans 0.1 – 190 nm at 1 minute temporal resolution. The availability of GOES, SEE and FISM data is extremely valuable to the upper atmospheric modeling community, and in particular, FISM data allow modelers to simulate the response to flares under the most realistic conditions ever. Still, in order to obtain the FISM data, assumptions about how the X-ray measurements correspond to the rest of the EUV spectrum are made. While a great deal of thought has gone into the manner in which this is done, there is still some uncertainty in the results (*Chamberlin et al.*, 2007). Table 1.1 summerizes the above mentioned datasets.

Dataset	Spectral Range	Temporal Resolution
GOES	.1–.8 nm	1 minute
SEE	.5–190 nm	90 minute
FISM	.1–190 nm	1 minute

Table 1.1: 3 different datasets which specify the soft X-ray and EUV irradiance

1.2.1.2 Observations of thermosphere

One of the main reasons that models of the thermosphere are so useful for investigating and understanding the physics of the upper atmosphere is that observations of the region are relatively rare. For one, thermospheric altitudes are too high for balloons to reach in order to take in situ measurements. In addition, the density in the thermosphere is sufficiently high that the longevity of a satellite is restricted because atmospheric drag on the satellite will cause the orbit to erode quickly. Since the drag experienced by a satellite is directly proportional to the mass density, the lifetime of a satellite will exponentially decrease with decreasing altitude. At an altitude of 300 km, a satellite will stay in orbit for approximately 27 days without the use of additional fuel. Below 150 km, the lifetime is reduced to hours. One of the alternatives to satellites and balloons are rockets, and they have been successfully utilized to perform detailed studies of upper atmospheric processes. However, the short-term nature of rocket flights means that they are ill-suited for studying transient events.

Most observations of the upper atmosphere come from remote sensing. The existence of several airglow layers at thermospheric altitudes allow observations of several thermospheric variables, including the neutral winds (*Killeen et al.*, 1999; *Russell et al.*, 1999), the O/N_2 ratio (*Christensen et al.*, 2003), altitude profiles of O_2, N_2, and O (*Christensen et al.*, 1994), and nitric oxide densities (*Solomon et al.*, 2001). Ionospheric measurements are made by a variety of instruments including, among others, incoherent scatter radars (*Evans*, 1972; *Brekke et al.*, 1974), which observe the electron density, electron and ion temperatures and ion velocity throughout the

ionosphere, ionosondes, which also provide measurements of the electron density up to the altitude of the peak electron density (H_mF_2) and all sky cameras, which are used to perform studies of the aurora, dayglow, and nightglow. One of the most useful measurements for the current study are in situ measurements of the neutral mass density. These observations are made by the CHAllenging Mini-satellite Payload (Champ) satellite (*Reigber et al.*, 2000), which is in a polar orbit at an altitude of roughly 400 km. The density measurements are made by an on-board high-resolution accelerometer, that obtains density observations by recording the acceleration of the spacecraft. These accelerations are dependent on the drag experienced by the satellite, which will change if the ambient density changes. Given a thorough knowledge of the spacecraft's drag coefficient, it is possible to obtain a density.

Champ observations have been used to study the thermosphere in detail. Aside from the work by *Sutton et al.* (2006), studies by *Sutton et al.* (2005) and *Thayer et al.* (2008) have used these observations to study the thermospheric response to severe geomagnetic storms as well as periodic solar wind forcing. Still, Champ measurements are only available at a single measurement point, and the satellite rate of precession is such that global coverage is achieved only every 30 days. Therefore, it is inherently difficult to use Champ to investigate the global thermospheric response to a transient event, such as a solar flare. Furthermore, as is demonstrated in Chapter III, the largest perturbations in the thermosphere after a solar flare occur near solar zenith angles (SZA) of 0° and 180°. This means that ideally, observations should be available in the noon–midnight sectors or from a satellite in a 12:00 – 24:00 local time (LT) orbit. While Champ is certainly in such an orbit from time to time, the slow rate of precession means that often, it is not. These issues make performing an in-depth statistical study using data of the neutral density response to solar flares quite difficult. However, data can be used on an event by event basis. In Chapter VI, this type of study is performed utilizing measurements from Champ, as well as data from

the Global Ultra-Violet Imager (GUVI) (*Christensen et al.*, 1994) and the Sounding of the Atmosphere using Broadband Emission Radiometery (SABER) instrument.

CHAPTER II

Methodology

The main tool used to investigate the manner in which the global upper atmosphere responds to solar flares is GITM. This chapter provides a summary of the model itself, including the important numerics of the model, assumptions, chemical processes, and descriptions of the sources of energy into the model. In addition, an analysis of the parameters used in the model is presented to provide an understanding of the uncertainties involved in using a large-scale 3-dimensional (3-D) model to investigate a highly-coupled non-linear system.

2.1 The Global Ionosphere-Thermosphere Model

GITM is a 3-D model that solves for the coupled ionosphere-thermosphere system, from 100 km to about 600 km. The model solves for the neutral and ion temperatures and vector velocities, as well as the densities of the following 8 neutral species: N_2, O_2, $O(3P)^a$, $N(4S)^a$, NO, $N(2D)^b$, $N(2P)^b$, and $O(1D)^b$, and the following 7 ion species: $O(4S)^{+a}$, O_2^+, N_2^+, N^+, NO^+, $O(2D)^{+b}$, and $O(2P)^{+b}$. The total neutral and ion densities are then calculated by summing over the species. One of the basic assumptions about the ionosphere is that it is charge neutral. This means that

[a] Ground state
[b] Excited state

the total number of ions is equal to the total number of electrons. In addition to calculating the total velocity vector for the neutrals, GITM also vertically advects 5 neutrals, N_2, O_2, O(3P), N(4S), and NO. Therefore, GITM solves the vertical momentum equation individually for each of these species. The reason for this is that above the homopause, individual species become hydrostatically balanced based on their own mass, therefore, it is not adequate to assume each species moves vertically with the same velocity.

2.1.1 Fundamental equations

In order to obtain the densities, velocities, and temperatures mentioned above, GITM solves the fluid equations in a 3-D spherical coordinate system. As mentioned in Section 1.1.1, one of the fundamental simplifying assumptions usually made about the state of the thermosphere, is that it is in hydrostatic equilibrium (1.1). This is not the case in GITM. Rather, as mentioned above, the momentum equation is solved in the vertical direction self-consistently, which, as demonstrated by *Deng et al.* (2008), allows significant acceleration and vertical velocities to develop. In addition, GITM uses an altitude based vertical coordinate as opposed to a pressure based coordinate. This is done because using a pressure coordinate system requires that the system be in hydrostatic equilibrium. These two features make GITM unlike other global circulation models (GCMs) of the ionosphere-thermosphere region.

If sources are temporarily ignored, the total mass density, ρ, is written as:

$$\rho = \sum_s M_s n_s, \tag{2.1}$$

where M_s is the molecular mass of species s, n_s is the number density of species s, and a normalized neutral temperature, $\mathcal{T}$, is introduced:

$$\mathcal{T} = P/\rho, \tag{2.2}$$

where P is the total neutral pressure. Then, the continuity equation is written as

$$\frac{\partial n_S}{\partial t} + n_s \nabla \cdot \mathbf{u} + \mathbf{u} \cdot \nabla n_s = 0, \tag{2.3}$$

where $\mathbf{u}$ is the average neutral velocity vector,

$$\mathbf{u} = \frac{1}{\rho} \sum_s M_s N_s \mathbf{u}_s, \tag{2.4}$$

and t is time. The momentum equation is

$$\frac{\partial \mathbf{u}}{\partial t} + \mathbf{u} \cdot \nabla \mathbf{u} + \nabla \mathcal{T} + \frac{\mathcal{T}}{\rho} \nabla \rho = 0, \tag{2.5}$$

and the energy equation is

$$\frac{\partial \mathcal{T}}{\partial t} + \mathbf{u} \cdot \mathcal{T} + (\gamma - 1) \mathcal{T} \nabla \cdot \mathbf{u} = 0, \tag{2.6}$$

where γ is the ratio of specific heats. Solving the above equations in the vertical direction is difficult because vertical gradients are quite strong. For this reason, the fluid equation are broken up into the horizontal and vertical directions and solved for separately. In the vertical, or radial, direction, the natural logarithm of the mass density and number densities are used as the primitive variables:

$$\mathcal{R} = ln(\rho) \tag{2.7}$$

$$\mathcal{N}_s = ln(n_s). \tag{2.8}$$

This is done because, while the density varies exponentially with altitude, the logarithm of the density varies nearly linearly, which is easier to solve numerically. The energy equation is written in terms of the normalized temperature, $\mathcal{T}$, instead of the

exponentially varying P for this reason.

If the equations are cast in spherical rotating coordinates, then the vertical continuity equation becomes

$$\frac{\partial \mathcal{N}_s}{\partial t} + \frac{\partial u_{r,s}}{\partial r} + \frac{2u_{r,s}}{r} + u_{r,s}\frac{\partial \mathcal{N}_s}{\partial r} = \frac{1}{N_s}\mathcal{L}_s, \tag{2.9}$$

where the subscript r denotes the radial component, $u_{r,s}$ is the radial neutral velocity of species s, and $\mathcal{L}_s$ are the source and loss terms, which are described in section 2.1.2. The $\frac{2u_{r,s}}{r}$ term comes from the radial divergence of the radial component of the velocity.

The vertical momentum equation becomes

$$\begin{aligned}\frac{\partial u_{r,s}}{\partial t} + u_{r,s}\frac{\partial u_{r,s}}{\partial r} + \frac{u_\theta}{r}\frac{\partial u_{r,s}}{\partial \theta} + \frac{u_\phi}{r cos\theta}\frac{\partial u_{r,s}}{\partial \phi} + \frac{k}{M_s}\frac{\partial T}{\partial r} + T\frac{K}{M_s}\frac{\partial \mathcal{N}_s}{\partial r} \\ = g + F_s + \frac{u_\theta^2 + u_\phi^2}{r} + cos^2\theta\Omega^2 r + 2cos\theta\Omega u_\phi,\end{aligned} \tag{2.10}$$

where θ is the north latitude, ϕ is the east longitude, u_θ is the northward neutral velocity, u_ϕ is the eastward neutral velocity, Ω is the angular velocity of the Earth, g is gravity, and F_s are the source and loss terms due to ion-neutral friction and neutral-neutral friction. The last two terms on the right side are the centrifugal and Coriolis forces. The $\frac{u_\theta^2+u_\phi^2}{r}$ term is due to the spherical geometry and causes the horizontal winds to "lift off" from the Earth's curved surface.

In the horizontal direction, the eastward momentum equation becomes

$$\begin{aligned}\frac{\partial u_\phi}{\partial t} + u_r\frac{\partial u_\phi}{\partial r} + \frac{u_\theta}{r}\frac{\partial u_\phi}{\partial \theta} + \frac{u_\phi}{r cos\theta}\frac{\partial u_\phi}{\partial \phi} + \frac{1}{r cos\theta}\frac{\partial \mathcal{T}}{\partial \phi} + \frac{\mathcal{T}}{r\rho cos\theta}\frac{\partial \rho}{\partial \phi} \\ = \frac{F_\phi}{\rho} + \frac{u_\phi u_\theta tan\theta}{r} - \frac{u_r u_\phi}{r} + 2\Omega u_\theta sin\theta - 2\Omega u_r cos\theta,\end{aligned} \tag{2.11}$$

and the northward momentum equation is

$$\frac{\partial u_\theta}{\partial t} + u_r\frac{\partial u_\theta}{\partial r} + \frac{u_\theta}{r}\frac{\partial u_\theta}{\partial \theta} + \frac{u_\phi}{rcos\theta}\frac{\partial u_\theta}{\partial \phi} + \frac{1}{r}\frac{\partial \mathcal{T}}{\partial \theta} + \frac{\mathcal{T}}{r\rho}\frac{\partial \rho}{\partial \theta}$$
$$= \frac{F_\theta}{\rho} - \frac{u_\phi^2 tan\theta}{r} - \frac{u_r u_\theta}{r} - \Omega^2 rcos\theta sin\theta - 2\Omega u_\phi sin\theta, \tag{2.12}$$

where F_ϕ and F_θ are the eastward and northward momentum source terms. Again, the terms involving Ω are due to the Coriolis force and those involving Ω^2 are due to the centrifugal force. In addition, the terms including the velocity on the right side are due to the spherical geometery.

Finally, the neutral energy equation is also broken up into vertical and horizontal components. In the vertical direction

$$\frac{\partial \mathcal{T}}{\partial t} + u_r\frac{\partial \mathcal{T}}{\partial r} + (\gamma - 1)\mathcal{T}(\frac{2u_r}{r} + \frac{\partial u_r}{\partial r}) = \frac{k}{c_v \rho \overline{m_n}}\mathcal{L}, \tag{2.13}$$

and in the horizontal direction

$$\frac{\partial \mathcal{T}}{\partial t} + \frac{u_\phi}{rcos\theta}\frac{\partial \mathcal{T}}{\partial \phi} + \frac{u_\theta}{r}\frac{\partial \mathcal{T}}{\partial \theta} + (\gamma - 1)\mathcal{T}(\frac{1}{r}\frac{\partial u_\theta}{\partial \theta} + \frac{1}{rcos\theta}\frac{\partial u_\phi}{\partial \phi} - \frac{u_\theta tan\theta}{r}) = 0. \tag{2.14}$$

where the specific heat at a constant volume is denoted by c_v, and $\mathcal{L}$ are the energy source and loss terms. Again, the $\frac{2u_r}{r}$ term is due to the spherical geometery.

In the ionosphere, the equations are also separated into the horizontal and vertical directions. The horizontal continuity equation has the form

$$\frac{\partial N_j}{\partial t} + \frac{v_\theta}{r}\frac{\partial N_j}{\partial \theta} + \frac{v_\phi}{rcos\theta}\frac{\partial N_j}{\partial \phi} = \mathcal{L}_j, \tag{2.15}$$

and in the vertical direction

$$\frac{\partial \mathcal{N}_j}{\partial t} + v_r\frac{\partial \mathcal{N}_j}{\partial r} = 0, \tag{2.16}$$

where N_j is the number density of the jth ion, $\mathcal{N}_j = ln(N_j)$, and $\mathcal{L}_j$ are the sources

and losses of ions due to chemical and ionization processes. It possible to advect multiple ions, but it is typical to do so only for O^+ since it is the dominant ion in the low collision region of the ionosphere (*Schunk and Nagy*, 2000).

In GITM, the ion momentum equation is simplified by assuming the ions are in steady state, and that the flow velocity is much slower than the sound speed. This means the convective derivative terms on the left side of equation 2.5 are zero. Therefore, the ion momentum equation can be written as

$$\mathbf{v} = \frac{\mathbf{A} \cdot \mathbf{b}}{\rho_i \nu_{in}} + \frac{\rho_i \nu_{in} \mathbf{A}_\perp + e N_e \mathbf{A}_\perp \times \mathbf{B}}{\rho_i^2 \nu_{in}^2 + e^2 N_e^2 B^2}, \tag{2.17}$$

where $\mathbf{A}$ are force terms described by

$$\mathbf{A} = \rho_i \mathbf{g} + e N_e \mathbf{E} - \nabla(P_i + P_e) + \rho_i \nu_{in} \mathbf{u}, \tag{2.18}$$

$B = \|\mathbf{B}\|$ is the magnitude of the magnetic field, $\mathbf{b} = \mathbf{B}/B$ is the direction of the magnetic field, $\mathbf{A}_\perp$ is the component of $\mathbf{A}$ that is perpendicular to the magnetic field, N_e is the electron density, e is the electron charge, P_i and P_e are the ion and electron pressures, and ν_{in} is the ion-neutral collision frequency. In this manner, the ion velocity is broken up into a component that is parallel to the magnetic field, and a component that is perpendicular to the magnetic field.

The ion temperature equation is not solved in GITM. Instead, it is calculated using an altitude-dependent linear combination of the neutral and electron temperatures. The electron temperature is solved for using the electron energy equation

$$\frac{\partial T_e}{\partial t} = -\frac{2}{3} T_e \nabla \cdot \mathbf{v}_e - \mathbf{v}_e \cdot \nabla T_e + \frac{2}{3 N_e k}(-\nabla \cdot \mathbf{q}_e + Q_e - L_e), \tag{2.19}$$

where $\mathbf{e}$ is the electron drift velocity, T_e is the electron temperature, $\mathbf{q}_e$ is the electron heat flux, which is approximated by $\mathbf{q}_e = -\kappa_e \nabla T_e$, where κ_e is the electron thermal

conduction coefficient, and Q_e and L_e are the electron heat sources and losses. There are two sources of heat to the electrons in GITM, Joule and EUV heating. The EUV heating which is done in a similar manner as the neutral EUV heating (section 2.1.2.1), using a smaller heating efficiency, is dominant except at high latitudes.

There are many processes that are effective in cooling the electron gas (*Schunk and Nagy*, 2000). In GITM, cooling due to rotational excitation of N_2 and O_2 is included as a loss of heat, as is vibrational excitation of N_2 and O_2. In addition, electronic excitation of $O(^1D)$ is included due to its importance at temperatures greater than 1500K.

2.1.2 Thermospheric source and loss terms

Since most of this thesis focuses on the manner in which the thermosphere deals with the incident energy from a solar flare, the source terms for the neutral fluid equations are explained in detail in this section.

After the advection is completed, source and loss terms are added to the the solution. For the neutral continuity equation, the sources and losses included are specified by eddy diffusion and the results of chemistry. The major chemical processes that occur in the thermosphere and ionosphere, including photodissociation, photoionization,

recombination, and charge-exchange lead to the following main chemical reactions:

$$O_2 + h\nu \rightarrow O + O \tag{2.20}$$

$$O_2 + h\nu \rightarrow O_2^+ + e \tag{2.21}$$

$$O + h\nu \rightarrow O^+ + e \tag{2.22}$$

$$N_2 + h\nu \rightarrow N_2^+ + e \tag{2.23}$$

$$O^+ + N_2 \rightarrow NO^+ + N \tag{2.24}$$

$$O^+ + O_2 \rightarrow O_2^+ + O \tag{2.25}$$

$$N_2^+ + O_2 \rightarrow O_2^+ + O \tag{2.26}$$

$$N_2^+ + O \rightarrow O^+ + N_2 \tag{2.27}$$

$$N_2^+ + O \rightarrow NO^+ + N \tag{2.28}$$

$$NO^+ + e \rightarrow N + O \tag{2.29}$$

$$O_2^+ + e \rightarrow O + O \tag{2.30}$$

$$N_2^+ + e \rightarrow N + N \tag{2.31}$$

In calculating the chemical sources and losses, GITM accounts for these reactions as well as all the reactions included in *Rees* (1989). These reactions and their rates are listed in table 2.1. To do this, GITM uses a sub-cycling technique, which does not require any assumptions on chemical equilibrium. The chemical time step is determined by ensuring that the number density of each species can only be reduced by a maximum of 25%. The number of chemical time steps taken is equal to the advective time step divided by the chemical time step, and is calculated at each grid cell. Above roughly 150 km, the advective time step, which is determined by satisfying the CFL condition,

$$CFL = \Delta t \frac{v_{max}}{\Delta x}, \tag{2.32}$$

where CFL is a unit-less number less than or equal to unity which ensures stability when solving the momentum equation, Δt refers to the advective time step, v_{max} is a characteristic speed, in this case, the speed of sound, and Δx, is the grid spacing, is less than the chemical time step. Therefore, only 1 chemical time step is required in this region. Near the lower boundary of the model, where the chemistry is fast, several hundred chemical time steps are performed.

Reaction	Rate coefficient (m^3/s)	f	Reference
$O + O + M \rightarrow O_2 + M$	$9.59x10^{-40}\exp(480/T_n)$		
$O^+(^2D) + N_2 \rightarrow N_2 + O^+(^4S)$	$8.0x10^{-16}$		
$O^+(^2P) + N_2 \rightarrow N_2^+ + O$	$4.8x10^{-16}$		
$N_2^+ + O_2 \rightarrow O_2^+ + N_2$	$5.0x10^{-17}\frac{T_r}{300}^{-0.8}$		
$N_2^+ + O \rightarrow NO^+ + N(^2D)$	$1.4x10^{-16}\frac{T_r}{300}^{-0.44}$		
$N_2^+ + e \rightarrow 2N(2D)$	$1.8x10^{-13}\frac{T_e}{300}^{-0.39}$		
$N_2^+ + O \rightarrow O^+(^4S) + N_2$	$1.4x10^{-16}\frac{T_r}{300}^{-0.44}$		
$N_2^+ + NO \rightarrow NO^+ + N_2$	$3.3x10^{-16}$		
$O^+(^4S) + O_2 \rightarrow O_2^+ + O$	$2.0x10^{-17}\frac{T_r}{300}^{-0.4}$		
$O^+(^2D) + O_2 \rightarrow O_2^+ + O$	$7.0x10^{-16}$		
$N^+ + O_2 \rightarrow O_2^+ + N(^4S)$	$1.1x10^{-16}$		
$N^+ + O_2 \rightarrow O_2^+ + N(^2D)$	$2.0x10^{-16}$		
$O_2^+ + e \rightarrow O(^1D) + O(^1D)$	$2.4x10^{-13}$	0.31	*Schunk and Nagy* (2000)
$O_2^+ + e \rightarrow O(^1D) + O(^3P)$	$2.4x10^{-13}$	0.42	*Schunk and Nagy* (2000)
$O_2^+ + e \rightarrow O(^3P) + O(^3P)$	$2.4x10^{-13}$	0.22	*Schunk and Nagy* (2000)
$O_2^+ + N(^4S) \rightarrow NO^+ + O$	$1.8x10^{-16}$		
$O_2^+ + NO \rightarrow NO^+ + O_2$	$4.4x10^{-16}$		
$O_2^+ + N_2 \rightarrow NO^+ + NO$	$5.0x10^{-22}$		
$O^+(^2D) + O \rightarrow O^+(^4S) + O(^3P)$	$1.0x10^{-17}$	0.5	
$O^+(^2D) + O \rightarrow O^+(^4S) + O(^1D)$	$1.0x10^{-17}$	0.5	
$O^+(^2D) + e \rightarrow O^+(^4S) + e$	$7.8x10^{-14}\frac{T_e}{300}^{-0.5}$		
$O^+(^2D) + N_2 \rightarrow O^+(^4S) + N_2$	$8.0x10^{-16}$		
$O^+(^2P) + O(^3P) \rightarrow O(^3P) + O(^4S)$	$5.2x10^{-17}$		
$O^+(^2P) + e \rightarrow O^+(^4S) + e$	$4.0x10^{-14}\frac{T_e}{300}^{-0.5}$		
$O^+(^2P) \rightarrow O^+(^4S) + h\nu_{2470}$	$0.047s^{-1}$		
$N^+ + O_2 \rightarrow O^+(^4S) + NO$	$3.0x10^{-17}$		
$O^+(^4S) + N_2 \rightarrow NO^+ + N(^4S)$	$4.5x10^{-20}\frac{T_r}{300}^{2}$		

Table 2.1 Continued

Reaction	Rate coefficient (m^6/s)	f	Reference
	$5x10^{-19}, T_r < 1000K$		
$O^+(^4S) + NO \rightarrow NO^+ + O(^3P)$	$8.0x10^{-19}$		
$O^+(^4S) + N(^2D) \rightarrow N^+ + O(^3P)$	$1.3x10^{-16}$		
$O^+(^2P) + e \rightarrow O^+(^2D) + e$	$1.4x10^{-13}\frac{T_e}{300}^{-0.5}$		
$O^+(^2P) \rightarrow O^+(^2D) + h\nu_{7320}$	$0.171s^{-1}$		
$O^+(^2D) \rightarrow O^+(^4S) + h\nu_{3726}$	$7.7x10^{-5}s^{-1}$		
$O^+(^2P) + N_2 \rightarrow N^+ + NO$	$1.0x10^{-16}$		
$O_2^+ + N(^2D) \rightarrow N^+ + O_2$	$2.5x10^{-16}$		
$O^+(^2P) + N \rightarrow N^+ + O$	$1.0x10^{-16}$		
$O^+(^2D) + N \rightarrow N^+ + O(^3P)$	$7.5x10^{-17}$		
$N^+ + O_2 \rightarrow NO^+ + O(^1D)$	$2.6x10^{-16}$		
$N^+ + O(^3P) \rightarrow O^+ + N$	$5.0x10^{-19}$		
$NO^+ + e \rightarrow O(^3P) + N(^4S)$	$4.2x10^{-13}\frac{T_e}{300}^{-0.85}$	0.22	
$NO^+ + e \rightarrow O(^3P) + N(^2D)$	$4.2x10^{-13}\frac{T_e}{300}^{-0.85}$	0.78	
$N(^2D) + e \rightarrow N(^4S) + e$	$5.5x10^{-16}\frac{T_e}{300}^{0.5}$		
$N(^2D) + O(^3P) \rightarrow N(^4S) + O(^3P)$	$2.0x10^{-18}$	0.9	
$N(^2D) + O(^3P) \rightarrow N(^4S) + O(^1D)$	$2.0x10^{-18}$	0.1	
$N(^2D) \rightarrow N(^4S) + h\nu_{5200}$	$1.06x10^{-5}s^{-1}$		
$N(^4S) + O_2 \rightarrow NO + O(^3P)$	$4.4x10^{-18}exp(\frac{-3220}{T_n}$		
$N(^4S) + NO \rightarrow N_2 + O(^3P)$	$1.5x10-18\sqrt{T_n}$		
$N(^2P) \rightarrow N(^2D) + h\nu_{10400}$	$7.9x10^{-2}s^{-1}$		
$N(^2D) + O_2 \rightarrow NO + O(^3P)$	$6.2x10^{-18}\frac{T_n}{300}$	0.9	*Torr et al.* (1981)
$N(^2D) + O_2 \rightarrow NO + O(^1D)$	$6.2x10^{-18}\frac{T_n}{300}$	0.1	*Torr et al.* (1981)
$N(^2D) + NO \rightarrow N_2 + O(^3P)$	$7.0x10^{-17}$		
$O(^1D) \rightarrow O(^3P) + h\nu_{6300}$	$0.0071s^{-1}$		*Torr and Torr* (1982)
$O(^1D) \rightarrow O(^3P) + h\nu_{6364}$	$0.00221s^{-1}$		*Torr and Torr* (1982)
$O(^1D) + e \rightarrow O(^3P) + e$	$2.6x10^{-17}T_e^{-0.5}exp(\frac{-22740}{T_e})$		*Torr and Torr* (1982)

Table 2.1 Continued

Reaction	Rate coefficient (m^6/s)	f	Reference
$O(^1D) + N_2 \rightarrow O(^3P) + N_2$	$2.3x10^{-17}$		*Torr et al.* (1980)
$O(^1D) + O_2 \rightarrow O(^3P) + O_2$	$2.9x10^{-17}T_n^{0.6}$		*Torr et al.* (1980)
$O(^1D) + O(^3P) \rightarrow O(^3P) + O(^3P)$	$8.0x10^{-18}$		*Torr and Torr* (1982)

Table 2.1: GITM chemistry. f refers to the branching ratio where applicable. All references are from *Rees* (1989) unless otherwise noted.

In addition to centrifugal, Coriolis, and geometrical force terms that are introduced into the momentum equation when using a rotating spherical coordinate system, ion-drag (*Rees*, 1989) and neutral–neutral friction (in the vertical direction) are included as momentum sources. In spherical coordinates, the ion-neutral friction and viscosity terms in the horizontal direction are given by:

$$F_\theta = \rho_i \nu_{in}(v_\theta - u_\theta) + \frac{\partial}{\partial r}\eta\frac{\partial u_\theta}{\partial r} \tag{2.33}$$

$$F_\phi = \rho_i \nu_{in}(v_\phi - u_\phi) + \frac{\partial}{\partial r}\eta\ \frac{\partial u_\phi}{\partial r}, \tag{2.34}$$

where i refers to the ions and n refers to the neutrals, ν_{in} is the ion-neutral collision frequency, v is the vertical ion velocity, and η is the coefficient of viscosity. The first term in the above equations is the horizontal ion drag term. The second term is the viscosity due to the radial shear of horizontal wind. In the vertical direction, the source term is made up of an ion drag term similar to that in equations 2.33 and 2.34 an a neutral–neutral friction term. Viscous interactions that contribute to the vertical velocities are assumed to be negligible.

The energy source terms are given by:

$$\mathcal{L} = Q_{EUV} + Q_{NO} + Q_O + Q_p + \frac{\partial}{\partial r}\left((\kappa_c + \kappa_{eddy})\frac{\partial T}{\partial r}\right) + N_e \frac{\overline{m}_i \overline{m}_n}{\overline{m}_i + \overline{m}_n}\nu_{in}(\mathbf{v}-\mathbf{u})^2. \tag{2.35}$$

Q_{EUV}, Q_p, Q_{NO}, and Q_O are the EUV heating, particle heating, and NO and O cooling terms respectively, κ_c is the thermal conductivity, κ_{eddy} is the eddy conductivity, and the final term is a frictional or Joule heating term.

Above 110 km, the eddy conductivity term is not important on Earth (*Roble et al.*, 1987). However, as discussed in section 1.1.2, thermal conduction is extremely important for the redistribution of energy throughout the entire thermosphere. In

GITM, the thermal conductivity is calculated at each grid cell according to:

$$\kappa_c = \sum_{q=O,O_2,N_2} \frac{[N_i]}{[N_{total}]} A_q T_q^s \tag{2.36}$$

where the coefficients, A_q, and the exponents, s_q, are held constant. As it turns out, the values of these coefficients are subject to some uncertainty, the effects of which on the thermosphere are discussed in section 2.2.

Particle, or auroral, heating is important at high latitudes where precipitating electrons from the magnetosphere deposit energy via collisions with the ions and neutrals. This source of heat is accounted for using the technique described by *Frahm et al.* (1997), where the particle flux at a given energy range is specified based on the hemispheric power index (HPI) (*Fuller-Rowell and Evans*, 1987).

The radiative cooling terms, Q_{NO} and Q_O, are specified by (*Kockarts*, 1980) and (*Kockarts and Peetermans*, 1970) respectively. *Dickinson* (1984) and *Roble et al.* (1987) show that the 15μm CO_2 emission is an important source of cooling to the lower thermosphere, and below 120 km, it can be the dominant cooling agent contributing more than 0.5 J (kg s)$^{-1}$ to the total cooling rage. However, GITM does not include this source of heat loss because the addition of CO_2 significantly increases the complexity of the chemistry. CO_2 cooling will be added to the model in the near future.

2.1.2.1 EUV heating

As mentioned in section 1.1.2, most of the time, the incident EUV radiation is the primary source of energy into the thermosphere, especially at mid- and low-latitudes. In GITM, the EUV heating can be specified in a number of ways. For theoretical or long term studies, the $F_{10.7}$ proxy is typically used to specify the solar flux.

There are a number of studies that have developed proxy based models of the EUV

spectrum using the $F_{10.7}$ (*Tobiska et al.*, 2000; *Woods and Rottman*, 2002; *Solomon and Qian*, 2005). In addition, the models developed by *Hinteregger et al.* (1981) and *Tobiska* (1991) are currently implemented in GITM. However, most often when using the $F_{10.7}$, the EUV flux is calculated by the EUVAC model, described by *Richards et al.* (1994). EUVAC primarily uses a reference EUV flux based on F74113 reference spectrum measured by a rocket flight on April 23, 1974, during low solar activity ($F_{10.7}$ = 74, $F_{10.7A}$ = 87, where $F_{10.7A}$ refers to the 80-day average $F_{10.7}$ value for surrounding days) and solar variability data obtained from the Atmospheric Explorer E (AE-E) satellite. This is different than previous models by *Hinteregger et al.* (1981) and *Tobiska* (1991), which are based on the reference spectrum SC#21REF. The SC#21REF spectrum was taken from even lower solar activity ($F_{10.7}$ = 68, $F_{10.7A}$ = 70) and was not obtained directly from measurements of the spectrum. Rather, it was inferred from extrapolation of AE-E measurements between 1977 and 1980. By doubling the solar flux below 25 nm (*Richards and Torr*, 1984), the F74113 reference spectrum produces calculated photoelectron fluxes that are in good agreement with the photoelectron Spectrometer Experiments (PES) on AE-E. In addition, the fluxes below 15 nm are multiplied by a factor of 3 to reach agreement with the calculated photoelectron fluxes from *Winningham et al.* (1989). The result is an EUV spectrum based on 37 wavelength bins from 5–105 nm, which were introduced by *Torr et al.* (1979). The spectrum is scaled for solar activity using the $F_{10.7}$ and $F_{10.7A}$ values for the time period of interest. In GITM, the EUVAC model has been modified to include 59 wavelength bins ranging from .1 nm to 175 nm.

When performing realistic studies, GITM can also use measurements of the EUV spectrum provided by SEE, as well as the interpolated dataset provided by FISM. While the resolution of these datasets is 1nm, the data have been re-binned to the 59 wavelength bins in order to make use of the absorption and ionization cross sections provided by *Richards et al.* (1994).

In either case, the amount of energy that gets deposited into the thermosphere per wavelength bin is specified by:

$$Q_{EUV}(\lambda) = \epsilon I_{\infty}(\lambda) exp[-\tau(z, \lambda, \chi)] \sum_{s} \sigma_{abs,s}(\lambda) n_s, \tag{2.37}$$

where ϵ is the heating efficiency, I_{∞} is the EUV flux at the top of the atmosphere, λ is the wavelength, τ is the optical depth, χ is the solar zenith angle, and σ is the absorption cross section. Summing over the entire wavelength range gives the total amount of heat going into the thermosphere at each grid point. In section 1.1.2, the heating efficiency was discussed, and calculated values were given. These values take into account the amount of heat being added to the atmosphere via exothermic chemical reactions. In GITM, this source of heat is calculated self-consistently. Therefore, using the above heating efficiency profiles would result in a double counting of the chemical energy. Instead, a constant value of 0.05 is used (*Chandra and Sinha*, 1973; *Stolarski*, 1976; *Roble et al.*, 1987), which is typical of other global climate models (GCMs) of the thermosphere-ionosphere region that also calculate chemical heating.

2.1.2.2 Chemical heating

As mentioned in Section 1.1.2, exothermic reactions account for most of the energy that goes into heating of the neutral gas. In using the heating efficiencies calculated by *Torr et al.* (1980), it must be assumed that the heating efficiency does not vary with position, local time, or solar zenith angle. Furthermore, profiles are available for 2 distinct time periods, and while they are calculated for solar minimum and maximum conditions, those interested in using the profiles are still left to guess how the conditions of interest relate to the time periods used by *Torr et al.* (1980). This is the reason that, as mentioned above, GITM does not use such a heating efficiency, and instead, the chemical heating is calculated self-consistently, and a constant heating

efficiency value of 0.05 is used to account for other heating processes. The chemical heating calculations are done at the same time as the chemical sources and losses calculation, using energy values given in *Rees* (1989). The major chemical energy sources in GITM are shown in Figure 2.1 and are summarized in Figure 2.2.

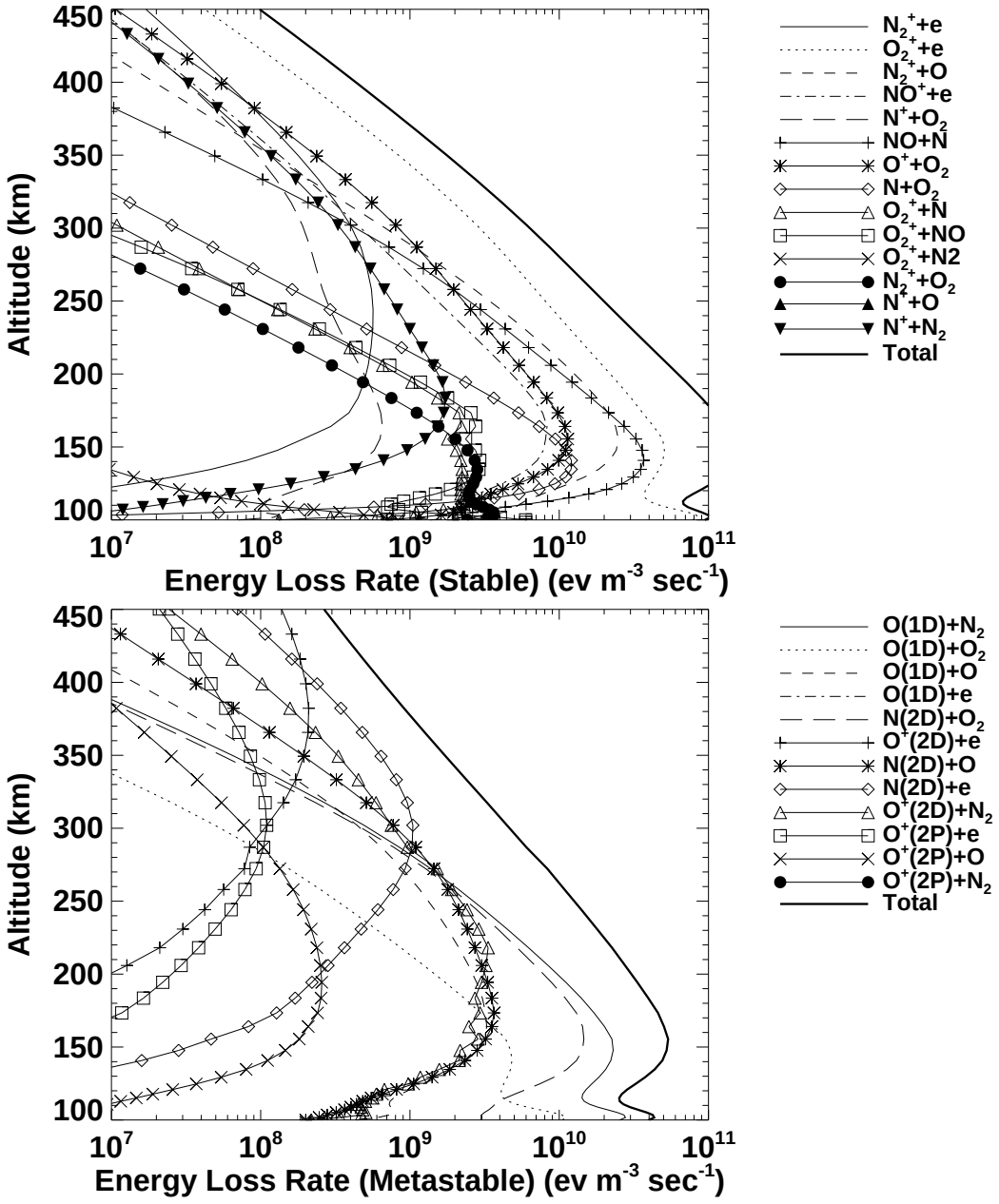

Figure 2.1: The major chemical heating sources in GITM broken up by reactions involving only ground state reactants (top) and reactions involving species in an excited state (bottom).

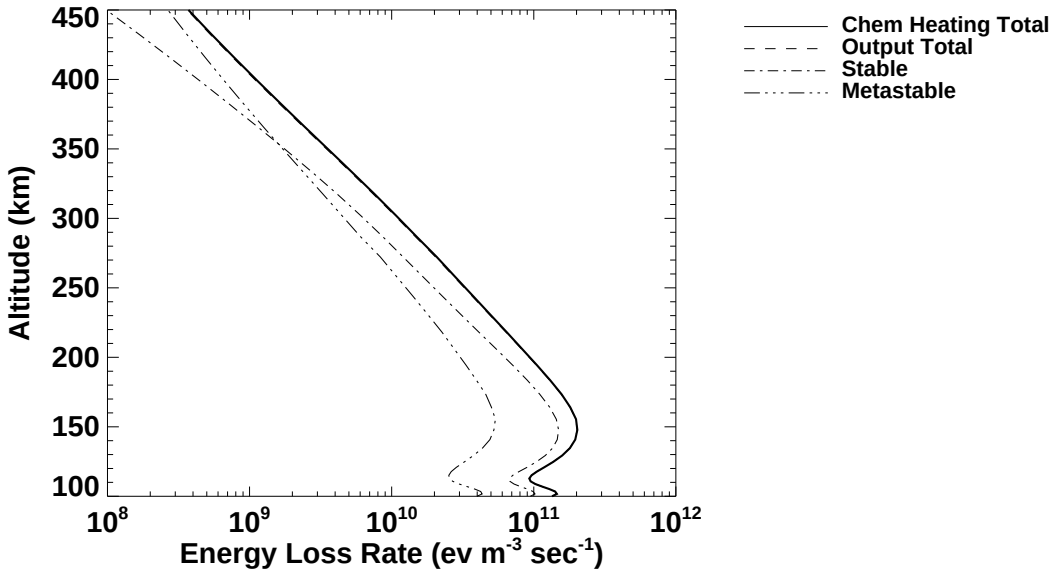

Figure 2.2: Comparison of the chemical heating due to reactions with reactants in their ground states (stable) and reactions with a reactant in an excited state (metastable) along with the total chemical heating rate.

In Figure 2.1, the reactions labeled as stable (top) involve only reactions whose reactants are in their ground state, while those labeled metastable (bottom) involve reactants in an excited state. Throughout much of the thermosphere, most of the heat that goes into the neutrals is due to energy given off during reactions with ground state reactants. Specifically, the reaction:

$$O_2^+ + e \rightarrow O + O \tag{2.38}$$

is the most dominant source of energy throughout the entire thermosphere. However, the stable reactions:

$$NO + N \rightarrow N_2 + O \tag{2.39}$$

$$N_2^+ + O \rightarrow NO^+ + N(2D) \tag{2.40}$$

and metastable reactions:

$$O(1D) + N_2 \rightarrow O + N_2 \tag{2.41}$$

$$N(2D) + O_2 \rightarrow NO + O \tag{2.42}$$

are important in the lower thermosphere, while the stable reactions:

$$O^+ + O_2 \rightarrow O_2^+ + O \tag{2.43}$$

$$N_2^+ + e \rightarrow N + N \tag{2.44}$$

and metastable reactions:

$$N(2D) + O \rightarrow N + O \tag{2.45}$$

$$O^+(2D) + N_2 \rightarrow N_2^+ + O \tag{2.46}$$

$$O^+(2D) + e \rightarrow O^+(4S) + e \tag{2.47}$$

become important higher up. By about 360 km, reactions involving species in an excited state dominate the chemical heating.

2.2 Uncertainty involved with using parameters

When modeling the ionosphere-thermosphere system, it is important to understand the sources of uncertainty within the model. Perhaps the most important source of uncertainty stems from the fact that the ionosphere-thermosphere system is highly externally driven. In other words, given adequate time, the initial conditions of the system should have little to no effect on the end state of the system. This is primarily a result of the coupling between the Earth's upper atmosphere and the magnetosphere as well as the sun (*Kamide and Baumjohann*, 1993; *Lu et al.*, 1995;

Khazanov et al., 2003). Dynamics in these two external systems have a profound effect on the state of the ionosphere and thermosphere. Thus, when attempting to model the system, it is critical to accurately account for the forcing due to these sources. For example, it would be impossible to sustain an ionosphere without specifying the solar radiation flux, regardless of the initial ionospheric conditions. There is a great deal of work throughout the community attempting to accurately specify the important sources of energy and momentum to the upper atmosphere (*Fuller-Rowell and Evans*, 1987; *Woods et al.*, 2005; *Solomon and Qian*, 2005; *Chamberlin et al.*, 2007; *Ridley*, 2005).

In addition to the external drivers, there are other sources of uncertainty. In some cases, there is underlying physics in the system that is important and needs to be accounted for, but is not completely understood, e.g. eddy diffusion. In other cases, the physics may be understood, but it may be too complicated to take into account given the scale of problem trying to be solved. The heating efficiency is an example of such physics. In either case, models must approximate the real system through the use of parameterizations. In today's GCMs of the Earth's upper atmosphere, many parameters are used to specify a variety of rates and coefficients. Parameters are used to specify sources in the energy equation, such as heating efficiencies and conductivities, the momentum equation, such as diffusion coefficients, and the mass continuity equation, such as reaction rates. While many of these parameters have been studied in detail, whether through laboratory or computational experiments, the use of any of them is subject to some uncertainty, since it is impossible to test each parameter in all possible scenarios.

It is unrealistic to expect that models always provide the correct answer to every problem, and it is in uncovering why the answer is wrong that new physics can be deduced. In order to better understand the results from a model and to use the results to provide insight into the physical processes that are not understood, it is

important to evaluate the uncertainty in the results. This is done here for GITM in order to show which parameters have the largest effect on the thermosphere, and to quantify the uncertainty introduced into the results through the use of such parameters. Specifically, the effect of 8 of the most important atmospheric parameters on the results is studied under solar minimum and solar maximum conditions. In addition, the time-dependent effects of the parameters are studied during a geomagnetic storm.

2.2.1 Parameters

For this study, the uncertainty involved with the use of eight different thermospheric parameters is investigated. The parameters examined are the thermal conductivity (*Schunk and Nagy*, 2000) , eddy diffusion coefficient (*Blum and Schuchardt*, 1978; *Brasseur and Offermann*, 1986; *Fuller-Rowell and Rees*, 1992), turbopause altitude (*Blum and Schuchardt*, 1978; *Hall et al.*, 2008), NO binary diffusion coefficient, N_2 photodissociation branching ratio (*Rees*, 1989; *Schunk and Nagy*, 2000), NO^+ recombination branching ratio (*Torr et al.*, 1976; *Rees*, 1989; *Marsh et al.*, 2004), O^+ recombination rate, and the nitric oxide (NO) dilution factor for NO cooling (*Kockarts*, 1980). These represent only a subset of the parameters involved in the model. One of the reasons that these parameters have been selected is that each of them has some uncertainty. The goal of this study is to show how this uncertainty affects the results.

The other reason these parameters are selected is because each of them is significant with regard to the calculation of the neutral gas temperature. Each of the terms in Equation 2.35 contributes to the total uncertainty in the model, since each term itself contains some uncertainty. The solar, particle, and Joule heating terms are directly driven by external forcing (i.e., magnetospheric electric fields, particle precipitation, as well as the solar EUV flux), therefore, most of the uncertainty in the results due to these terms is not contained within GITM itself, but rather in

the data or model results used to drive GITM. However, the radiative cooling and the conductive terms do depend on the internal dynamics of the model, and thus uncertainty in these terms can be quantified. Each of the parameters addressed in this study have an effect on one of these three terms, either though a coefficient used directly in the calculation of the temperature, or because the parameter either directly or indirectly causes compositional changes, which affects the radiative cooling rates. In order to quantify the effect that each of these parameters has on the upper atmosphere, GITM is run several times for each parameter. Each time, the value of the parameter is changed within the limit of published values. Table 2.2 summarizes these values.

It is important to point out that in GITM, the eddy diffusion coefficient transitions from a constant value below some pressure level, P_1, to a value of zero above some pressure level, P_2. This is demonstrated in Figure 2.3 due to its consequences for the turbopause simulations. Changing the pressures at which this transition occurs is not the same as directly changing the location of the turbopause, since the turbopause is not directly calculated by GITM. However, the location of the turbopause will change as a result of the values of the pressures being different. Therefore, comparison of these simulations, in effect, compares the location of the turbopause, and thus, they are referred to "turbopause" simulations in the text.

#	Parameter	Formulation	Label	Value	Reference
1	Thermal conductivity	$\lambda = \sum_{i=O,O_2,N_2} \frac{[N_i]}{[N_{total}]} A_i T^s$		[a]A(O_2)=A(N_2)=3.6x10^{-4}	*Schunk and Nagy* (2000)
			1	A(O) = 5.6x10^{-4}	
				s = .69	
				A(O_2)=A(N_2)=3.6x10^{-4}	
			2	A(O) = 5.6x10^{-4}	
				s = .75	
				A(O_2)=A(N_2)=5.6x10^{-4}	
			3	A(O) = 7.6x10^{-4}	
				s = .75	
2	Eddy diffusion coefficient		1	100.0 m^2/s	*Blum and Schuchardt* (1978),
			2	50.0 m^2/s	*Brasseur and Solomon* (1986),
			3	200.0 m^2/s	*Fuller-Rowell and Rees* (1992)
3	Turbopause altitude	Linear transition between pressures P_1 and P_2	1	Figure 2.3 solid line	*Blum and Schuchardt* (1978),
			2	Figure 2.3 dotted line	*Hall et al.* (2008)
			3	Figure 2.3 dashed line	
4	NO binary diffusion coefficient		1	910.0 m^2	
			2	450.0 m^2	
5	N_2 dissociation branching ratio	$N_2 \rightarrow$ f_{4s}N(4S) + f_{2d}N(2D)	1	f_{4s}=0.5, f_{2d}=1.5	*Rees* (1989),
			2	f_{4s}=1.0, f_{2d}=1.0	*Schunk and Nagy* (2000)
			3	f_{4s}=0, f_{2d}=2.0	
6	NO^+ recombination branching ratio	$NO^+ \rightarrow$ f_{4s}N(4S) + f_{2d}N(2D) + O	1	f_{4s} = 0.2, f_{2d} = 0.8	*Rees* (1989)
			2	f_{4s} = 0, f_{2d} = 1.0	*Marsh et al.* (2004)
7	O_2^+ recombination rate	$O^+ \rightarrow$2O	1	[b]rr = 1.9x$10^{-13}(\frac{T_e}{300})^{-0.5}$	
			2	rr = 2.4x$10^{-13}(\frac{T_e}{300})^{-0.7}$	
			3	rr = 1.9x$10^{-13}(\frac{T_e}{300})^{-0.7}$	

Table 2.2 Continued

#	Parameter	Formulation	Label	Value	Reference
8	NO Cooling	ω=k[O]/(k[O] + 13.3)	1	k=3.3x10^{-18} m^3/s	*Kockarts* (1980)
			2	k=6.5x10^{-17}m^3/s	
			3	k=3.6x10^{-17}m^3/s	

Table 2.2: Parameters in GITM that have an effect on the thermospheric temperature along with the values used for this study. In cases where the implementation is not standard, the current formulation used in the model is shown. The label column is used to reference which parameter set is used in the text in a simple manner. For example, in the text, the conduction 1 simulation refers to the first set of parameters in the table, etc.

[a]Units for the coefficient A are J/(m s K).
[b]Units for the reaction rates are m^3.

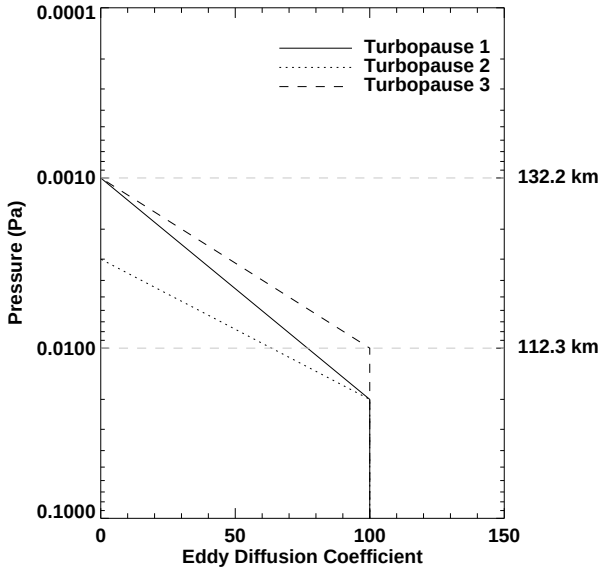

Figure 2.3: Plot of the vertical profile of the eddy diffusion coefficient for each of the turbopause cases (units m^2/s).

2.2.2 Results

2.2.2.1 Steady-state simulations

As a first look at the effect of these different parameter values, GITM is run under solar minimum and solar maximum conditions to see how the results differ when the model is in steady-state. In these simulations, GITM is initialized using MSIS (neutral) and International Reference Ionosphere (IRI) profiles and then run for 24 hours. In the solar minimum case, GITM is run with a $F_{10.7}$ of 87.8 W/(m^2 Hz) and during the solar maximum case, GITM is run with a $F_{10.7}$ of 240.6 W/(m^2 Hz). The high-latitudes are driven by constant low values that are the same for solar minimum and solar maximum. The hemispheric power index (HPI) is specified to be 1.0 and the cross polar cap potential patterns are specified by the Weimer model (*Weimer*, 1996) using interplanetary magnetic field values of B_y = 0.0 nT and B_z = -2.0 nT and a radial solar wind velocity of 400 km/s. In all cases, all inputs are identical between the runs except for the particular parameter being investigated.

Solar minimum

Figure 2.4 shows a comparison between the parameter values of the global averaged neutral temperature profile for GITM under solar minimum solar conditions. During solar minimum, the parameters that have the most impact on the results are conduction, NO cooling, and to a lesser degree, NO diffusion. For the conduction simulations, at 400 km, the global average temperature varies by 30% between values of 789.8 K and 1023.7 K. Depending on the conductivity applied, the increased exospheric temperature in the conduction 1 and 2 simulations is expected because lower conduction values are used, causing less energy to be transported down in the atmosphere. The other two parameters that significantly affect the temperature, NO cooling and the NO binary diffusion coefficients, result in a range of exospheric temperatures of 14% and 3.2% respectively. The eddy diffusion, N_2 dissociation, and O_2^+ simulations result in a range of less than 1%.

The NO cooling 1 simulation uses a value for the dilution factor, ω, that is at least an order of magnitude smaller than the other values. This means that the NO cooling is essentially shut off in this simulation. While this is unrealistic, the results help shed light into the overall effect of NO cooling, and provide a means by which to gauge the performance of the parameterization. When a value of ω of $6.5\text{x}10^{-17}(\text{m}^3/\text{s})$ is used, NO cools the atmosphere on a global scale by 14% relative to the NO cooling 1 simulation, and when a value of $3.6\text{x}10^{-17}(\text{m}^3/\text{s})$ is used, NO cools the atmosphere by 11%.

Solar Maximum

Figure 2.5 shows a similar plot to Figure 2.4 for solar maximum conditions. The results in the solar maximum case are similar to the solar minimum case except that the uncertainty in the results is slightly larger for each of the parameters. The conduction results for the exospheric temperature show a range of 35.5% with values

of 1218.7 K and 1651.4 K and the NO cooling simulations show a range of 24.1% Again, the NO diffusion has a smaller, but significant, effect of 4.8%. As is the case for solar minimum, the other parameters, result in a difference of 1% or less.

2.2.2.2 Geomagnetic storm simulations

In order to perform a more in-depth analysis of how these parameters affect the upper atmosphere during a more dynamic time period, the model is run during the May 15, 2005 storm, which reached a Dst (storm time disturbance index) value of -263 nT. This storm was selected because it is relatively isolated from other geomagnetic disturbances and because it occurred during moderate solar conditions ($f_{10.7} \sim 110$). For this case, GITM is driven using the Weimer potential model and *Fuller-Rowell and Evans* (1987) particle precipitation patterns, using HPI data as well as observed solar wind and interplanetary magnetic field data to simulate the upper atmospheric response to the storm.

Temperature

Figure 2.6 shows thermospheric density results throughout the 2005 storm along with inferred density observations from the Champ satellite (*Reigber et al.*, 2000) for reference. The GITM results are extracted at the same position as the Champ satellite (approximately 400 km) and the orbit averaged values are plotted. Only the results from the conduction, NO cooling, and NO diffusion simulations are plotted since these parameters result in the largest pre-storm uncertainty. Figure 2.6 shows that the different parameters can have an effect during both quiet-time and storm-time. As is the case in Figures 2.4 and 2.5, the conduction has the largest effect on the results under steady conditions (pre-storm). This is also the case during the storm. The base-to-peak difference of the mass density for the 3 simulations is 13.7, 13.0, and 9.9 kg/m^3, respectively. A similar trend takes place during the recovery of the

storm, when the peak-to-recovered difference values are 13.0, 12.6, and 9.7 kg/m^3, respectively, indicating that when a lower conductivity value is used, the thermosphere recovers faster. This result demonstrates the non–linear nature of the thermosphere. During the storm's main phase, the lower conductivity allows the temperature (and thus density) to increase more than when a large value is used. Since the thermosphere is more dense at all altitudes, there is more NO at all altitudes, and this extra NO leads to enhanced radiative cooling, allowing the thermosphere to recover faster after the main phase.

The NO diffusion simulations do not show as much of a change in the thermospheric response during storm time compared to quiet time, rather, there is only a slight difference between the maximum values that occur during the main phase of the storm and the pre-storm density between the 2 simulations (10.6 kg/m^3 for case 1 and 11.9 kg/m^3 for case 2). The NO cooling cases, on the other hand, further indicate how important NO cooling is to the recovery of the thermosphere. As the NO cooling is turned down, the system recovers more slowly. This is clearly evident when comparing case 1 to the other cases. At the end of May 17^{th}, the density in case 1 is still 51% higher than before the storm. This is significantly larger than the 13% and 16% difference between the density at the end of the storm and before the storm for cases 2 and 3 respectively. To summarize the effect each parameter has on the thermosphere during the storm, Table 2.3 shows the base-to-peak density difference for all of the parameter cases discussed.

The eddy diffusion simulations result in a relatively large difference between the pre-storm and peak density values for each of the cases. The eddy diffusion coefficient affects the temperature by helping to determine the NO density, and therefore the total radiative cooling. Increasing the eddy diffusion results in more NO at higher altitudes. This is similar to increasing the NO binary diffusion coefficient, and thus it is reasonable to expect that the results from increasing the two parameters has

Parameter	Case 1		Case 2		Case 3	
	%	Diff	%	Diff	%	Diff
Conduction	266.9	13.7	395.0	13.0	557.5	9.9
Eddy	364.7	11.9	348.6	12.1	403.3	11.1
Turbopause	408.0	10.5	421.3	10.9	417.3	10.3
NO Diffusion	406.4	10.6	280.4	11.9	N/A	N/A
N_2 Dissociation	360.7	11.9	352.5	12.1	384.2	11.5
NO^+ Recombine	366.0	11.2	360.2	11.8	N/A	N/A
O_2^+ Recombine	381.4	11.8	412.5	12.9	412.5	12.9
NO Cooling	203.0	21.4	380.4	11.9	344.6	13.0

Table 2.3: Percent difference and absolute difference (10^{-12} kg/m^3) between the pre-storm global average mass density and the maximum global average mass density for each case of each parameter category for the May 2005 event.

a similar affect on the uncertainty. Compared to the other parameter cases, the turbopause altitude, N_2 dissociation, and recombination reactions do little to affect the temperature.

In order to more quantitatively assess the effect of the parameter values on the simulation results, Figures 2.7 - 2.9 each show a histogram of temperature values at 400 km throughout the 2005 storm. Again, only the conduction, NO cooling, and NO diffusion simulations are shown since they result in the largest difference between the cases. The y-axis of each histogram plot shows the total number of counts in a particular bin divided by the total number of temperature measurements as a percentage. In Figure 2.7, four histograms are shown, one for the global temperature, day-side temperature, night-side temperature, and high-latitude temperature. Each of these are made by taking each grid cell in the particular region, at every output time step (.5 hours), and counting the number of occurrences for each temperature bin. Since the histograms are formed using the data at every time step, the information contained in dynamics that result from the storm are included in each plot.

The conduction histograms for temperature reinforce the conclusions derived from Figures 2.4, 2.5, and 2.6 that uncertainty in the conduction has a significant effect on the results. Qualitatively, the temperature distribution is similar between each of the

cases, and changing the conduction simply results in a shift in the temperature. Globally, the mean temperatures for cases 1, 2, and 3, respectively are 1188.2 K, 1025.7 K, and 888.9 K and the standard deviations are 87.5 K (7.4% of mean temperature), 75.6 K (7.4%), and 67.8 K (7.6%). Since cases 2 and 3 use the same exponent and only a different compositional constant in the conductivity calculation, they are easiest to compare. Between the two cases, the conductivity changed by approximately 30%. This change leads to a 15% difference in the exospheric temperature. If case 1 is included, the resulting range of exospheric temperatures is more than 33%.

In the other three regions, the mean temperature also has a range of 33% which indicates that, on average, the conduction affects the thermosphere in the same manner regardless of position. This makes sense because at the most fundamental level, the conduction determines only the amount of energy transported vertically. On the day-side and night-side, the distributions are slightly broader than they are globally, and the conduction values do seem to have a small effect on the distribution itself. Specifically, on the day-side, cases 1, 2, and 3 have standard deviations of 8.9, 9.6, and 10.7% of the respective mean temperature. There is a similar trend on the night-side, where the deviations are 9.6, 10.7, and 12.2% respectively. At high-latitudes, the standard deviation values are almost identical to the global values.

Some of the effects of the storm can be seen by looking at the secondary peaks that form at higher temperature that occur in all of the histograms, but most dominantly in the global, night-side, and high-latitude plots. These peaks occur as a result of the storm depositing massive amounts of energy into the high-latitude regions, which launches large scale waves that travel around the atmosphere for many hours after the storm occurs. It is interesting that a secondary peak occurs on the night-side, but not on the day-side. This is a result of a traveling disturbanced launched from high-latitudes converging at low-latitudes on the night-side. The effect of this wave is diminshed on the day-side because the wave must propagate in a direction anti-

parallel to the nominal day-to-night winds.

The NO cooling temperature histogram is shown in Figure 2.8, which further shows the importance of NO cooling to the thermospheric heat budget. Only the global histogram is shown since the other regions show similar trends. As mentioned previously, case 1 shows the thermospheric temperature when NO cooling is nearly turned off. The global mean temperature is more than 350K warmer. In addition, the spread of the distribution is more than a factor of 2 larger in this case. This is primarily due to the lack of recovery during the storm. The narrower secondary peaks that occur at higher temperature in the other cases indicate a faster recovery.

In Figure 2.9, the global temperature histogram for the NO diffusion cases are shown. The NO diffusion affects the temperature in a similar way as the conduction, in that a change in the diffusion coefficient results in a shift in the temperature, but the distribution itself remains similar. However, the magnitude of the shift is substantially smaller. The difference between the mean temperature in cases 1 and 2 is just 5.7% (compared to 33% for the conduction cases).

The inset in Figure 2.9 shows the difference between the NO altitude profiles during the storm in order to explain more thoroughly the cause of the temperature difference between the 2 cases. The diffusion values used in case 2 are half of those used in case 1. This means that in case 1, the NO molecules are more strongly tied to the bulk motion of the atmosphere. At the bottom of the model, where the molecular weight of NO is very close to the mean molecular mass, since the atmosphere is mostly N_2, the NO velocity is similar in both cases. However, as altitude increases, the mean molecular mass decreases due to the relative importance of atomic oxygen, and thus the NO velocity tends to be increasingly negative compared to the bulk flow. At these altitudes, then, the diffusion coefficient will have an overall effect on the velocity. Above 130 km, the NO downward velocity is more restricted by collisions with the bulk flow in case 1 compared to case 2, and therefore the [NO] is smaller in

case 2 at this altitude. Since NO cooling becomes efficient between 140 and 200 km, due to the presence of atomic oxygen (*Kockarts*, 1980), the temperature is cooler in case 1 than in case 2.

N_mF_2 and composition

The other parameters in this study all have a minimal effect on the temperature. The resulting temperature range for each of the cases is approximately 1% for each of the other sets of parameters and the standard deviations for the other parameter sets are within 2% of the mean temperatures. Still, there are some other interesting results that occur due to uncertainty in the other parameters. Figure 2.10 shows histograms of N_mF_2 during the December 2005 event for the three eddy diffusion cases. While the peaks that occur between 3.0e11 and 7.0e11 e^-/m^3 are affected by the different eddy diffusion values at all locations, it is interesting that the tails of the day-side and night-side histograms are affected the most by the different coefficients. On the day-side, when an eddy coefficient of 50 m^2/s is used, the maximum N_mF_2 values obtained are nearly 40% larger than when an eddy coefficient of 200 m^2/s is used. Similarly, on the night-side, a coefficient of 50 m^2/s leads to maximum N_mF_2 values that are 20% larger than when 200 m^2/s is used.

This amount of uncertainty in the N_mF_2 results from varying the eddy diffusion coefficient, which changes the amount of vertical mixing in the thermosphere. For a higher eddy coefficient, the individual species are not allowed to diffuse according to their own scale height as easily, and thus at a given altitude above the turbopause, a higher eddy coefficient will result in a thermosphere that, compositionally, more closely resembles the turbopause than when a lower coefficient is used (*Sinha and Chandra*, 1974). In other words, for a given altitude, (above the nominal turbopause) the higher the eddy coefficient, the lower the O/N_2 ratio. Figure 2.11, which shows a histogram of the O/N_2 ratio for the three eddy diffusion cases, indicates that this is

the case for these simulations, and suggests that any differences in the N_mF_2 may be due to the change in the diffusivity of the lower thermosphere, since the O/N_2 ratio determines, to a large part, the production and loss of electrons (*Mayr et al.*, 1978; *Prölss and Jung*, 1978).

Another feature of the eddy coefficient N_mF_2 histograms is that on both the day-side and night-side, the difference between each case occurs throughout the duration of the simulation, not just during the storm. As mentioned above, it is the tail region of the histograms that are most affected. This corresponds to the region of the day-side and night-side ionosphere that is the most ionized, or the equatorial region. In this region, the electrons are trapped on nearly horizontal field lines, and thus it is difficult for the F2 layer to shift in altitude, and thus it is unlikely that vertical motion of the ionosphere is contributing to the change in production and loss of electrons, which would occur mainly during storm time (*Jones and Rishbeth*, 1971). This is indeed the case here as the results show that for the three diffusion cases, there is no difference in the vertical ion velocity during the 2005 event (not plotted).

The effect of increasing the eddy coefficient should be similar to the effect of increasing the turbopause altitude, and therefore, it is expected that compositional changes should be observed. While this is the case, the values used for the turbopause altitude in this study lead only to a slight change in the mean O/N_2 ratio (a lower value of 0.47 compared to a upper value of 0.48). This range is small compared to that of the eddy coefficient, which has a range of over 20% (a lower value of 0.44 and an upper value of 0.54). In terms of atmospheric global circulation models, uncertainty in the eddy diffusion coefficient is much more important than the uncertainty in the location of the turbopause.

2.2.3 Discussion on uncertainty in the model

In the previous section, the effect of uncertainty in the parameters used in GITM was investigated. Specifically, the model was run using different values for eight parameters that have an effect on the neutral energy equation. It was found that uncertainty in the thermal conduction has the most drastic impact on the temperature and density results. In addition, while not as substantial as the thermal conduction, uncertainty in the NO cooling parameterization and NO binary diffusion coefficients also have a significant effect on the temperature. By means of differences in the composition, increasing the eddy diffusion coefficient by a factor of 2 can result in a 20% decrease in the electron density in the most charged parts of the upper atmosphere. While a compositional change occurs when the altitude of the turbopause is varied, uncertainty in the altitude is small enough that the compositional effects are not large enough to have a significant effect on the ionosphere. In this study, GITM indicates that variations in the other parameters, NO^+ recombination, O_2^+ recombination, and the N_2 dissociation branching ratio do not have a substantial effect on the large scale atmospheric quantities.

During a storm, GITM indicates that NO plays a crucial role in maintaining the thermospheric density. When the NO cooling is dramatically reduced, the modeled thermospheric density increases by much more during the main phase than when a more realistic NO cooling parameterization is implemented. Also, during recovery, the density takes much longer to return to a background state when the NO cooling is reduced. While these effects are most prominent when the NO cooling dilution factor was varied, the physical process that effects the temperature, and thus the density, is simply how much energy is radiated away. In this case, any parameter that has a measurable effect on the radiative cooling will effect the large scale variables in a similar way.

Global models of the thermosphere use many more parameters than those ad-

Parameter	Typical GITM Value
Thermal conductivity	$A(O_2)$=$A(N_2)$=3.6x10^{-4}
	A(O) = 5.6x10^{-4}
	s = .75
Eddy diffusion coefficient	100 m^2/s
Turbopause Altitude	Figure 2.3 solid line
NO binary diffusion coefficient	910 m^2
N_2 dissociation branching ratio	f_{4s}=0.5, f_{2d}=1.5
NO^+ recombination ratio	f_{4s}=0.2,f_{2d}=0.8
O_2^+ recombination rate	1.9x10^{-}13$(\frac{T_e}{300})^{0.5}$ m^3/s
NO Cooling dillusion factor	k=6.5x10^{-}17m^3/s

Table 2.4: Values used for GITM simulations

dressed here. In the previous section, only a handful of those that directly affect the thermosphere and ultimately the energy equation were investigated. There are many more that are more pertinent to the momentum and mass continuity equations, as well as the ionosphere itself. This study is meant to shed light into the scale of the uncertainty involved with using such parameters in the modeling community, but is also specific to GITM. The results allow pertinent science to be performed using the model with an understanding of the magnitudes of uncertainty involved. Further, when compared with data, the results indicate the best combination of parameters to use in other studies, such as those included in this thesis. In the following chapters, the impact of solar flares on the global thermosphere is examined in detail. All of the simulations performed use identical values for the parameters mentioned in this section, given in Table 2.4. While the goal of the study is to understand the fundamental processes that dominate the response to flares and not to perfectly match observations, it is still important to simulate the system in a manner that is as consistent as possible with reality.

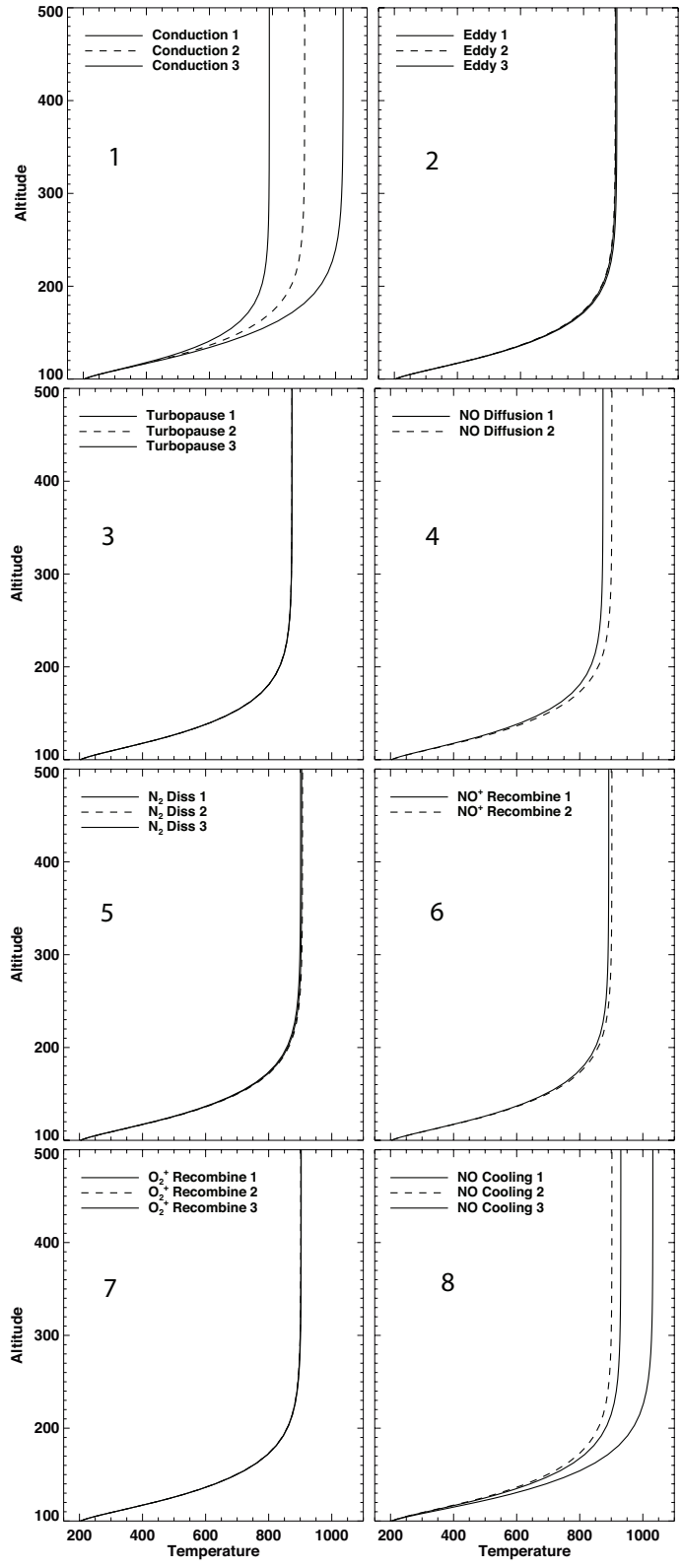

Figure 2.4: Global average temperature for solar minimum conditions. Each panel shows a comparison between the different values in each parameter category. The numbers in each panel correspond to each of the 8 parameters in table 2.2

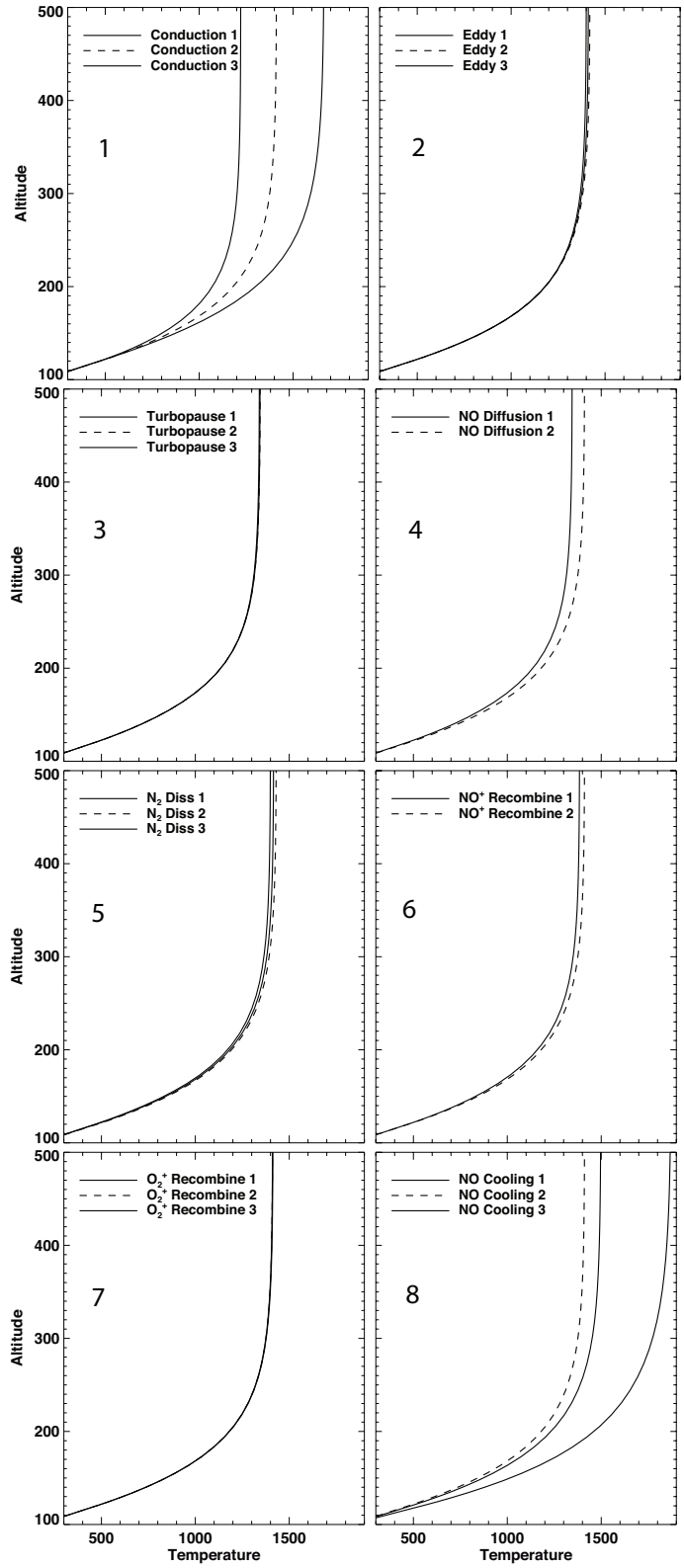

Figure 2.5: Global average temperature for solar maximum conditions. Each panel shows a comparison between the different values in each parameter category.

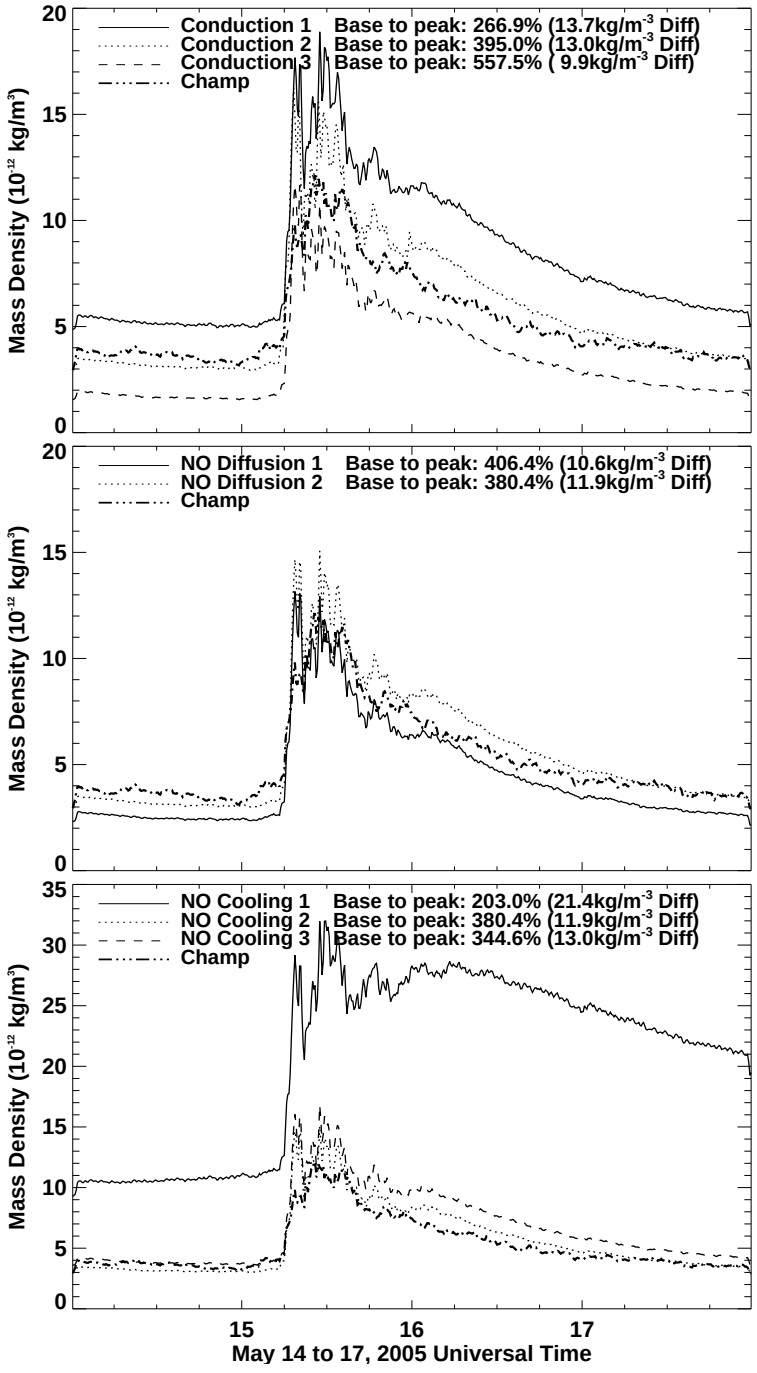

Figure 2.6: The orbit averaged thermospheric density results at the Champ position. The Champ observational data is also plotted. Note that the y-axis range on the NO cooling plot is larger than on the other plots.

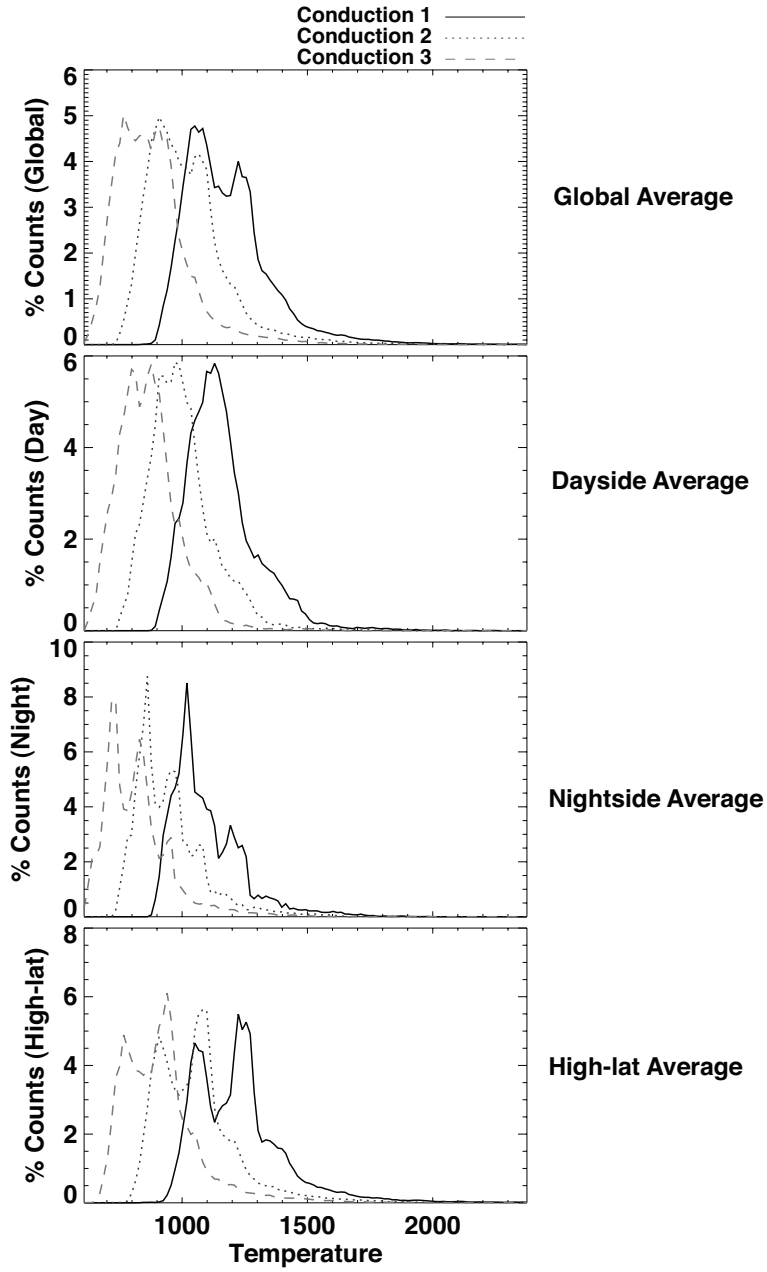

Figure 2.7: Histogram of temperature (K) during the December 2005 event for each of the conduction cases. Histograms are calculated globally (top), for the day-side (second from top), for the night-side (second from bottom), and for the high-latitudes (bottom).

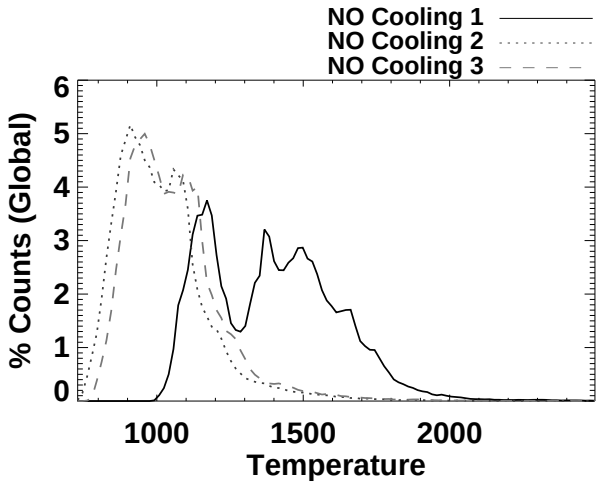

Figure 2.8: Histogram of global temperature (K) during the December 2005 event for each of the NO cooling cases.

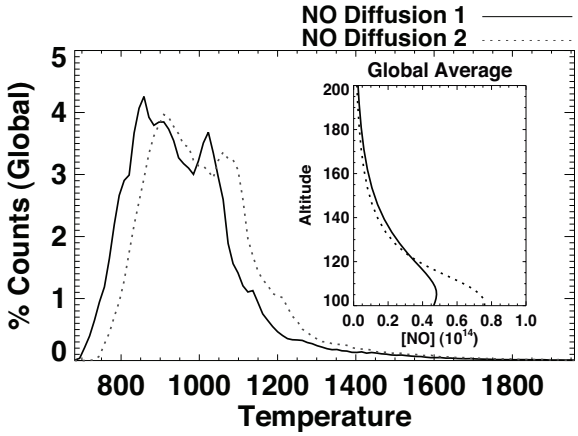

Figure 2.9: Histogram of global temperature (K) during the December 2005 event for each of the NO diffusion cases. The inset shows an altitude profile of the NO density at 12 UT on May, 15 2005 for each case.

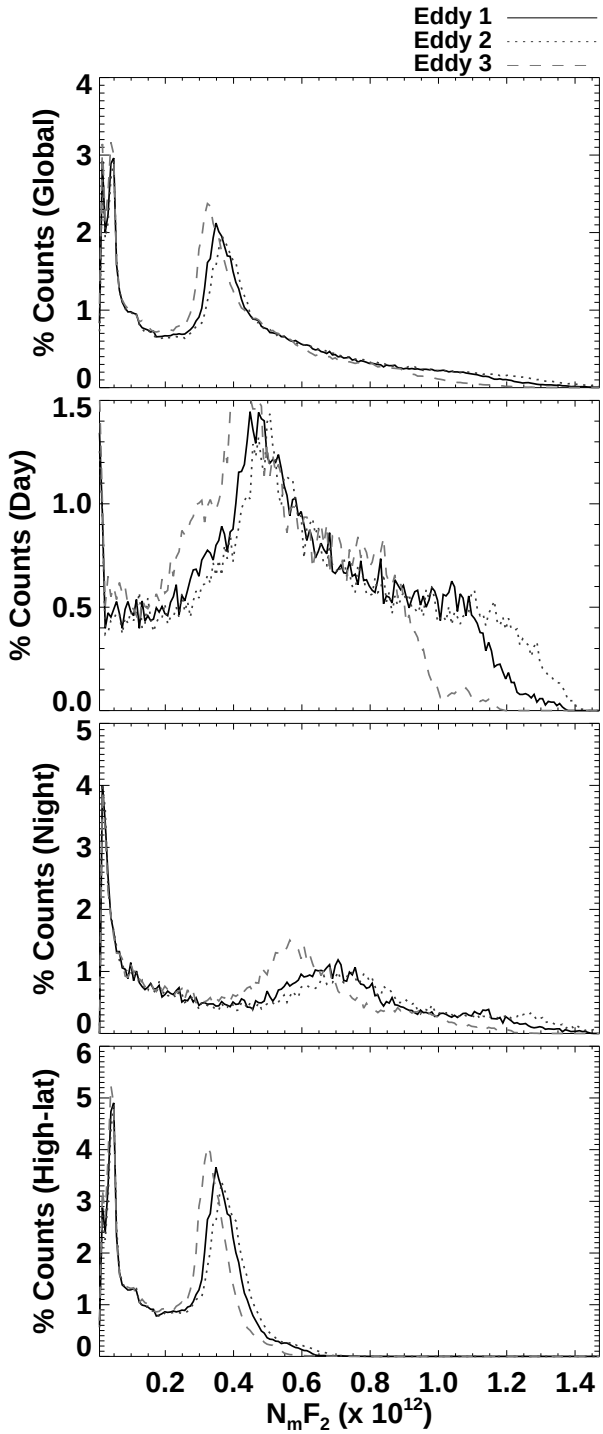

Figure 2.10: Histogram of global (top), day-side (second from top), night-side (second from bottom), and high-latitude (bottom) N_mF_2 during the December 2005 event for each of the eddy diffusion cases.

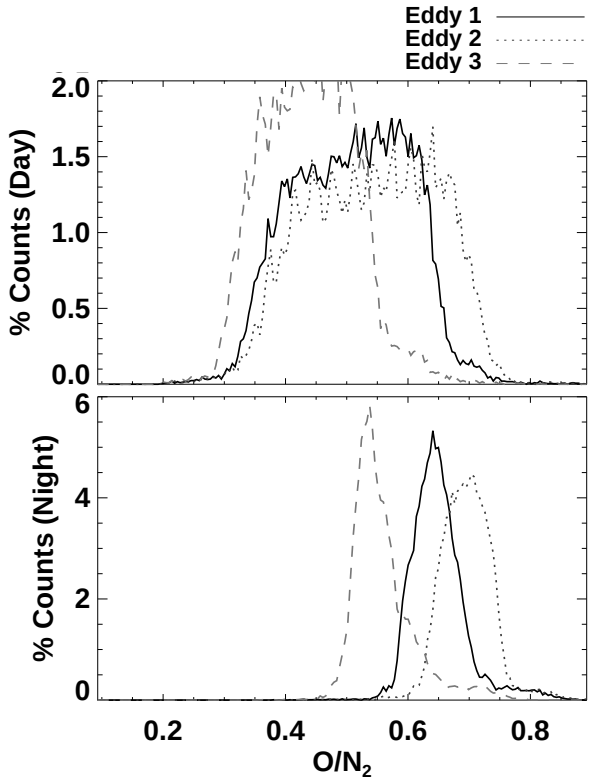

Figure 2.11: Histogram of day-side (top) and night-side (bottom) O/N_2 ratio during the December 2005 event for each of the eddy diffusion cases.

CHAPTER III

The Global Response to Large Flares

In this chapter, GITM is used to investigate the thermospheric response to two realistic solar flares, the X17 Halloween flare that occured on October 28, 2003, and a X0 flare which occured on November 6, 2004. In order to perform a detailed and accurate analysis of the thermospheric response to real solar flares, the model must be driven by measurements of the EUV and soft X-ray flux. As mentioned in section 1.2.1.1, one of the issues with using the SEE data to accomplish this is the instrument only has a 3% duty cycle on-board TIMED, which equates to approximately one observation every 90 minutes. Therefore, in order to study the response to a solar flare, the SEE data needs to be interpolated. For this study, this is accomplished simply assuming an exponential decay during the recovery of a solar flare. When GITM reaches the first SEE data point during a flare, the solar spectrum is then calculated at every time step for the duration of the flare using an exponential interpolation. This interpolation is calculated by determining the decay rate between the two closest data points surrounding the current time in the simulation, and utilizing that rate to calculate the flux at the current time. This method does not require any knowledge of how the EUV wavelengths correlate to the X-rays, as is the case when using the GOES X-ray data as a proxy, such as when using FISM. The only remaining issue is that due to the sparsity of the SEE data, there

may be significant error in specifying when the flare begins. Since SEE observations are made every 90 minutes, it is possible that the timing of the flare is off by as much as 90 minutes. Therefore, it is necessary to use the GOES data to determine the start time of the flare. The top panels in Figure 3.1 show the solar flux at .5 nm calculated using the SEE measurements on October 28, 2003 (left) and November 6, 2004 (right). The dashed line shows the flux that would drive the model if only the raw SEE data are used without any interpolation. If the start time of the flare is specified in GITM using the GOES data (bottom of Figure 3.1), and an exponential interpolation is performed between SEE data points, the solid line is obtained. By specifying the start time, GITM will simulate the October flare about 20 minutes before it would otherwise, and the November flare, an hour and a half earlier. After approximately six hours, the SEE data are no longer interpolated.

One possible source of error in using the SEE data is due to the approximate 10% uncertainty in energy input given by the instrument (*Woods et al.*, 1998). This may lead to a errors in both the temporal dynamics and strength of the thermospheric model reaction to the solar flare. In addition, no assumptions are made about the solar flux prior to the first SEE measurement during the flare. Rather, the study uses a very conservative approach to interpolating the SEE data. When the simulated time reaches the start time of the flare, the EUV flux increases to the value obtained from the first SEE measurement during the flare, even though the actual flux is almost certainly larger, since the measurement is in the future. This is the case for both the October 28^{th} event, where the first SEE measurement of the flare is only a few minutes after the actual start of the event, and the November 6^{th} event, where the first SEE measurement is nearly an hour and a half after the actual start of the flare. While simulating both events in this manner will lead to an underestimatation of the incident energy into the thermosphere, the amount of energy missed during the November event is likely much larger than the energy missed during the October

event due to the timing of the SEE measurements. However, the goal of this study is not to determine the exact thermospheric perturbation during a specific solar flare, but rather to obtain insight into how the thermosphere responds globally, using a minimum of assumptions about the solar flux, so this underestimation is acceptable. A brief comparison of the model results with data from the Champ satellite, which is described by *Reigber et al.* (2000), is presented in section 3.1.3, however, the studies by *Sutton et al.* (2006) and *Liu et al.* (2007) attempt to accurately quantify the density response during the October 2003 flare using in-situ accelerometer data.

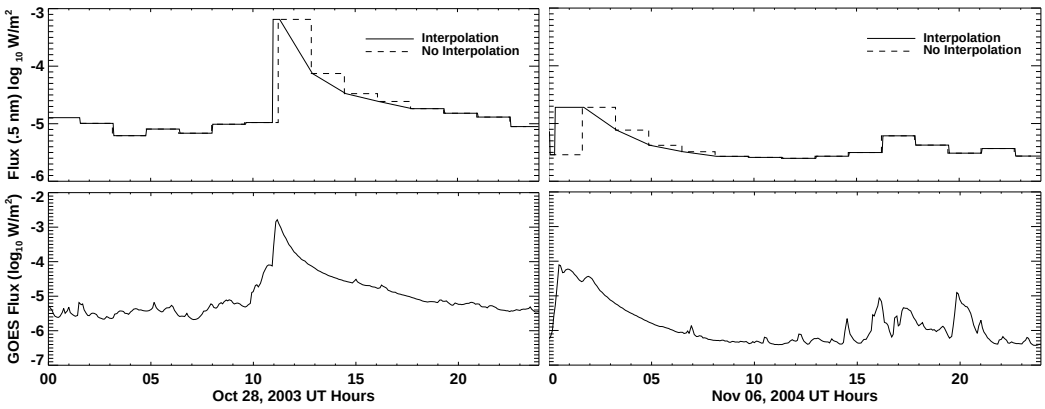

Figure 3.1: (Top) Log_{10} solar flux at .5 nm on Oct 28, 2003 (left) and Nov 6, 2004 (right). The dashed line represents the flux obtained using raw SEE data and the solid line is the flux after performing an exponential interpolation during the flare and specifying the start time of the flare. (Bottom) Log_{10} solar flux from GOES 1-8 angstrom channel for the same days.

3.1 The Global Thermospheric Response

For this study, GITM is run at a resolution of 5° latitude × 5° longitude, and is initially run for 24 hours prior to the day of the flare to achieve a pseudo steady-state. The model is then restarted at 0 UT on the day of the flare and run twice for another 24 hours. One simulation is performed allowing only the solar flux to vary according to the method described above, while holding all other inputs constant, including all high-latitude forcings (the perturbed simulation). Another run is performed where

the solar flux is also held constant (the unperturbed simulation) so that the runs can be compared. The perturbed and unperturbed simulations have exactly the same inputs for the first 90 minutes of the day. After this, the perturbed simulation's EUV flux is allowed to change. These changes are before the flare takes place, so in the results below, the differences between the simulations are non-zero at the start of the flare.

In the simulations, the high-latitudes are driven using the Weimer potential model (*Weimer*, 1995) and the *Fuller-Rowell and Evans* (1987) auroral precipitation model. The inputs are held constant at values that were typical of the day of each of the flares. This means that while there may be significant amounts of energy deposited into the thermosphere via the magnetosphere, this input is constant, implying that any perturbations are a result of the changing solar flux. The high-latitudes may still have an effect on each individual simulation, however, because ion drag and Joule heating are taken into account, but the effects should be the same between the simulations, except for any non-linear coupling between the constant high-latitude forcing and the effects of the solar flare.

3.1.1 Day and night perturbation

Figures 3.2 and 3.3 show difference plots between the perturbed and unperturbed simulations on October 28, 2003 and November 6, 2004, respectively. Here, we define the dayside as being solar zenith angles (SZAs) less than 30°, while the nightside is defined as SZAs larger than 150°. The average dayside and nightside density percent difference, which is calculated by:

$$\rho_{\%diff} = \frac{\rho_{perturbed} - \rho_{unperturbed}}{\rho_{unperturbed}}$$

along with the maximum percent difference in each region, are plotted at 110 and 400 km (400 km only for November 6, 2004). Also shown are the corresponding average vertical velocities at 400 km for October 28, 2003.

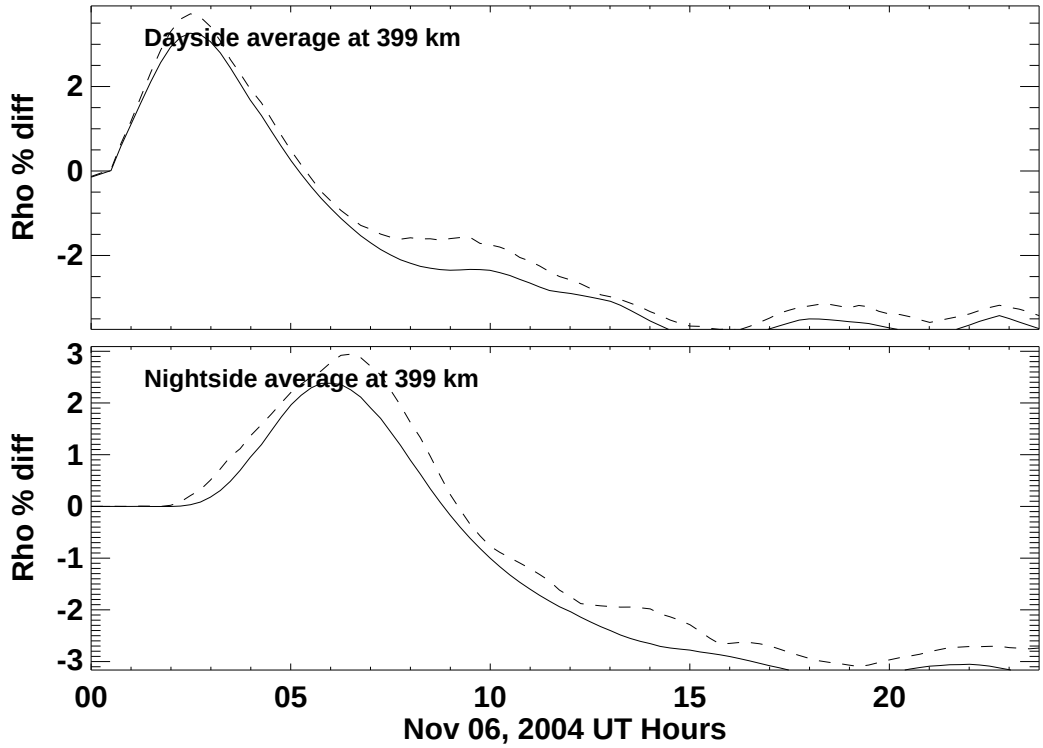

Figure 3.2: Difference plots of the thermospheric density on November 6, 2004. The dayside average (solid lines) and dayside maximum differences (dashed lines) are plotted at 400 km in the top panel and nightside values at the same altitude are shown in the bottom panel. The flare begins at approximately 00:20 UT on the 6^{th}.

The November flare was significantly smaller than the October flare, and therefore the response was considerably weaker. For the November 6 flare, the maximum difference on the dayside at 110 km (not plotted) is less than 0.15% and on the nightside, an order of magnitude weaker. At 400 km, the maximum response is more substantial, 3.7% on the dayside, and 3.0% on the nightside, but still much smaller than the reaction during the October event. Since the trends in the results for both

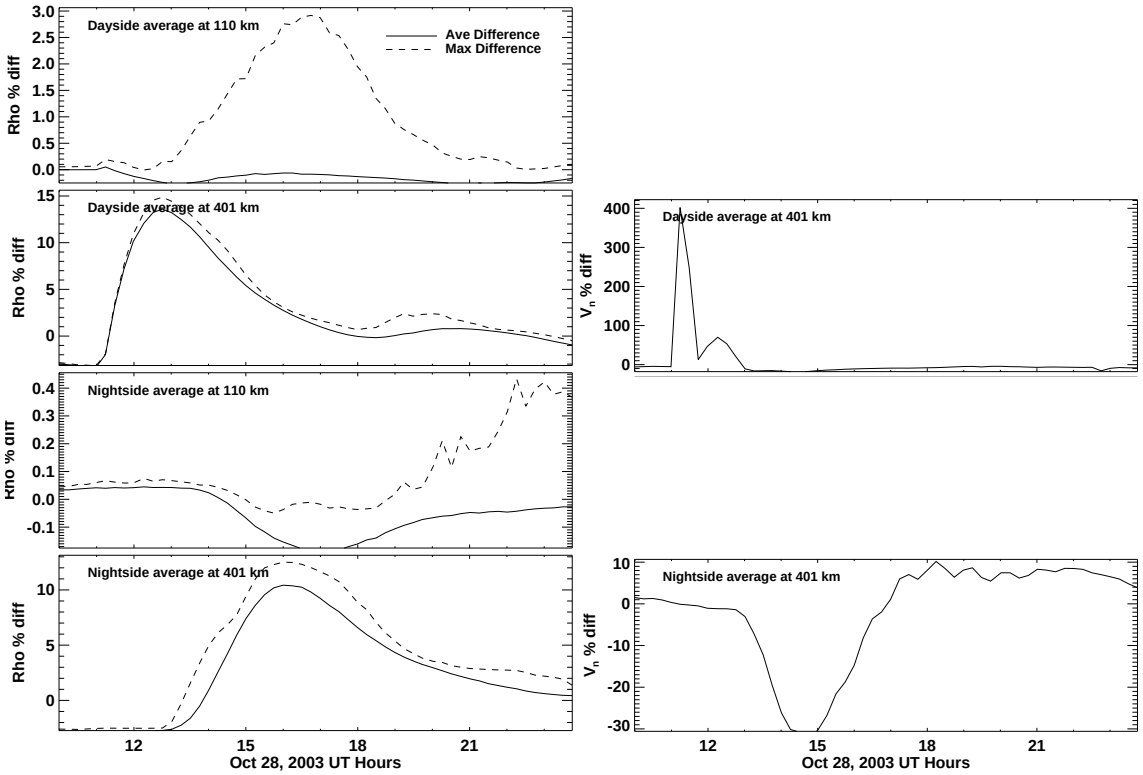

Figure 3.3: Similar to Figure 3.2 except for the October 28, 2003 flare. Density results are also shown at 110 km. Also, the vertical velocity differences are shown on the right, only at 400 km. The flare begins at approximately 11:00 UT on the 28^{th}.

October 28, 2003, and November 4, 2004 are very similar, the focus here will be on the October simulation.

During the October 28, 2003 event (Figure 3.3), on the dayside, the density response at 110 km is again quite small. The largest average density perturbation is less than 0.2%. The maximum difference reaches 2.9%, but it does so several hours after the flare occurs. This perturbation is at the forward edge of a traveling disturbance that propagates towards high-latitudes before diffusing away. The perturbation is extremely localized, only extending 20° in latitude, and it is traveling at an average speed of 310 m/s (± 50 m/s). There is a sharp neutral wind gradient at the leading edge of the disturbance which results in a build up of density. Figure 3.3 indicates

that the density enhancement begins to decrease after 17 UT. This is the case because the wave is moving out of the SZA $< 30^\circ$ region, not because the disturbance itself is becoming weaker. Rather, it continues propagating towards the northern high-latitudes and the density enhancement reaches a maximum of 5.2% at a SZA of 62°, at 19:15 UT, before slowing due to the presence of oppositely directed winds. As the disturbance slows, it quickly diffuses away.

At 400 km, the thermosphere begins to react to the flare within 15 minutes, but the maximum dayside perturbation does not occur until over an hour and a half later. Before the flare occurs, the density difference is actually negative. This is because the EUV flux just prior to the flare used in the perturbed simulation was actually smaller than the constant value used for the unperturbed simulation. At 12:45 UT, the maximum difference between the perturbed and unperturbed runs is 14.9% and the average difference is 13.6%. The thermosphere on the dayside starts to recover, taking approximately 5 hours until the average density at this altitude reaches a local minimum (18:00 UT) before slightly increasing again. There is then a small secondary maximum that occurs at about 20:30 UT at 400 km.

The vertical winds at 400 km are also highly perturbed. The wind percent difference, which is calculated in the same manner as the density percent difference, reaches a maximum increase of 400% (13 m/s) compared to the unperturbed simulation at 11:15 UT. This wind disturbance is not localized, but rather encompasses the entire dayside. As the thermosphere absorbs the excess solar energy, the entire atmosphere expands, and thus the average vertical velocity is highly perturbed. This is a hydrostatic expansion of the atmosphere, synonymous with an increase in the height of pressure levels. By 13:00 UT, the winds have died down, and the perturbation is slightly negative for most of the remainder of the day.

On the nightside, there is no significant response at 110 km, since the propagation of the small disturbance stalls in the high-latitudes, however, there is a substantial

reaction at 400 km. The density enhancement on the nightside at 400 km is nearly as large as that on the dayside. The maximum density difference of 12.5% occurs at 16:15 UT. The maximum average difference reaches 10.4% half an hour earlier. This indicates that there is a traveling disturbance that reaches the nightside thermosphere, and that the nightward propagation is highly efficient. Similarly to the density response at 110 km on the dayside, the largest nightside density perturbation at 400 km does not occur at a SZA $> 150°$. At 16:30 UT, SZA $= 124°$, there is a maximum difference of 13.4%. This maximum occurs as a result of the convergence of wind flows between the equatorial and the high-latitude regions due, in part, to the high-latitude inputs used in the simulation. This means that the location of the maximum is a consequence of this particular time period, and not necessarily indicative of every solar flare event.

The addition of energy to the thermosphere should have an observable effect on the temperature as well as the density. Figure 3.4 shows the temperature perturbations in the same manner as Figure 3.3. At 110 km on the dayside, the maximum temperature perturbation is 3.0%, or 10 K, at 16 UT. This maximum is a result of the traveling disturbance encountering slow winds, as described above, leading to adiabatic heating of the gas, and not due directly to the increase in energy absorption. At 400 km the temperature increases on most of the dayside, resulting in a maximum average perturbation of 3.4% (1257 K for the perturbed simulation vs. 1212 K for the unperturbed simulation). On the nightside, at 400 km, the magnitude of the temperature perturbation is similar to that on the dayside. This is due to adiabatic heating of the gas as the nightward propagating wave converges on itself. The temperature perturbation at 110 km is significantly less.

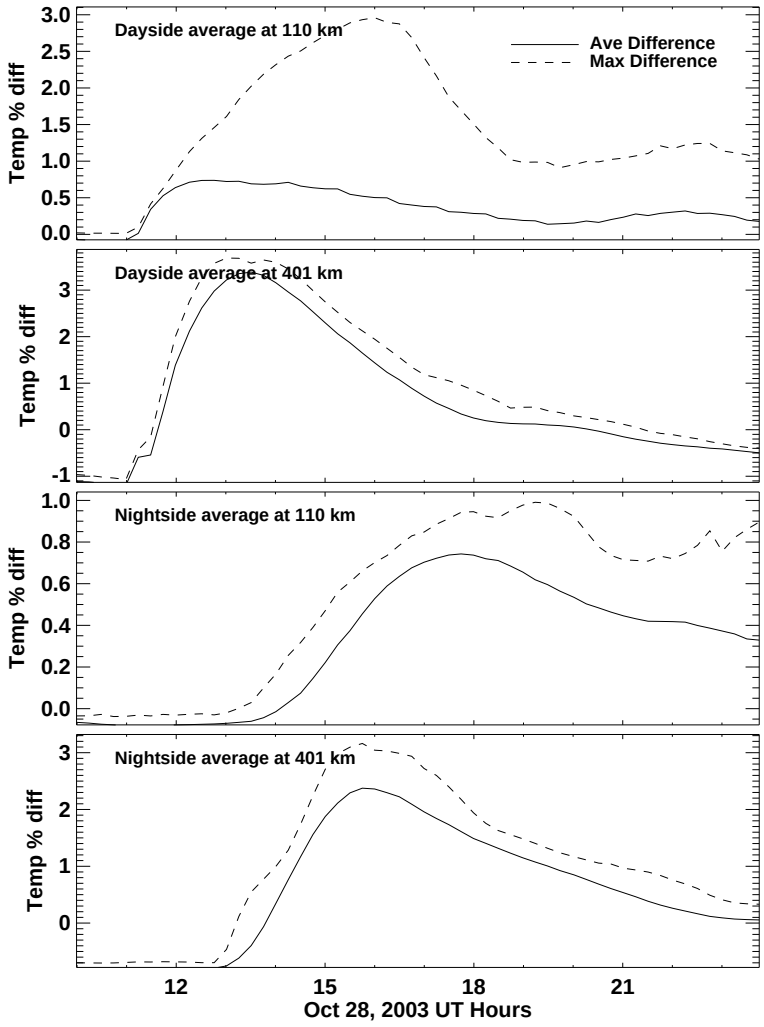

Figure 3.4: Difference plots from GITM simulations of the thermospheric temperature on October 28, 2003. The dayside average (solid lines) and dayside maximum differences (dashed lines) are plotted in the top two panels at 110 km and 400 km respectively. Nightside values at the same altitudes are shown in the bottom two panels.

3.1.2 Wave propagation

Figure 3.5 shows the percent difference of density averaged over 7.5° solar zenith angle bins for 8 different altitudes. At each altitude, solar zenith angle profiles are plotted corresponding to nine different times, separated by 15 minutes, beginning at 11:15 UT and ending at 13:15 UT. In the figure, it is possible to see the propagation of the disturbance from low to high solar zenith angles. Just after the flare occurs (black line), the density has begun to increase at all altitudes. At 110 km, the

density difference is a maximum at this time (as mentioned above, the density percent difference is negative because the unperturbed simulation was run using the first SEE measurement of the day, which is larger than the measurement just before the flare). At higher altitudes, the atmosphere has just begun to change. As time progresses (from purple to red lines), the disturbance extends to higher and higher solar zenith angle. At 400 km, the wave propagates all the way to SZA = 175° by 13:30 UT.

Figure 3.5 indicates that the propagation of the disturbance is very dependent on altitude. At lower altitudes, the thermosphere responds much more directly to the change in the solar flux. Figure 3.3 shows that the response at 110 km, while small, is directly driven by the changing incident energy. This means that the maximum density perturbation is expected to occur very near the time of the maximum incident solar flux, as is the case here. Since the sun shines on the entire dayside, and not only the subsolar location, the flare has a direct effect between 0° and 90° SZA at all altitudes. A consequence of this is that the peak density perturbation immediately after the flare isn't necessarily confined to near the sub-solar point. This is especially the case at intermediate altitudes.

Above about 200 km, the density perturbation reaches midnight, while below 200 km it does not. At 400 km, the wave travels from SZA = 100° to SZA = 165° in about 2 hours. This means that the day to night propagation speed is approximately 1070 m/s (± 150 m/s due to 15 minute temporal resolution of the results and the spatial resolution used in the model). At 400 km, the global mean sound speed is 910 m/s. The average day to night neutral wind speed due to dayside heating is, on average, between 100 and 200 m/s, depending on latitude and solar zenith angle. This indicates that the wave is most likely moving at a velocity that is approximately equal to the bulk wind velocity plus the sound speed.

At 15:45 the wave has propagated completely to the midnight sector. Figure 3.6 shows the same type of plot as Figure 5, but for only 401 km altitude and from 15:45

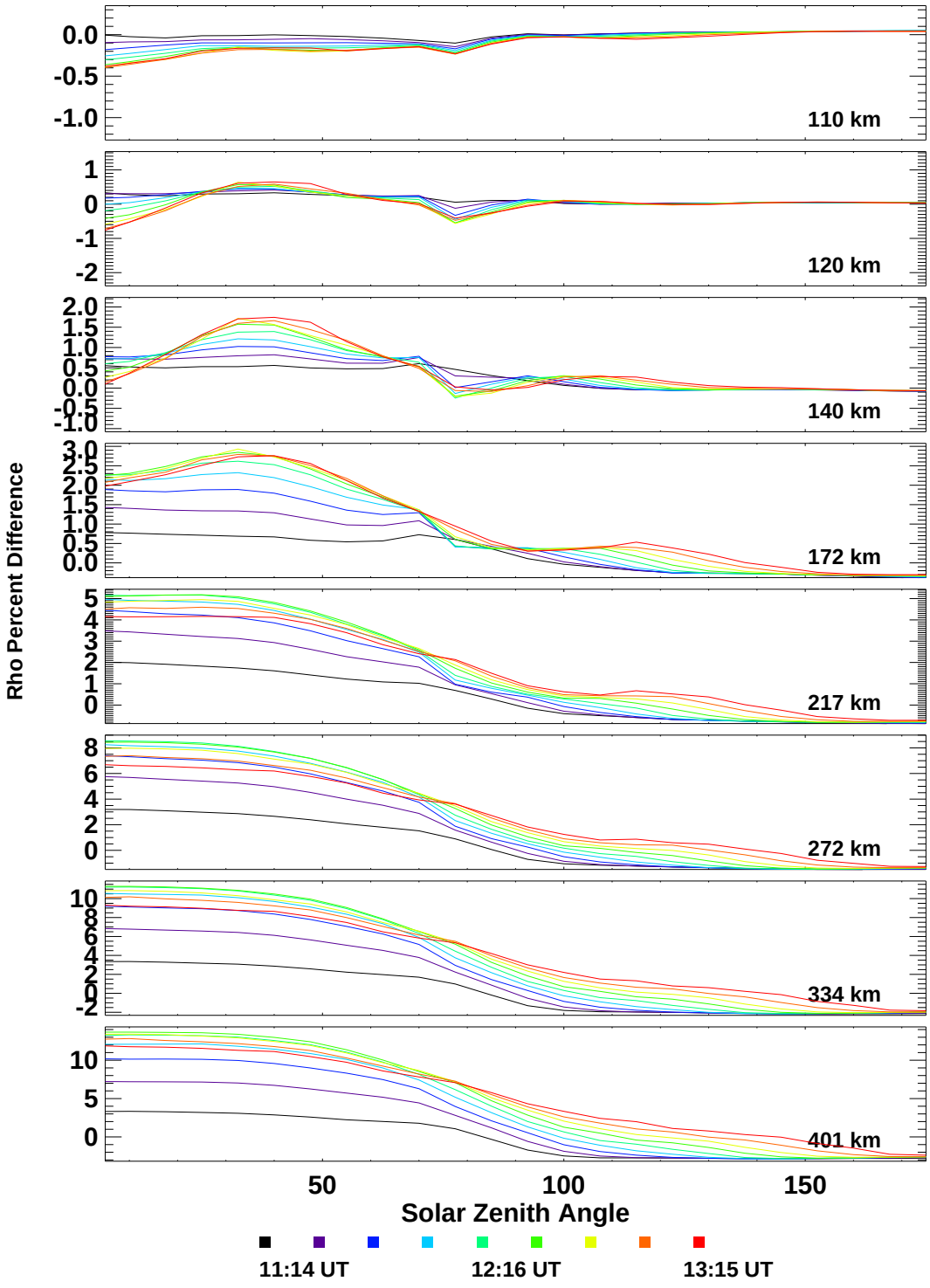

Figure 3.5: Density percent difference vs. solar zenith angle at 8 altitudes. Profiles are plotted at 9 different times separated by 15 minutes, beginning at 11:15 UT.

- 18:45 UT. At 15:45 UT, the perturbation is reflected back towards the dayside. However, the disturbance travels at an average speed of 575 m/s (± 90 m/s), much

slower than it did when moving from day to night. This speed is slightly slower than the bulk wind speed plus the sound speed (i.e. 910 - 200 m/s = 710 m/s), but is relatively close, given the uncertainty, and the fact that the nightside sound speed may be slightly lower than the global sound speed, due to the temperature being lower. As a consequence, the perturbation mostly diffuses away before it returns to the dayside.

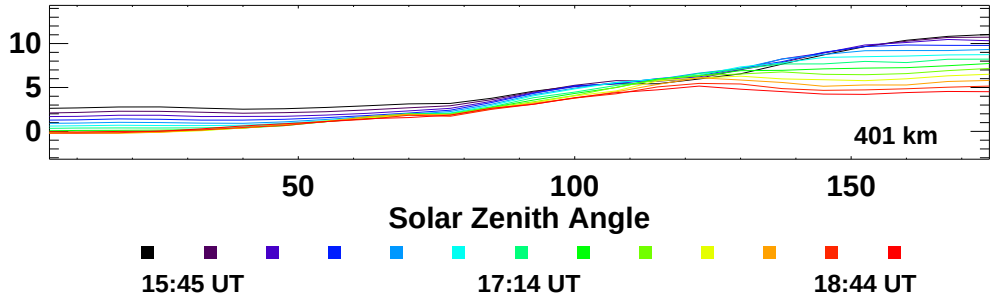

Figure 3.6: Similar to Figure 3.5, beginning at 15:45 UT and ending at 18:45 UT only at 400 km.

3.1.3 Comparison with Champ

The availability of mass density data from the Champ satellite, which is in a polar orbit at approximately 400 km, provides an opportunity for observational support of the features described above. Figure 3.7 shows a direct comparison between the Champ data (top) and GITM results from the perturbed simulation (middle), where the dayside (left) and nightside densities are plotted as a function of latitude and universal time. It is important to point out that no attempt to remove the density fluctuations in the Champ data due to external forcings other than the solar EUV has been made. This means that while the GITM results show only perturbations due to the changing solar flux, the Champ densities are significantly effected by high-latitude dynamics. This issue is demonstrated in the right side of Figure 3.7, where the Champ observations show an equatorward propagating disturbance that is launched from the southern high-latitudes around 7 UT. The GITM results on the other hand, show no

such disturbance. This makes comparison of data and model particularly difficult. Still, it is possible to make quantitative comparisons of several features.

On the dayside, Champ observations indicate two local maxima after the flare begins. While GITM does not capture the second maxima, the first one does show up in the simulation results. At 12:54 UT, GITM reaches a maximum value of 16.39×10^{-12} km/m^3 at 2°S latitude while the Champ observations indicate a local maximum at 12:54 UT and 6°S latitude of 15.38×10^{-12} km/m^3. This means that while the observed peak occurs one GITM cell southward of the simulated one, the time at which it occurs in the model is quite precise. The magnitude of the GITM maximum is larger than that of Champ, however, the increase over the average pre-flare values at the same latitude of the maximum is 45.7% for Champ compared to only 14.1% for GITM.

Although the time at which GITM and Champ reach the local maximum values is the same, the Champ densities begin to increase nearly an hour before the GITM densities. This is due to the conservative approach used to specify the EUV flux within GITM. Prior to the flare, GOES indicates an increase in the soft X-ray flux beginning around 10 UT. A similar increase does not show up in the SEE data because the last measurement prior to the flare was taken at 9:40 UT. In this case, there is some ambiguity as to when the flare actually begins. Here, it is specified to begin when the GOES flux gradient is sharpest, which is after 11 UT, and thus the smaller flux increase that occurs prior to the flare is not captured by the model.

On the nightside, Champ indicates much more structure in the densities than does GITM. As mentioned, there are obvious high-latitude disturbances in the data effecting the mid- and low-latitudes that begin before the flare starts. In addition, the background winds play a significant role in determining the location, time, and magnitude of any nightside perturbations caused by traveling disturbances. For these reasons there is increased uncertainty in making comparisons between observations

and model on the nightside. Regardless, both model and data do show a slight sudden increase in the densities beginning around 14 UT which maximizes in GITM at 16:46 UT. In the Champ data, the density increase is observed as a light blue region between $\pm$ 25° latitude starting between 14-15 UT. In the GITM plot, the background density is much larger, so the response may be harder to see, although there is a general decrease in the density from about 09 UT until the perturbation arrives on the nightside, which the GITM plot shows to occur around 14 UT. This is much easier to see in the bottom plots which show the values at -2° latitude. The model indicates that this increase, averaged over +/-25° latitude for 3 hours is 15.3% compared to 20.5% as observed by Champ. This density enhancement in GITM corresponds to the arrival of the nightward propagating gravity wave in the midnight sector. It is outside the scope of this study to determine the relative importance of nightward propagating gravity waves launched by solar inputs vs. traveling disturbances initiated by high-latitude heating on the enhancement seen by Champ. However, the timing and the magnitude of the disturbance suggests that this feature is at least in part influenced by solar effects on the thermosphere.

3.2 Discussion of the global response to flares

GITM shows that the thermosphere can be highly effected by solar flares on both the dayside and the nightside. While the focus of this study has been on the October 28, 2003 event, the characteristics of the thermospheric response were similar for both the October 28^{th} event and the November 6, 2003 event. At 110 km, the model indicates that the atmospheric mass density at the sub-solar location is not significantly perturbed. This is an expected result. During a solar flare, the shorter EUV wavelengths are enhanced the most. The solar flux at soft X-ray and EUV wavelengths is severely perturbed during strong flares. As a consequence of the exponential decrease of the neutral density with height, the altitude at which most of the photo-absorption

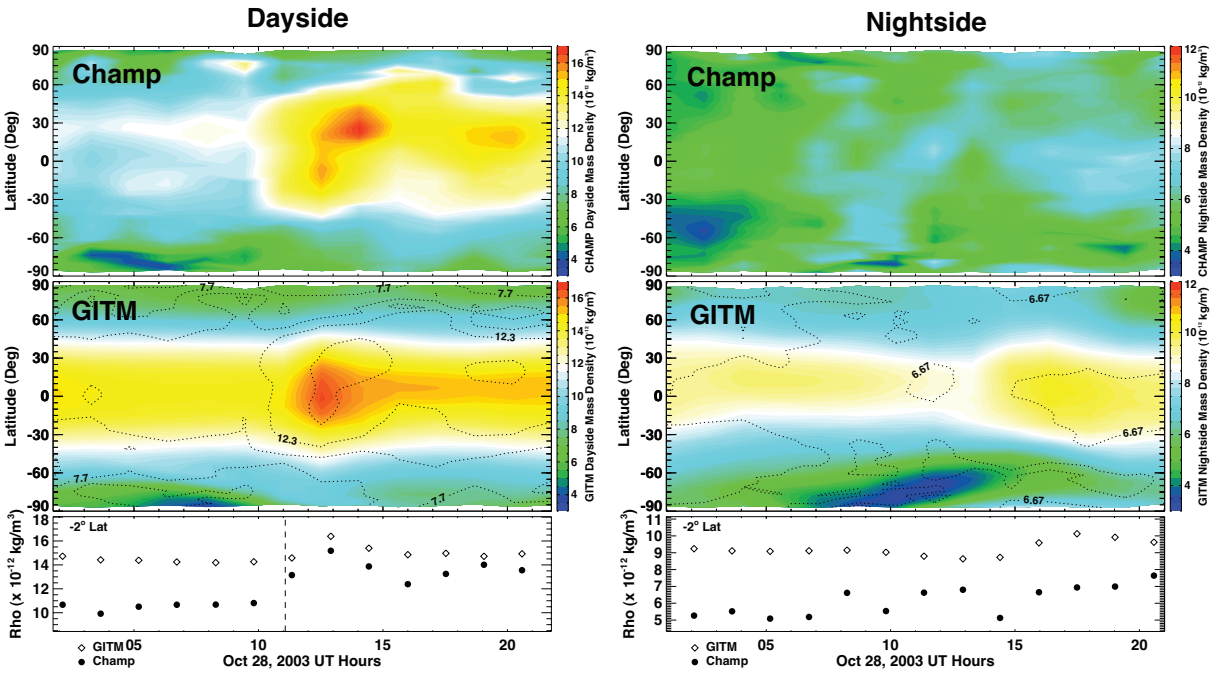

Figure 3.7: Contour plots of neutral density from the Champ satellite (top) and from GITM, extracted at the location of the satellite (middle), as well as a scatter plot of density results at 2°S latitude from both Champ and GITM. The dayside values ($\sim$ 13:20 local time (LT)) are plotted on the left and the nightside values ($\sim$ 1:20 LT) on the right. The dashed lines in the 2D plots are contours of the Champ data plotted on top of the GITM results for comparison. The start time of the flare is indicated by a vertical dashed line.

occurs is where the optical depth:

$$\tau(\lambda, \chi, z) = \sum_i \sigma_i(\lambda) n_i H_i Ch(\chi, z) \tag{3.1}$$

is equal to unity (*Kockarts*, 1981). Here, χ is the solar zenith angle, $\sigma_i(\lambda)$ the absorption cross section at wavelength λ for the species i with density n_i, and scale height H_i at altitude z, and $Ch(\chi, z)$ is the Chapman function. Figure 3.8 shows the altitude at which unit optical depth is reached for wavelengths between 10 and 700 angstroms on October 28, 2003 at 12 local time at the equator, as calculated by GITM. The majority of the energy in this region of the spectrum is absorbed from about 120 to nearly 200 km. The density perturbation at a specific altitude is primarily caused

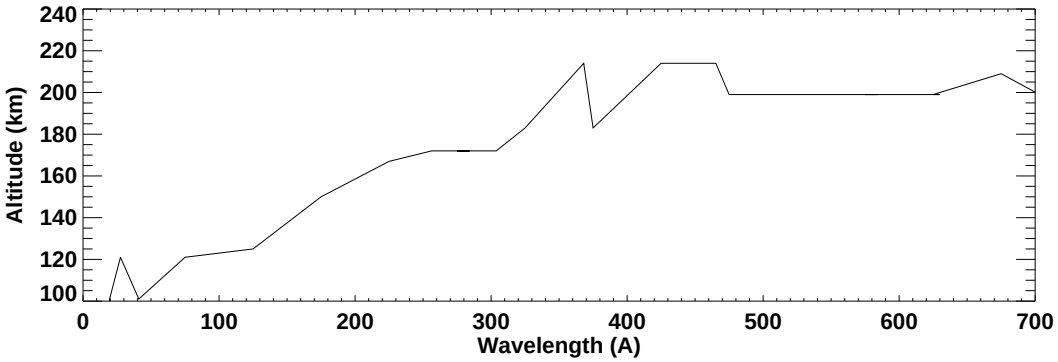

Figure 3.8: Altitude of unit optical depth vs. wavelength for October 28, 2003 at 12 local time at the equator.

by heating below this altitude, so if there is little heating below, the density will not be significantly effected. This means that during a flare, one would not expect a significant density response to occur below 120 km. Near 120 km, where most of the dynamic wavelengths deposit their energy, the thermosphere begins to have a more substantial response. Above 200 km, the atmosphere is so rarefied that efficient absorption of the solar radiation is minimal, and thus the temperature is not directly effected by the flare. However, as energy is absorbed lower in the atmosphere, the entire thermosphere hydrostatically expands, resulting in enhanced upward directed vertical winds (Figure 3.3, right) that bring higher density air up from the lower thermosphere. At 400 km, the integral effect also plays a substantial role on the density perturbation. At higher altitudes, the local density is a function of the density at all lower altitudes. Therefore, if the density is perturbed below 400 km, the density at 400 km will be effected.

In addition to significant density perturbations at 400 km, the thermospheric temperature is also disturbed. Figure 3.9 shows the dayside average temperature difference as a function of altitude at 12 and 13 UT, and indicates that conduction plays a role in heating the thermosphere at higher altitudes. During the flare, the lower thermosphere is heated the most, since the extra energy is mostly absorbed there, as indicated in Figure 3.8. Due to this additional energy, less heat is conducted

down from higher altitudes. Since the density is so much lower higher up, the extra heat has a substantial effect on the temperature. Therefore, dayside heating of the thermosphere above 200 km during a solar flare is primarily due to reduced downward conduction.

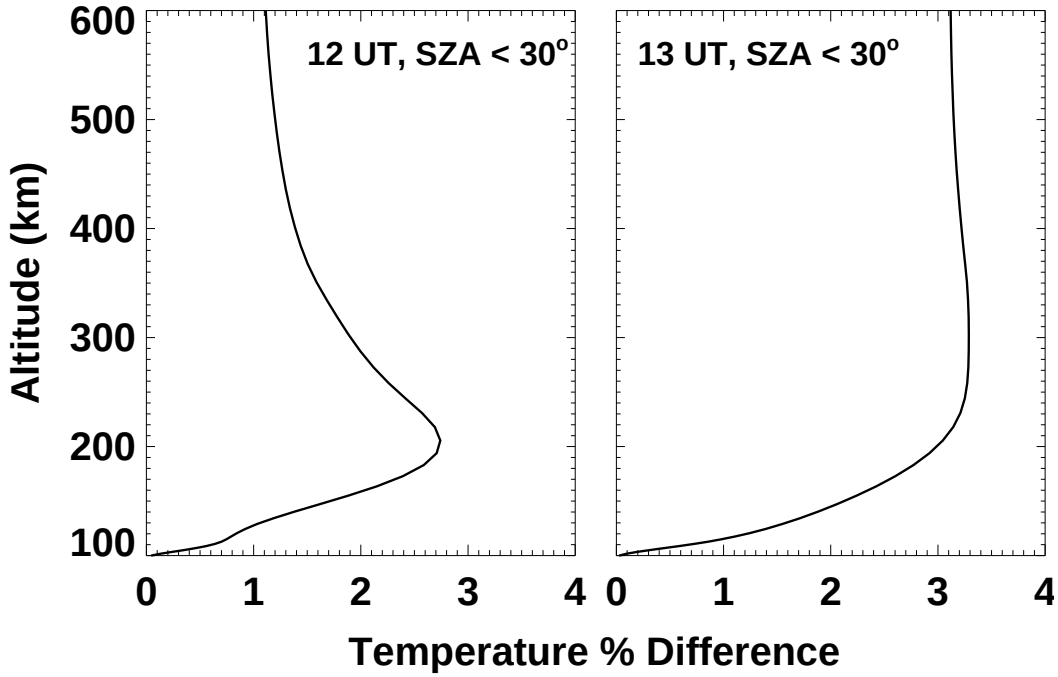

Figure 3.9: Altitude profile of the average dayside (SZA $< 30°$) thermospheric temperature difference between the perturbed and unperturbed simulations at 12 UT (left) and 13 UT (right).

One of the most interesting features of the modeled response is the magnitude of the nightside density perturbation at high altitudes. On the 28^{th}, the maximum nightside response at 400 km is only slightly smaller than the maximum dayside perturbation. This disturbance propagates from the dayside to the nightside at a speed of approximately 1070 m/s, which is close to the local sound speed at 400 km plus the bulk neutral wind velocity. On the nightside, the magnitude of the perturbation is not only a result of upward directed flows. In fact, the vertical flows are enhanced downward until 16 UT, even though the density perturbation is growing during this time. Rather, the density increase is primarily due to the traveling disturbance converging

on itself as it passes through the dawn and dusk sectors and over both poles. This also results in significant adiabatic heating of the gas. Evidence of this is observed in the temperature plots (Figure 3.4), where there is a significant temperature perturbation on the nightside at 400 km that corresponds, very closely, with the density perturbation.

It may be expected that this nightside maximum would occur very close to the anti-sunward point (SZA = 180°), however, as mentioned, the largest perturbation occurs at a SZA of 124°. This is primarily due to the global distribution of neutral winds that act to steer the disturbance. Figure 3.10 shows a time series of the thermospheric density difference at 400 km beginning at 14:00 UT and ending at 20:15 UT with the neutral wind vectors (non-differenced) over-plotted. The plots are spaced in time by 45 minutes. As the wave travels towards the nightside, the strong equatorward directed flows determine the location of the maximum convergence. In this simulation, steady high-latitude inputs were used that were characteristic of those on October 28. These inputs drive ion flows that enhance the neutral winds. This source of momentum along with the Coriolis force serve to make the wave not converge at exactly 180° SZA.

The largest dayside density perturbation at 110 km occurs in the northern high-latitudes, far from the sub-solar point (not plotted). The density perturbation is a result of air from the high density sub-solar region being pulled northward by neutral winds that are significantly enhanced by ion drag. In front of the leading edge of this disturbance, the winds are significantly weaker and eastward, which is perpendicular to the northward directed flow that is carrying the disturbance. This strong wind gradient causes a pile up of neutral gas as the disturbance moves northward. As the wave moves into the mid- and high-latitudes, the density perturbation continues to grow. As the wave passes the terminator, however, it encounters mostly oppositely directed neutral winds. This causes the wave to quickly slow and diffuse away.

Another interesting feature of the results is that there is a significant difference between the day to night propagation speed, and the speed of the disturbance once it is reflected back towards the dayside. The reason for this is demonstrated in Figure 3.10. At all times, the global circulation pattern is dominated by pressure gradients that are set up by solar heating. Prior to 16:30, the time at which the maximum perturbation occurs on the nightside, the disturbance is spreading around the globe such that the direction of propagation is in the direction of the neutral winds, anti-sunward. After 16:30, the wave begins traveling back towards the dayside. When the disturbance is reflected, and starts propagating sunward, the wave encounters oppositely directed winds, which act to slow the propagation. As the disturbance is slowed, it can easily diffuse away, and therefore, is unable to completely propagate back to the dayside. Remnants of the wave show up in the SZA $< 30^{\circ}$ region which causes a small secondary maximum around 20:30 UT. By 23 UT, the largest perturbation in the thermospheric density at 400 km is below 5%.

The results suggest that the day to night propagation speed is approximately equal to the sum of the bulk wind speed and the local sound speed. This is also the case for the reflected wave, however, the high-latitude winds have a more significant influence on the reflected wave than the nightward propagating wave, since the effects of the high-latitude drivers extend deep into the mid-latitude region. This means the bulk velocity, on average, is larger (in the opposite direction) for the reflected wave. Also, the high-latitude wind patterns on the nightside are much less isotropic than the pressure gradient induced winds on the dayside. Therefore, the reflected wave speed is much more dependent on location.

This work shows that the solar flares can have a significant effect on the entire global thermosphere, and not just the dayside. Heating and atmospheric expansion on the dayside can cause disturbances at all altitudes, and can lead to the propagation of a large scale gravity wave that travels near the local sound speed plus the bulk neutral

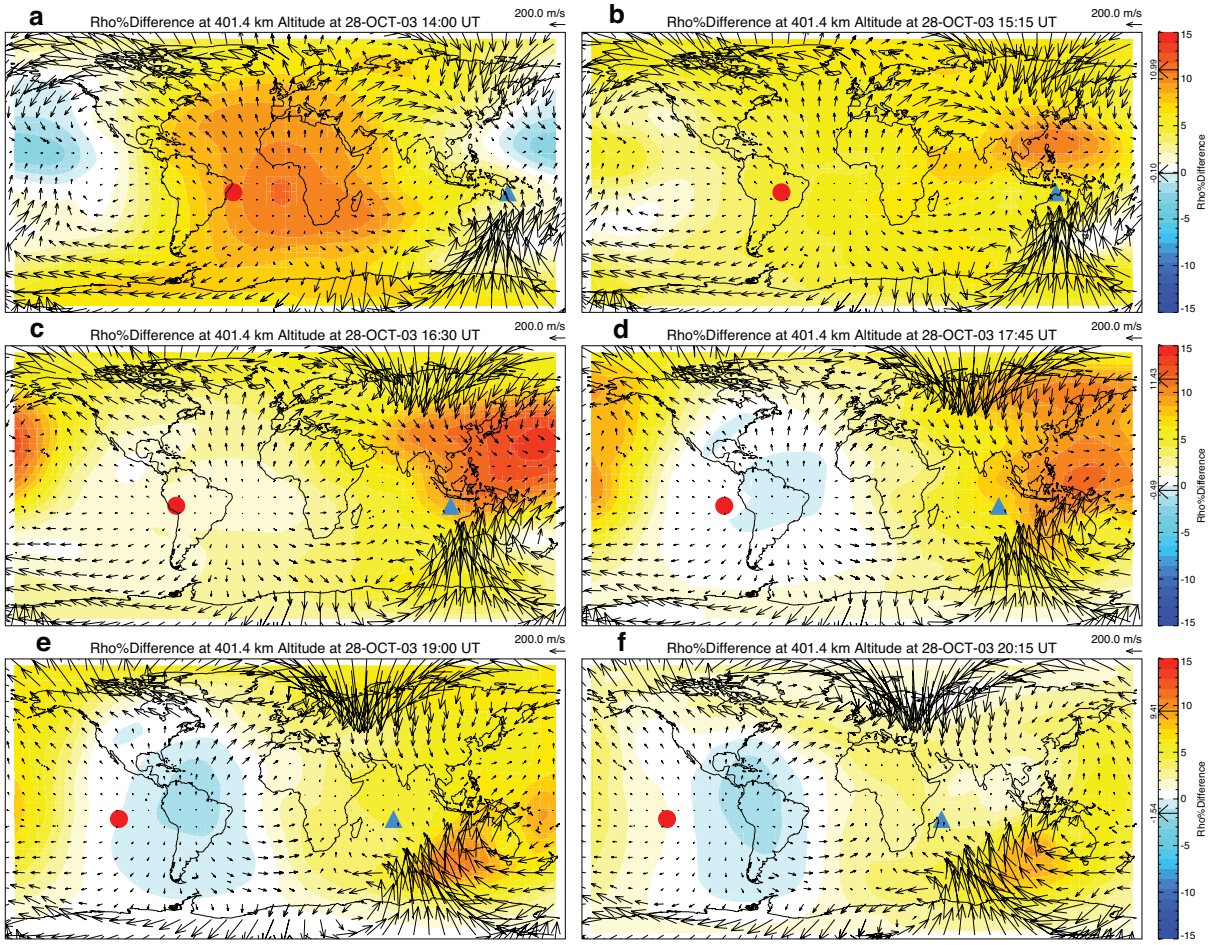

Figure 3.10: Difference contours of thermospheric density at 400 km beginning at 14:00 UT (a) and ending at 20:15 UT (f). The neutral wind vectors from the perturbed simulation are over-plotted. The red circle and the blue triangle indicate the sub-solar point and anti-solar point respectively.

wind velocity and, at higher altitudes, efficiently transports energy to the nightside. The thermosphere may then experience significant nightside density enhancements and be subject to adiabatic heating as the wave converges on itself (4 - 5 hours after the flare). While the trends in the thermospheric response are similar for both events presented in this study, this does not mean that all flare events have the same effect on the thermosphere. In chapter V, a more detailed examination is performed to determine which characteristics of a flare are most important to the response, and how the magnitudes of these characteristics effect the response.

CHAPTER IV

Ionospheric Consequences

4.1 Introduction

The thermosphere is of particular interest to the scientific community not only because of the importance of atmospheric drag, but also because it is highly coupled to the ionosphere. Since the ion density in the upper atmosphere is always small compared to the neutrals, the neutral atmosphere can have a significant effect on the composition and motion of the ionosphere. Changes in the O/N_2 ratio at a given altitude can quickly lead to large changes in the production and loss rates of the important reactions which control the ionosphere, drastically altering its magnitude and composition. Also, horizontal neutral flows, which can be as a large as 1000 m/s or more, can induce significant ion flows in mid- and low-latitude regions. Since the ions are tied strongly to the field lines, they respond by being pushed higher or lower in altitude, which can substantially alter the height and peak density of the F2 layer.

It is these changes in the ionosphere that have become the subject of more intense research in recent years. Advancement of and dependence on space-borne technology in areas such as navigation, communications, and scientific research are driving a need for an understanding of how the thermosphere and ionosphere respond to dynamic inputs to the system. One source of dynamics are sudden changes in the incident solar extreme ultraviolet (EUV) radiation due to solar flares. Several studies have

attempted to characterize the ionospheric effects due to flares (e.g. *Afraimovich et al.*, 2001; *Tsurutani et al.*, 2005; *Le et al.*, 2007). A sudden brightening of the solar flux in the EUV wavelengths causes an increase in the photoelectron production everywhere on the dayside. This can have significant effects on, for example, the propagation of Global Positioning System (GPS) signals, are prone to significant error when there are frequent changes in the total electron content (TEC) between the transmitting spacecraft and the receiver.

A substantial ionospheric response is certainly expected on the dayside during a solar flare, but it is also of interest to investigate how the rest of the ionosphere, including the nightside, may respond to perturbed thermospheric dynamics. It is demonstrated in chapter III that the thermosphere can be perturbed by more than 15% in just over an hour after the Halloween flare occurs. Also, anti-sunward propagating gravity waves can lead to night-side density perturbations that are of the same magnitude as the density enhancements observed on the dayside. In this chapter, GITM is again used to investigate how the ionosphere is affected by these traveling neutral atmospheric disturbances that result from the flare on October 28, 2003.

4.2 Simulation results

4.2.1 Conditions

Unlike the simulations in chapter III, for this investigation, FISM data (Section 1.2.1.1) are used to drive the solar EUV flux in GITM. Since it is of interest to try and capture the exact amount of energy being input into the system, and thus, have the best possibility of obtaining the correct magnitudes of the resulting perturbations. Similar to the previous simulations, GITM is run twice, once using the FISM solar EUV spectrum that included the October 28^{th} flare (the perturbed simulation), and again using a constant spectrum (the unperturbed simulation), where the values were

set to the measured flux at the beginning of the day on the 28^{th}. The high-latitude convection patterns are specified by *Weimer* (1996) using constant solar wind values typical of the time period. The solar wind properties were certainly not constant during the 28^{th}, however, the goal of the study is to evaluate the ionospheric response due only to solar forcing. Therefore, the only external source of dynamics to the model in the perturbed simulation is the changing solar flux, and there are no changing external inputs in the unperturbed simulation.

4.2.2 Ionospheric response

A summary of the ionospheric and neutral response to the flare is shown in the top panel of Figure 4.1, where the minimum, average, and maximum percent differences are shown beginning at 0 UT on the 28^{th} until 4 UT on the 29^{th}. In addition, the details of the ionospheric response are shown in Figure 4.2, where contour plots of the vertical TEC percent difference along with the horizontal ion velocity difference vectors (calculated at the H_mF_2 altitude) are plotted every hour beginning at 13 UT and ending at 22 UT. In both cases, the differences are calculated by the equation:

$$\frac{TEC_{perturbed} - TEC_{unperturbed}}{TEC_{unperturbed}} \times 100,$$

The minimum (maximum) percent difference at any one time is simply the smallest or most negative (largest) difference between the two runs at one cell location, while the average difference is a surface area weighted global mean. The vertical grey line indicates the start time of the flare.

When the flare goes off, there is a clear increase in the globally averaged TEC, which maximizes at about 20%. This is the result of increased photoelectron production on the entire dayside due to the increased EUV flux. Since the average calculation is global, and therefore takes into account the nightside as well as the dayside, this

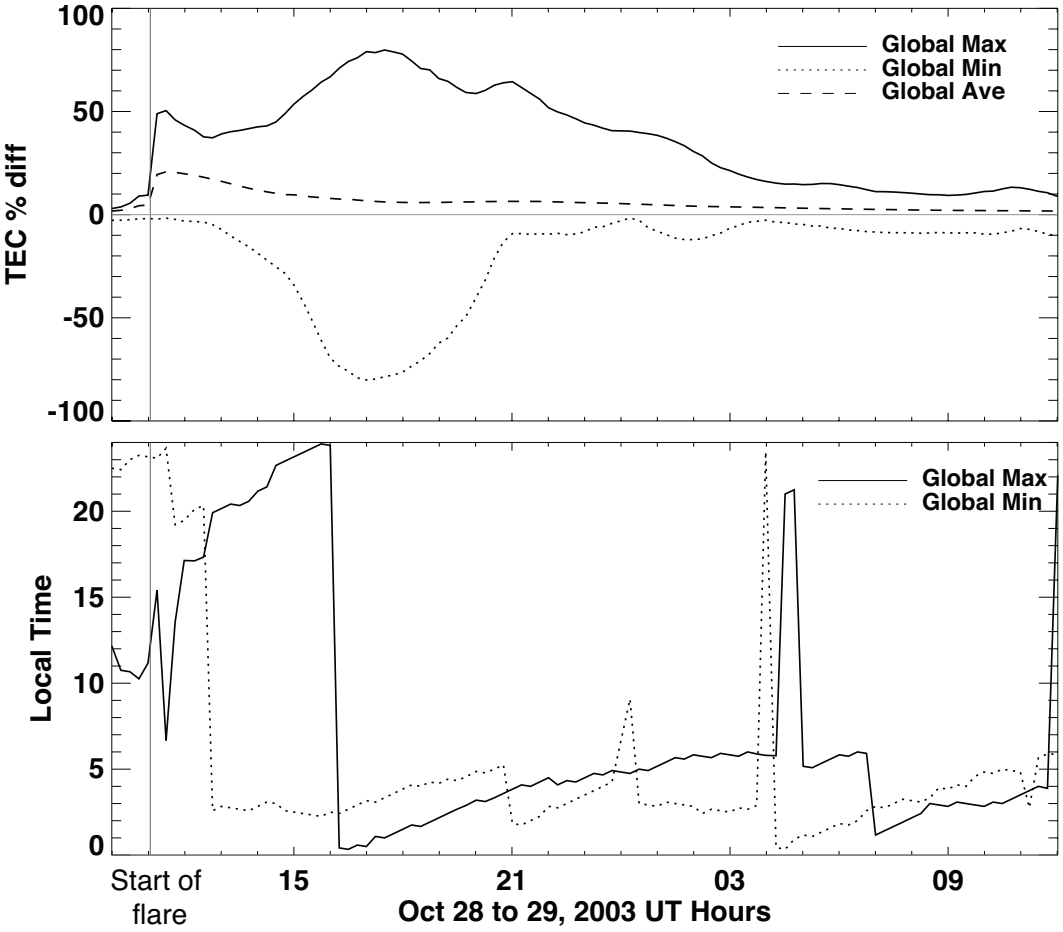

Figure 4.1: (Top) TEC percent difference beginning at 10 UT on October 28, 2003 and ending at 12 UT on the 29^{th}. The solid, dotted, and dashed lines indicate the global maximum, minimum, and average difference between the perturbed and unperturbed runs. The start time of the flare is indicated by the solid grey line just after 11 UT. (Bottom) The local time at which the maximum (solid line) and minimum (dotted line) occurs as a function of UT.

percent difference is lower than it would be if only the dayside average was calculated ($\sim$40%). By 16 UT, this dayside perturbation has subsided (Figure 4.2), and while the global average difference is still decreasing after 0 UT on the 29^{th}, the difference is minimal.

In addition to the dayside response, there are significant positive and negative perturbations that occur long after the start of the flare. The bottom panel of Figure 4.1 shows the local time at which the maximum and minimum perturbations occur. After the flare starts, at 11 UT, the maximum global perturbation is located close to

noon. As time elapses, the largest global perturbation propagates towards the nightside at an increasingly slower rate. Conversely, the minimum perturbation remains on the nightside throughout the majority of the time period. These maxima and minima are very localized features that reach their largest magnitudes nearly 6 hours after the start of the flare. A more detailed description of the development of these features is shown in Figure 4.2, which further demonstrates that these enhancements and depletions occur in the nightside ionosphere (i.e., near the blue diamond, which indicates 180° solar zenith angle (SZA)). The largest TEC enhancement develops over the western coast of Australia beginning at 15 UT. By 17 UT, the perturbed simulation reaches a value of 5.9 TECU (where a TECU is 10^{16} electrons m^{-2}) vs. an unperturbed value of 3.3 TECU (79.0% difference). At the same time, a strong TEC depletion develops over the western pacific and moves over the east coast of Australia where the perturbed TEC value reaches .56 TECU vs. an unperturbed value is 5.6 TECU (-80.1% difference).

During this time period, the locations of the perturbations in the TEC are correlated to the perturbations in N_mF_2. Therefore, in order to determine the cause of these ionospheric disturbances, it is useful to consider the dynamics taking place in the F region, as that is where much of the TEC is located.

Since the large changes in the electron density occur on the nightside, local production of electrons is not likely to be the cause of the positive perturbation, especially given that the high-latitude drivers used during the perturbed and unperturbed simulations are identical. Instead, GITM results suggest that these features are a ramification of coupling with the neutral atmosphere. Chapter III shows that during large flares, gravity waves may be launched in the thermosphere that propagate nightward at the local sound speed plus the background wind velocity. While enhanced neutral zonal winds do not have a strong effect on the transport of the charged species because the ions are restricted to motion along the field lines, enhanced neutral meridional

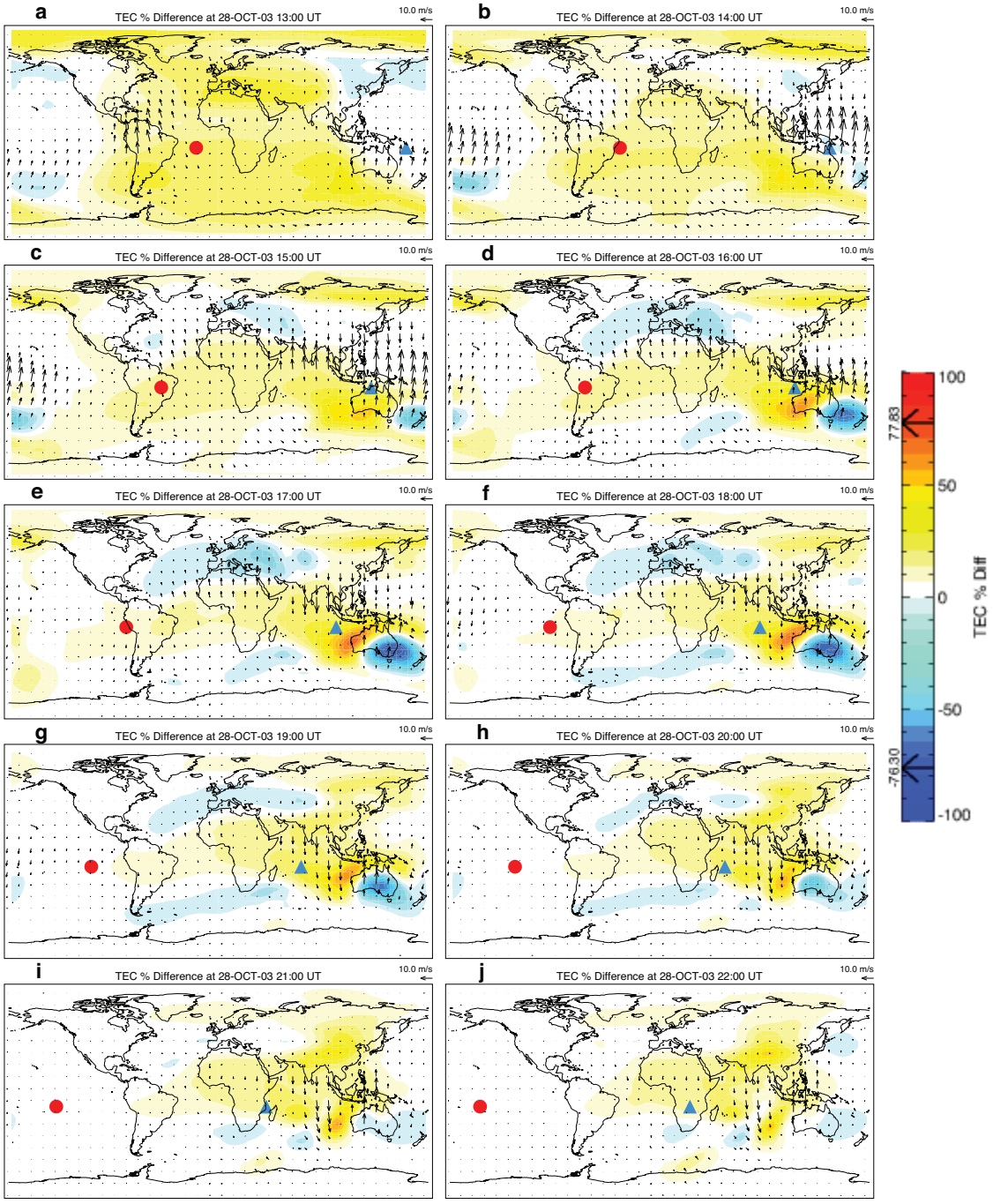

Figure 4.2: TEC percent difference at 10 different times on October 28, 2003 beginning at 13 UT (a) and ending at 22 UT (j). The vectors show the ion velocity difference between the perturbed and unperturbed runs. Local noon and midnight are indicated by the red circle and blue triangle respectively.

winds can result in a larger meridional ion velocity. In this case, beginning at 13 UT, perturbed neutral winds lead to enhanced ion flows in the south pole region (Figure 4.2, panels a, b, and c). The ion flows are enhanced enough to cause a larger tongue of ionization over the south pole in the perturbed simulation, increasing the electron concentration on the nightside. While the ion velocity is relatively unchanged just south of Australia, the stronger ionization tongue is supplying the region with more electrons for the nominal meridional wind, which is setup by the day-to-night pressure gradient as well as the high-latitude convection pattern, to push equatorward. This is shown in Figure 4.3, in which the electron density at 15 UT (the time at which the nightside positive perturbation is beginning to grow) is plotted at 401 km, which corresponds to the H_mF_2 in the region south of Australia during this time period. Both the perturbed and the unperturbed simulations are shown. Figure 4.3 shows that the N_mF_2 south of Australia in the perturbed simulation is approximately 2.4e11 $1/m^3$ whereas the unperturbed N_mF_2 is 1.7e11 $1/m^3$ a difference of 41%. It is important to note that while the absolute difference between the perturbed and unperturbed N_mF_2 in the low-latitudes is larger than that south of Australia (approximately 3.8e-11 $1/m^3$), the percent difference is much smaller (14%). After 17 UT, the meridional wind perturbation over the west coast becomes negative as the thermospheric wave reflects back towards the dayside. These enhanced southward winds push the ionosphere down field lines, where the recombination rates are larger due to higher N_2 densities, and the enhancement slowly dies away.

GITM results suggest that the mechanism behind the large negative electron density perturbation that forms over the east Australian coast is also related to dynamics in the ion velocity. The depletion develops at the location where there are enhanced northward ion winds (Figure 4.2). While this occurs in the near-midnight sector, the location of the perturbation is more than 1 hour behind midnight, and therefore the tongue of ionization does not effect the electron density in this region. Without

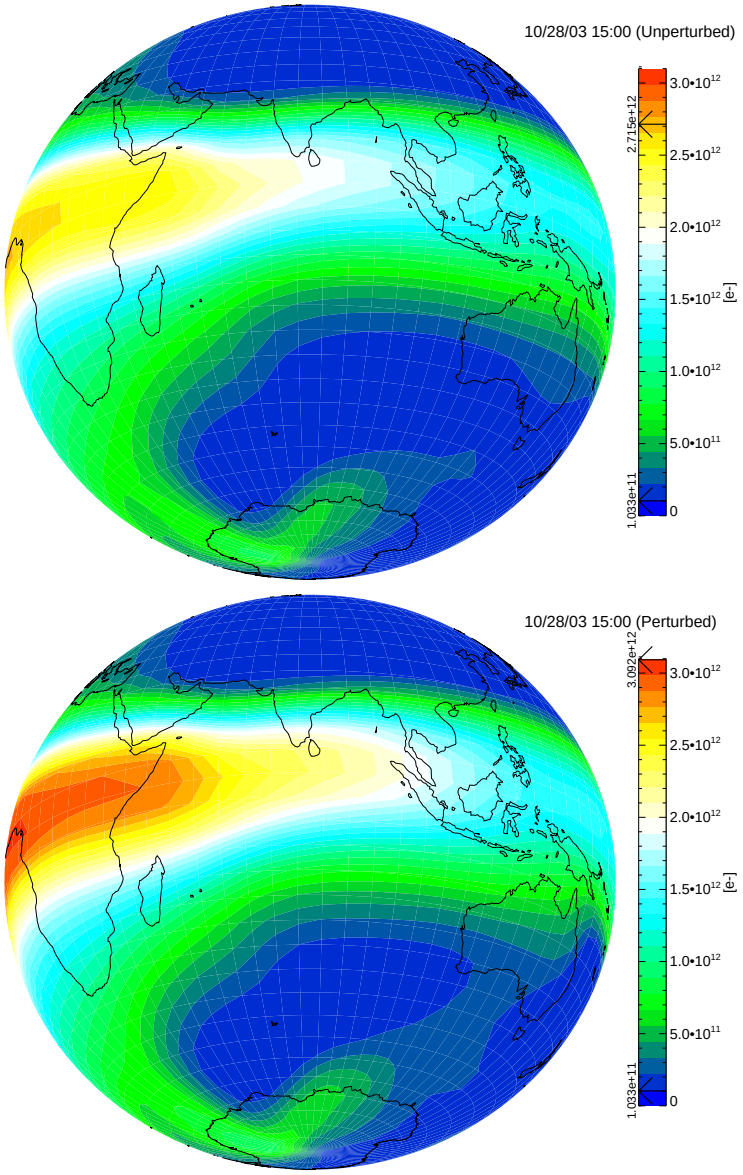

Figure 4.3: Electron density (m^{-3}) at 15:00 at 401 km for the unperturbed (top) and perturbed simulations (bottom).

the addition of electrons through the tongue of ionization, the enhanced northward meridional winds push the ionosphere upwards in altitude, along field lines. Figure 4.4 shows the electron density altitude profile for the perturbed simulation (solid lines) and the unperturbed simulation (dashed lines) beginning at 14 UT and ending at 17 UT. In both simulations, the altitude of the peak density is around 350 km at 14 UT (purple lines). By 15 UT (blue lines), the H_mF_2 has moved upwards, and the density

at the top of the model is significantly larger than earlier. As time progresses (green and orange lines), the peak density occurs at the top of the model, and the magnitude becomes smaller. This means that there are significant vertical ion flows at all altitudes pushing the electrons out of the model domain. In both simulations, the day-to-night pressure gradient in the thermosphere drives northward neutral winds at this location that result in a nominal upward motion of the ionosphere. However, Figure 4.4 indicates that the electrons are pushed out of the top boundary faster in the perturbed simulation than in the unperturbed simulation. This is due to the larger northward neutral velocity in the perturbed simulation dragging the ions more quickly up the field lines.

While the upward movement of the ionosphere clearly has an effect on the electron density at a given altitude, the TEC along a field line is not likely to be largely effected because the electrons are only moving to a higher altitude along the same field line. The model indicates a TEC depletion at this time only because the ionosphere has been pushed above the top of the model. In fact, since the ionosphere is being pushed up, slower recombination may actually result in an overall larger TEC magnitude. However, the model results shed light into the importance of neutral coupling on the ionosphere, especially during dynamic time periods. The results indicate that the ability of the enhanced horizontal neutral flows, which develop as a result of a solar flare that began several hours ago on the opposite side of the planet, to lead to significant vertical motion of the ions is important for determining the altitude of the F2 peak, as well as the rest of altitude profile of the ionosphere.

4.3 Discussion of ionospheric consequences

It is expected that the ionosphere should respond significantly to a solar flare. On the dayside, high EUV fluxes result in higher photoelectron production, and ultimately, a widespread increase in vertical TEC measurements. However, GITM indi-

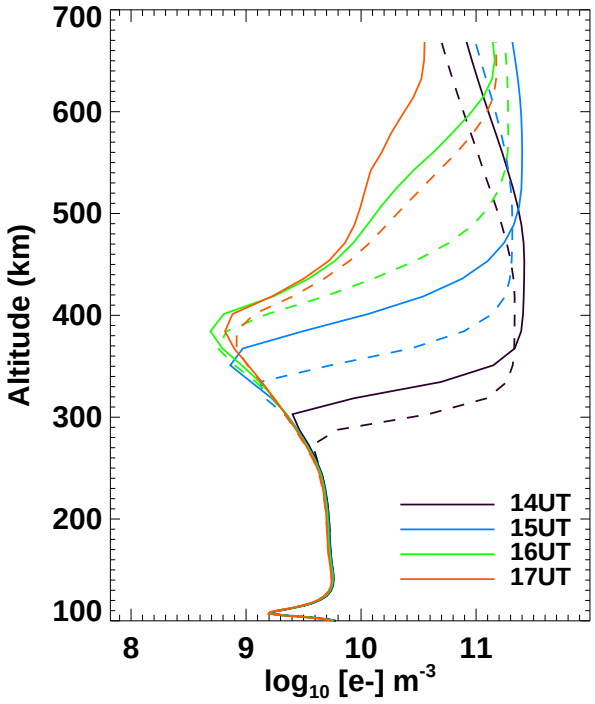

Figure 4.4: Electron density vs. altitude beginning at 14 UT and ending at 17 UT for the unperturbed (dashed lines) and perturbed simulations (solid lines) over the east coast of Australia (152.5 E longitude and 32.5 S latitude).

cates that perturbations in TEC can be more substantial elsewhere in the ionosphere, and that these perturbations can begin many hours after the onset of the solar flare. Traveling thermospheric disturbances, which propagate to the nightside and converge on themselves near midnight, cause substantial compositional and dynamical neutral perturbations. As a result of the changes in the thermosphere, the electron density, and therefore TEC, can be both depleted and enhanced in localized regions on the nightside for more than 15 hours after the flare.

The most significant ionospheric perturbations occur in the southern hemisphere around midnight. The largest TEC enhancement, which begins around 15 UT, is due to an enhanced tongue of ionization in the summer hemisphere. It is expected that a similar feature would develop in the northern summer under similar forcing, since, after the flare, the neutral winds are more disturbed in the summer pole than in the winter pole. The location of the depletion that results from the lifting of the of the

ionosphere depends on several factors which determine that ability of the neutrals to force the ions, such as where the neutral winds are enhanced as well as the neutral density, and also, the ability of the ions to move vertically (therefore, the inclination of the magnetic field at that location). In this case, the enhanced ion velocities occur where the neutral density and neutral winds are also perturbed, which corresponds to the region of neutral wind convergence on the nightside. Therefore, there is no reason to expect that this feature is limited to the southern hemisphere, but rather, is dependent on the relationship between the location of neutral convergence, the respective density enhancement in that location, and how close that location is to the magnetic equator.

As mentioned, GITM does not include self-consistent low-latitude electrodynamics. The addition of such physics to the model will clearly have an effect on the overall structure of the ionosphere, especially at mid- and low- latitudes. Most likely, inclusion of low-latitude electrodynamics would have a significant effect on the location of the perturbations indicated in the results. This is because the location of the perturbations is dependent on where the north-ward electron density gradient becomes positive on the nightside. In this study, the perturbations that result from the solar dynamics are of interest. The model results indicate that the largest localized perturbations occur on the night-side near Australia. This is far enough south of the magnetic equator such that the addition of low-latitude electrodynamics should have little effect on the magnitude and location of these perturbations. However, given a situation where the convergence of neutral flows on the nightside occurs closer to the magnetic equator, low-latitude electrodynamics are expected to play a more significant role.

These features all have important operational implications due to their localized nature and severity. The perturbations observed in the model are all highly dependent on both the neutral wind and ion convection patterns and therefore on the current

geomagnetic conditions. The ability to predict such features, then, is an extremely difficult task, since it is important to correctly specify the advection of both the ion and neutral species as well as correctly specify the external drivers acting on the system. While global models are well suited for this purpose, more work must be done to further understand the important physics taking place. It is important to continue to validate models against in-situ data taken in both the thermosphere and ionosphere so that further understanding about the global nature of the response of both the neutral and ionized atmosphere to solar flare events can be developed.

CHAPTER V

Characteristics of a Flare and Their Effects

5.1 Introduction

The previous chapters focused on examining how the atmosphere responds to real flare events. While these investigations have helped shed light on the magnitude of the perturbations associated with an increase of the solar radiation on a global scale, this chapter is meant to supplement the previous work with more detailed investigation into quantifying how each of the individual aspects of a flare affect the response. This is accomplished through the use of idealized simulations, in which synthetic solar flux data is used to drive GITM. Ultimately, the goal of this particular study is to examine the way in which the different characteristics of a flare affect the thermospheric density at 400 km.

5.2 Solar inputs

The flare characteristics examined in this study are the (a) total integrated energy, the (b) peak flare magnitude, the (c) background flux magnitude, the (d) elapsed time between the pre-flare background flux and the peak flux (rise time), and the (e) elapsed time between the peak flux and the post-flare background flux (decay time). The reason for the use of synthetic data is that it is not possible to drive the model

using actual solar flux measurements and separate out the effects due to the above mentioned quantities. Artificial data, on the other hand, can be used to drive the model under different solar flares that share some of the same characteristics. For example, since it is of interest to examine the relationship between the total amount of energy incident on the thermosphere during a flare and the response, it would be useful to have data during several solar flares, where each have the same background and peak flux, as well as the same elapsed time between the background flux and the peak flux, while the total energy incident (and thus decay time) during each flare is different. It is not possible to do such a study using real flare events, where, for even two flares, none of the characteristics are likely to be constant, let alone during 4 or 5 flares. But by using synthetic data, such experiments are possible.

The synthetic data used in this study are not completely fabricated. For each of the flares mentioned in this chapter, the input fluxes are based on data from the Halloween flare. Specifically, the pre-flare flux, maximum flux, and total integrated energy are used as starting points from which to create a solar flare spectral profile, and then, depending on the characteristic of interest, the flare profile is tweaked accordingly. This is done several times for each characteristic, and GITM is run using the corresponding solar flux data. All other inputs are held constant between the runs, therefore, any difference in the results between each simulation is due only to use of a different solar driver. In each case, GITM has been run for 24 hours prior to the solar flare in order to achieve a pseudo-steady state. In addition, for normalized comparison purposes, a baseline simulation has been performed in each case, in which the solar flux is held constant throughout the duration of the event.

5.3 Results

5.3.1 Total integrated energy

Intuitively, one of the most important characteristics of a solar flare, with regard to the thermospheric response, is the total integrated energy incident into the atmosphere above the background energy level. After all, it is this energy that causes the high thermospheric temperatures, forms the ionosphere, and sets up the global circulation patterns in the first place. The total integrated energy above the background is the total energy incident into the atmosphere summed over all wavelengths, above the background, integrated over the duration of the solar flare. In order to examine the effect the total integrated energy has on the density response, four flare simulations are performed using GITM. Each of the flares inputs a different amount of energy into the system. This is accomplished by holding the flare magnitude and peak time constant, while allowing the decay time to vary. The temporal profile of the solar flux for .1–.8 nm is shown in the top panel of Figure 5.1. The flares are labeled by the numbers 0.33, 0.67, 1.0, and 1.33, which are based on the relative amount of integrated energy each of them inputs into the atmosphere. For example, the 1.33 flare inputs 1.33 times as much energy as the 1.0 flare, the 0.67 flare inputs 0.67 times as much energy as the 1.0 flare, etc. For reference, the peak time, peak magnitude, and total integrated energy values for the 1.0 flare are similar to those for the actual Halloween flare.

The bottom 3 panels of Figure 5.1 show the global average, global maximum, and global minimum neutral density response respectively for 24 hours following the onset of the solar flare. The density percent difference for each case is calculated by the equation

$$\rho_{\%diff} = \frac{\rho_{flare} - \rho_{baseline}}{\rho_{baseline}} x100.$$

The minimum (maximum) values are taken at the horizontal grid cell that contains

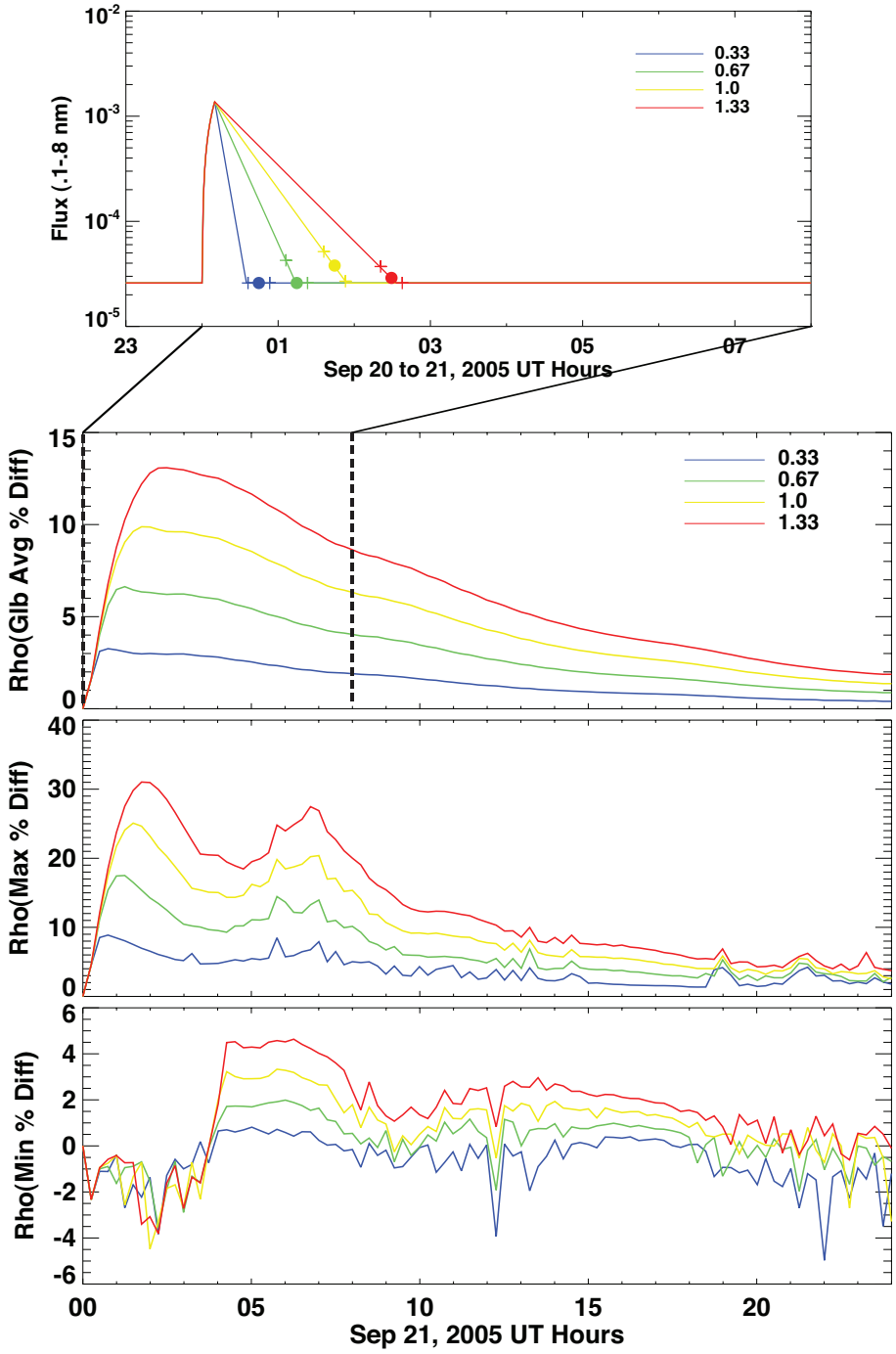

Figure 5.1: (Top) Log_{10} solar flux from .1 - .8 nm for the 4 solar flares used to drive GITM. Each color represents a flare with a different total integrated energy, normalized to 1. The background and peak fluxes are constant between all flares, as is the time duration between the background and peak flux. The filled circles indicate the time at which the maximum density perturbation occurs. Also shown are the global averaged (2^{nd} from top), global maximum (2^{nd} from bottom) and global minimum (bottom) mass density perturbations resulting from each flare.

the smallest (largest) difference over the entire globe, at 400 km.

Qualitatively, the global average response behaves in an intuitive manner. The flare with the most incident energy causes the largest density response. In addition, larger the flare, the longer the duration of atmospheric perturbation. However, it is difficult to say whether the duration of the response is more dependent on the amount of energy being input or on the length of the flare itself, since this is not constant from simulation to simulation. This will be addressed further at a later point in the chapter.

In terms of the maximum global average for each of the 4 cases, the perturbations are 3.25%, 6.63%, 9.88%, and 13.08%, respectively. This means that the maximum global average density perturbation due to the 0.33 flare is 1/3 times the density perturbation due to the 1.0 flare, the perturbation due to the 0.67 flare is 2/3 times the perturbation due to the 1.0 flare, and the perturbation due to the 1.33 flare is 1.32 times the density perturbation due to the 1.0 flare, suggesting that the global average density response is quite linearly related to the additional energy being input to the system.

The global maximum perturbations behave in a similar manner. The largest perturbations that occur throughout the day due to the 0.33, 0.67, and 1.33 flares are 0.35, 0.70, and 1.32 times the perturbation due to the 1.0 flare respectively. This also suggests that the global maximum perturbation is linearly related to the additional energy being input. In addition to the primary maxima in the global maximum results, there are secondary maxima that occur 6–7 hours after the start of each flare. These maxima are a result of a traveling atmospheric disturbance converging on itself on the night-side. While the night-side density enhancement itself correlates with the amount of extra energy being input into the system, the ratio of the maximum night-side perturbation to the maximum dayside perturbation is higher for the weaker flares (0.95,0.83,0.79, and 0.88 for the 0.33, 0.67, 1.0, and 1.33 flares respectively).

The minimum percent difference plot gives an indication of the time at which the traveling atmospheric disturbance has affected every part of the globe. As discussed in Chapter III, the speed of propagation of this disturbance is roughly equal to the local sound speed plus the background velocity. Therefore, the total integrated energy is not expected to have an effect on this time, which is supported by the bottom panel of Figure 5.1, since the time at which the global minimum perturbation becomes larger than zero is the same for each of the flares. Beyond that, the global minimum figure gives an indication of how much the entire globe is affected by the flares in much the same way that the global average figure does: Larger flares result in a larger density perturbation, everywhere.

The one remaining piece of information that can be obtained by these plots has to do with the timing of the global density response. While the rate of increase of the global average density enhancement is constant for each of the flares, the time at which the peak enhancement occurs is not. In the top panel of Figure 5.1, each of the flux profiles has a corresponding filled circle. These circles indicate the time at which the peak global average density enhancement occurs for each of the flares. In all of the cases, the peak enhancement occurs very near the time at which the flare ends. This indicates that the most important factor in determining the time of the maximum global density response is the decay time of the flare.

5.3.2 Different peak magnitude

High background flux

Next, several GITM simulations are performed in order to quantify the effect of the peak flare magnitude has on the global response to a flare. In this case, GITM is run using five different solar flares, each having a different peak EUV flux value, but the same total energy integrated over the life of the flare. The temporal profiles of each

of these flares is shown in the top panel of Figure 5.2. The relative magnitudes of each of the flares are normalized to 1, thus the 0.25 flare has a peak flux magnitude of 0.25 times that of the 1.0 flare, etc. As is the case in section 5.3.1, the 1.0 flare uses similar background flux, peak flux, and total incident energy values as the Halloween flare. In each of the 5 cases, the background flux as well as the elapsed time between the background flux and the peak flux are identical. In addition, the total integrated energy above the background incident into the thermosphere throughout the flare is constant.

The top panel of Figure 5.2 further reinforces the above conclusion that the timing of the peak global perturbation is determined by the decay time of the flare. These 5 flares span a greater amount of time than those in section 5.3.1, yet, as indicated by the filled circles, the maximum perturbation always occurs near the time when the flare ends.

The other panels in Figure 5.2 show a more detailed description of the thermospheric response to the 5 different flares. The global average (2^{nd} from top), global maximum (3^{rd} from top), and global minimum (bottom) are all plotted as a function of time for the 24 hour period following the beginning of the flare. One of the most interesting features in the density response to the 5 flares is that while the peak of the global average perturbation decreases with the relative magnitude of the flare, the dependence is not very strong. The peak global perturbations are 8.1%, 9.3%, 9.9%, 10.2%, and 10.2% for the 5 flares, from lowest to highest peak flux. This range of density enhancements is very small compared to the range of enhancements when calculated on a cell-by-cell basis (global maximum plot), which are 14.0%, 19.7%, 25.1%, 27.7%, 28.1% respectively.

In the maximum difference plot, two maxima occur during the day, one prior to 5:00 UT for each of the flares and another between 5:00 and 10:00 UT. These maxima correspond to the night-side response to a traveling atmospheric disturbance

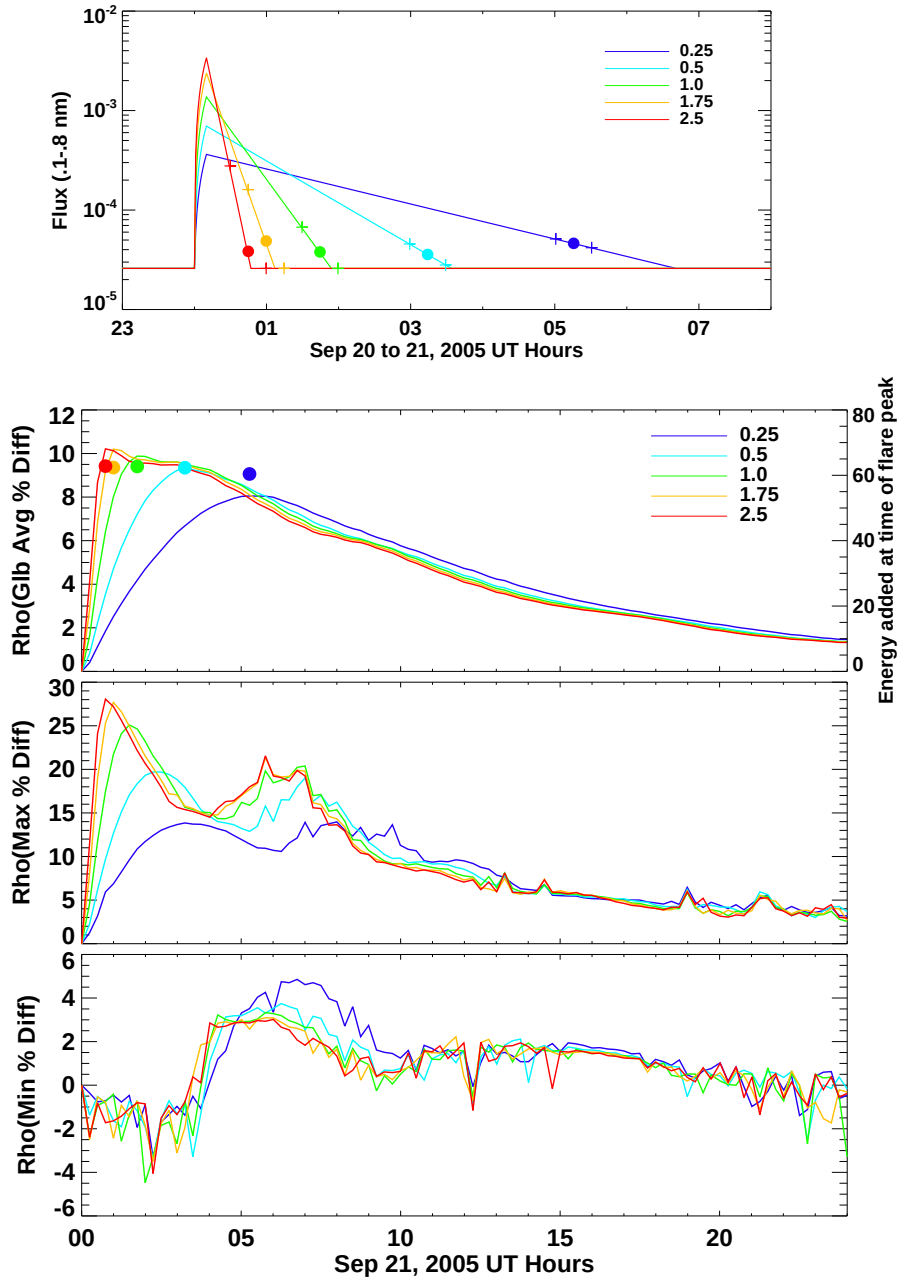

Figure 5.2: (Top) Log_{10} solar flux from .1 - .8 nm the 5 solar flares used to drive GITM. Each color represents a different peak flare magnitude, normalized to 1. Also shown are the global averaged (2^{nd} from top), global maximum (2^{nd} from bottom) and global minimum (bottom) mass density perturbations resulting from each flare. The filled circles in the global average plot indicates the total integrated energy input to the thermosphere above the background up until the time of the maximum density response.

launched on the day-side as a result of the flare. As is the case on the day-side, the night-side response is dependent on the flare magnitude. However, once again the

ratio between the night-side and day-side response is not constant. Instead, as the relative magnitude of the flare increases, the ratio decreases. For these 5 flares, the ratios are 0.76, 0.77, 0.81, 0.96, 1.0 from the largest flare to the weakest respectively.

Low background flux

GITM is run with another set of 5 flares in order to examine the effect that the background flux has on the thermospheric response. For these 5 flares, (Figure 5.3, top panel) the pre-flare solar flux, peak solar flux, and total incident integrated energy above the background have been divided by two. This results in a temporal profile for each of the flares that is very similar to those in Figure 5.2.

A comparison between the density response plots in Figures 5.2 and 5.3 shows the effect that reducing the pre-flare flux, peak flux, and total energy has on determining the magnitude of the thermospheric response. The maximum global perturbation for these 5 flares is 8.6%, 9.6%, 10.2%, 10.3%, and 10.3% for the weakest to strongest flares respectively, and the largest global maximum difference is 15.9%, 22.1%, 27.4%, 28.1%, and 28.1%. These percentages are nearly the same as those calculated for the high background flux cases. This means that thermospheric response to a large flare when the background is in a relatively excited state is the same as the response to a small flare when the thermosphere is in a low background state. In other words, for the exact same flare that is launched when the thermosphere is in an excited state vs. a low state, the response will be larger, by percentage, for the thermosphere in the low state. These numbers are a little deceiving though. Table 5.1 shows the absolute difference between each of the flares and the baseline simulation for the high and low background flux case. As expected, dividing the total energy by two results in a significantly lower absolute increases in the density during the flare. In each of the 5 cases, the resulting density increase is approximately 3.2 times as large when more energy is input into the system.

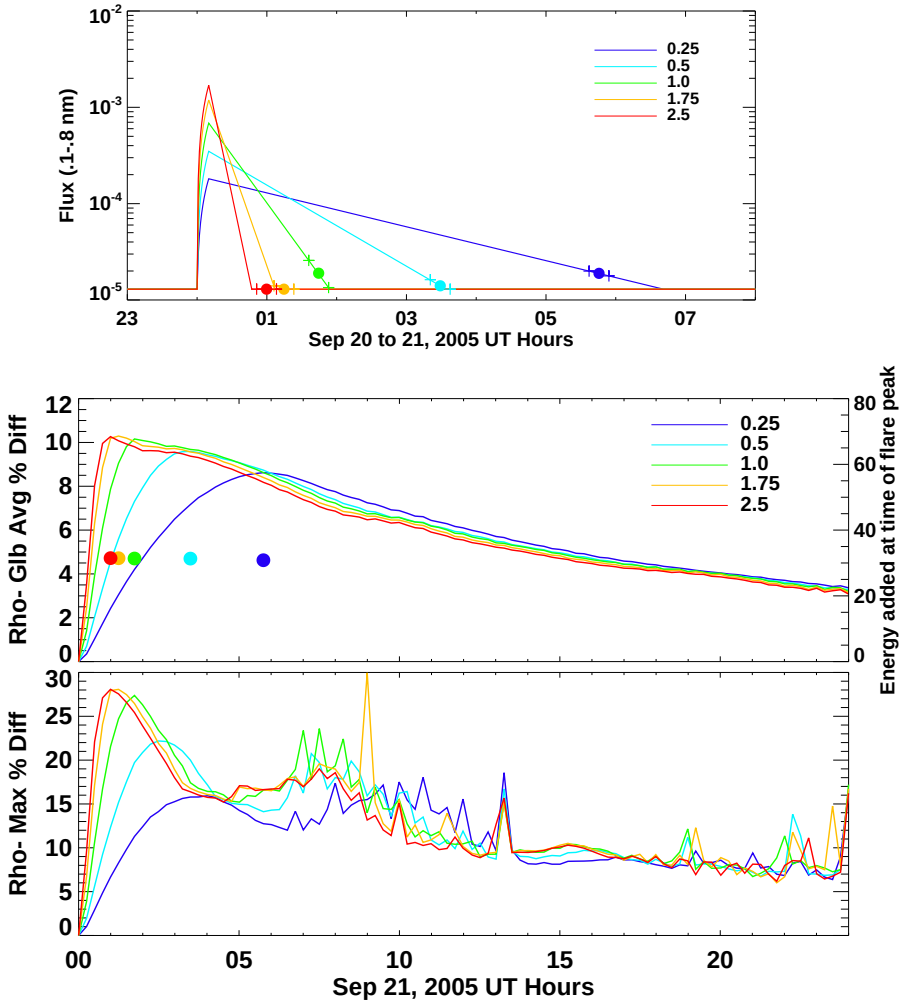

Figure 5.3: Same as Figure 5.2 except the pre-flare solar flux, peak solar flux, and total integrated energy for each flare is divided by two. Also, the global minimum difference plot is not shown.

5.3.3 Different background to peak flux time

So far, it has been determined that the total incident energy, maximum flare magnitude, and decay time are all important for determining the magnitude and timing of the density response in the thermosphere. All of the cases examined so far have resulted from flares that all have the same background to peak flux time of 10 minutes. For these next cases, the incident energy and peak magnitudes are held constant while the background to peak flux timing is changed from flare to flare.

Global Average Absolute Difference		
Flare	High Background[a]	Low Background[a]
0.25	2.90	0.88
0.5	3.60	1.10
1.0	4.06	1.27
1.75	4.26	1.32
2.5	4.29	1.32

Table 5.1: Table of global average absolute differences between each of the 5 flares and the baseline simulations for both the high and low background cases. [a]x10^{-13} kg/m^3

As is the case for the previous sets of flares, the decay time is allowed to adjust accordingly to allow the incident energy to remain constant. The solar flux profiles for these simulations are shown in the top panel of Figure 5.4. The bottom two panels of Figure 5.4 show that both the global average and the global maximum density perturbation are not strongly affected by the rise time of the flare. There is less than 1.5% relative global average difference between a flare that reaches its peak magnitude in 1 minute and a flare that does so in 40 minutes. During the first hour after the beginning of the flare, the maximum perturbation is as much as 6% larger, due to the difference in the magnitude of the flux, but after that, the relative global maximum difference is always less than 2%.

Figure 5.4 also reiterates the importance of the decay time in determining the timing of the density response. These flares are the only ones that end within 30 minutes of each other. As a result, the peak density perturbations all occur at approximately the same time.

5.4 Discussion on the impact of flare characteristics

The use of synthetic solar flux data makes it possible to study the effects of some of the important characteristics of a solar flare on the thermosphere, independently. In this study, the effect that the total time integrated incident energy, peak flare EUV

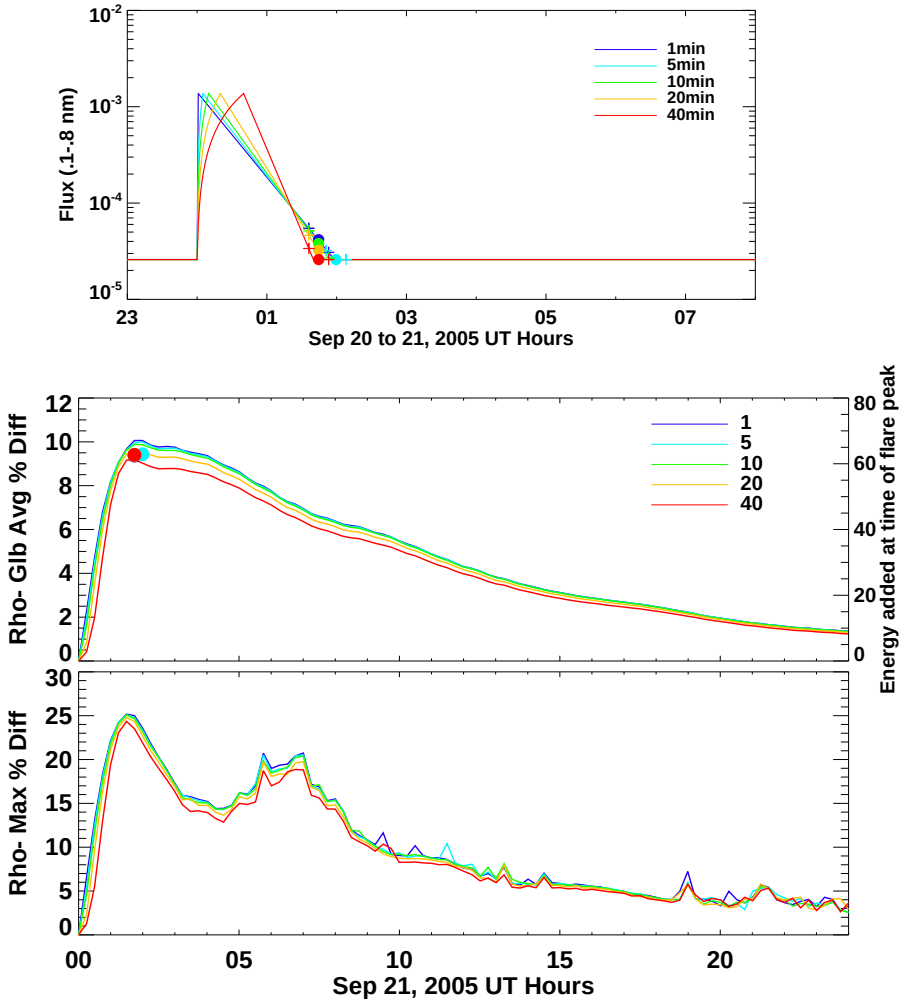

Figure 5.4: (Top) Log_{10} solar flux from .1 - .8 nm for the 5 solar flares used to drive GITM. Each color represents a different peak time. Also shown are the global averaged (middle) and global maximum (bottom) mass density perturbations resulting from each flare. The filled circles in the global average plot indicates the total integrated energy input to the thermosphere above the background up until the time of the maximum density response.

flux, background flux, background-to-peak flux elapsed time, and flare decay time have on the thermospheric density at 400 km have been investigated. It is found that of these, the global average density response and the magnitude of the global minimum perturbation are linearly dependent on the total integrated energy. The integrated energy and the peak flare magnitude both contribute to the global maximum response (while the relationship is somewhat linear for the integrated energy, it is not for the peak flare magnitude). In addition, while the background-to-peak flux time duration

has little affect on the response of the system, the decay time is very important in determining the timing of the peak global average response. This last point helps to shed light on the fundamental physical processes that are responsible for the overall response of the system. It seems somewhat logical to expect that the maximum global response occur at a fixed time after the peak of the flare. The fact that that the maximum response occurs when the solar flux has nearly returned to a background level means that, on a global scale, the thermosphere is slow to respond to a change in solar forcing. During a solar flare, the additional energy being input into the thermosphere heats the gas in the region that the energy is absorbed (from 100 - 200 km). As a result the gas expands, and at higher altitudes, the density increases because the denser gas from below is pushed upwards. In order for the atmosphere to relax back to a nominal state, the additional energy needs to be lost somehow. The primary loss mechanism for this extra energy is nitric oxide (NO) cooling (Figure 1.6). The loss processes are slow, however, and the system only reaches equilibrium (global energy in equals global energy out) when the extra solar energy coming into the system has nearly returned to the background level.

To try and better quantify the balance of energy in the system, Figure 5.5 shows the temporal profile of the global average NO cooling difference between each of the flares described in 5.3.2 and the baseline simulation, at 155 km, at a time resolution of 30 minutes (as opposed to 15 for the density results above). Figure 5.5 shows that the nitric oxide cooling responds on both short time scales and long time scales. This is determined by noting how quickly the cooling increases after the start of the 2.5 flare, yet how long the perturbations last, even though the flares all have ended by 7 UT. Since the most important characteristic of the flare when determining the global average density response is the incident energy, and if it is assumed that NO cooling is the dominant energy loss process, one can come up with an empirical formula to predict the behavior of the system during and following a solar flare. Simplistically,

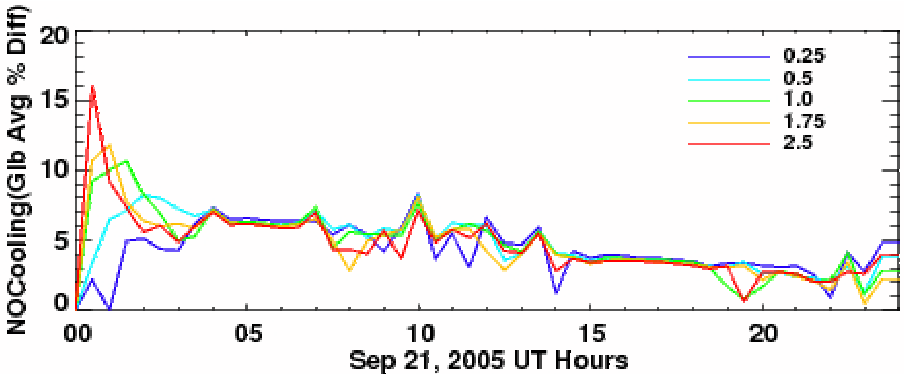

Figure 5.5: NO cooling global average percent difference for the flares described in section 5.3.2.

such a formula should be of the form:

$$\rho(t) = \rho(t-1) + A \cdot E(t) - B \cdot Q_{NO}(t) \tag{5.1}$$

where A and B are weighting coefficients, E is the energy as a function of time, t, and Q_{NO} is the time dependent NO cooling. The second term on the right hand side of Equation 5.1 is simply due to the incident EUV energy at the time of interest. The NO cooling term in Equation 5.1 should also be dependent on the EUV energy being absorbed by the system, since it is this energy that is perturbing the NO density, leading to the enhanced cooling, however, as suggested by Figure 5.5, this term is not only due to the instantaneous energy being absorbed, but also the energy that was absorbed several hours prior to the time of interest. Therefore, one can write a formula such as:

$$Q_{NO}(t) = a_1 E(\Delta t_{0.25}) + a_2 E(\Delta t_{0.5}) + a_3 E(\Delta t_1) + a_4 E(\Delta t_2) + \ldots + a_n E(\Delta t_{24}) \tag{5.2}$$

where a_n are weighting coefficients that specify the relative importance of each of the terms, and $E(\Delta t_n)$ refers to the total energy absorbed in the t_n hours prior to the current time.

Using the above formulation, the equations:

$$\rho(t) = \rho(t-1) + 0.06(1.0E(\Delta t_{0.25}) + 0.1E(\Delta t_{0.5}) - 0.327NO(t) - (0.01\frac{\rho(t-1)}{NO(t)+0.01})) \quad (5.3)$$

$$NO(t) = 0.2E(\Delta t_{0.25}) + 0.1E(\Delta t_2) + 0.4E(\Delta t_6) + 1.2E(\Delta t_{12}) + 1.2E(\Delta t_{16}) \quad (5.4)$$

can be obtained that describe the density and NO cooling enhancements at a specified time, t, based on the density at the previous time and the total integrated energy above background into the system 0.25, 2, 6, 12, and 16 hours prior to the time of interest.

Figure 5.6 shows the results of this simple formula for the flares discussed in the first half of section 5.3.2. The calculated density perturbation is within 1% for all of the flares, the time of the maxima are always within 15 minutes. By about 20 hours after the beginning of the flare, the NO cooling enhancements have all returned to zero. Since the flares have long since ended, both the energy in and the energy loss rates should be zero, and this would mean that the global average density would have a zero gradient. However, the GITM simulations suggest that the NO cooling is still slightly perturbed at this time, and this long after the flares, the thermosphere is expected to have a negative gradient so as to push the system towards its unperturbed state. For this reason, the last term in Equation 5.3 has been added. This is a small term that becomes important only when NO cooling becomes small, and acts to ensure that the system returns to it's background state. This term is justified since this simple formula only accounts for nitric oxide cooling as a loss process. In reality, there are other losses such as oxygen cooling and conduction that play a role in returning the system to an unperturbed state. At first glance, one would expect this term to be dependent on energy in, since if the EUV flux never returns to background levels, then the system should not continue to relax to its previous state. This, in fact is the case, since the NO term is dependent on the energy in. In such a case, when the

post-flare EUV flux is larger than the background, or pre-flare, flux, then the post-flare NO cooling term will be larger than zero, and the final term in Equation 5.3 will not be important, eventually allowing the positive EUV energy term to balance the positive NO cooling term, resulting in a constant, positive density enhancement.

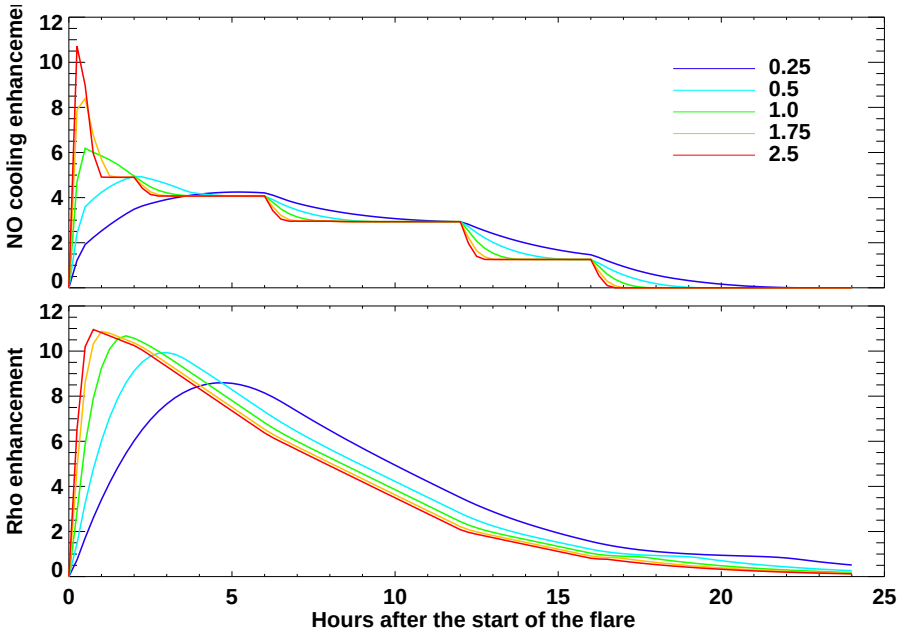

Figure 5.6: NO cooling percent enhancement (top) and density enhancement at 400 km (bottom) for 24 hours following the solar flares described in section 5.3.2 as calculated by equations 5.4 and 5.3.

Figure 5.7 shows the density response to the September 7, 2005 X17 flare that occurred at 19:40 UT using this formula. The maximum global average perturbation calculated during the response is about 14%, roughly 1.5% lower than what GITM suggests the maximum enhancement to be. Much of the error is primarily the result of the choice of the pre-flare solar flux. This is a difficult decision to make since this value is rarely constant. Equations 5.3 and 5.4 were developed using the synthetic data described in this chapter, and therefore, the solar EUV temporal profiles consisted of a constant value prior to, and after, the flare. This certainly is hardly the case in reality. Rather, in calculating the response, a mean flux value needs to be obtained based on the flux prior to the flare. The duration of time used to calculate the average

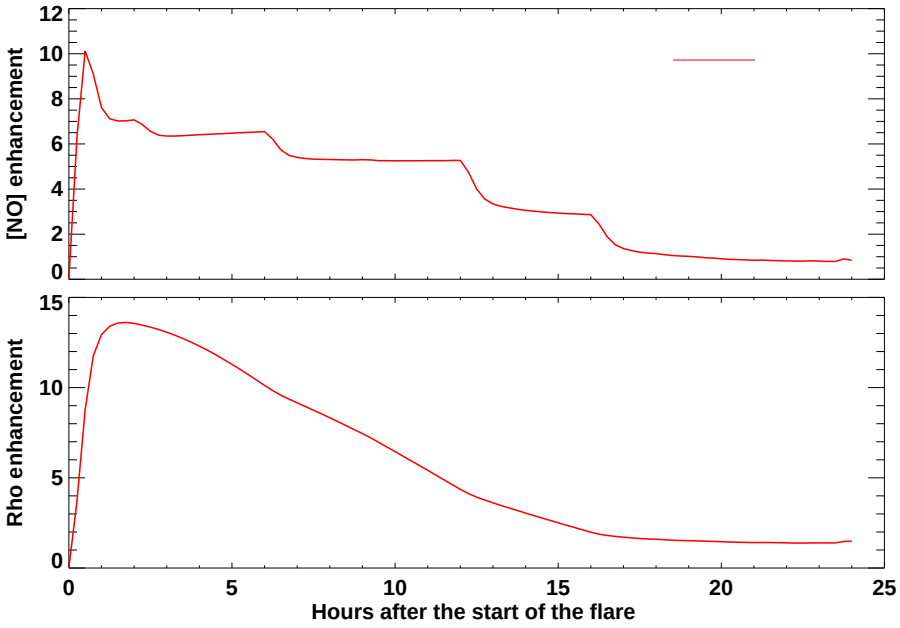

Figure 5.7: Density enhancement at 400 km for 24 hours following the solar flares that occurred on September 7, 2005, calculated using equations 5.4 and 5.3.

flux is dependent on how dynamic the flux is prior to the flare. In addition, oxygen cooling and conduction certainly play a role in removing the extra energy from the system, and diffusion will assist in the removal of excess density. None of these factors are meant to be accounted for by such an equation, rather, the goal is to show that it is possible to come up with a simple formula based on knowledge only of the energy being added to the system, that does a reasonable job of calculating the perturbation in NO cooling, and how the resulting increase in radiative cooling balances the excess energy to determine the thermospheric density enhancement.

The discussion of flare characteristics in this chapter has primarily focused on one type of flare, since the synthetic data used is based on a single flare. It may be expected that different flares that are launched from different regions of the sun may not always behave in the same manner. What is meant is that the temporal profile of a solar flare over all EUV wavelengths may not always be the same from flare to flare. An example of this is illustrated in Figure 5.8, where the percent difference between the peak flux and the pre-flare flux is shown vs. wavelength for the October 28, 2003,

November 02, 2003, September 7, 2005, and September 9, 2005 solar flares. In order to make comparison easy, the percentages have been normalized to the November 02, 2003 flare. Figure 5.8 shows that the solar flux increase at every wavelength between flares is not always the same. It this were the case, each line would be perfectly horizontal. The difference between the size of the flare would be evident by the shift of the horizontal line. In reality, different flares have different responses at different wavelengths. It is interesting that the October 2003 flare line is in fact nearly horizontal. This is because this flare came from the same sunspot group as the November 2003 flare. The September 7, 2005 flare shows a much stronger relative increase in the X-rays than do the other flares, as well as the wavelength region of the spectrum from 90–105 nm. The consequences of these differences on the Earth's

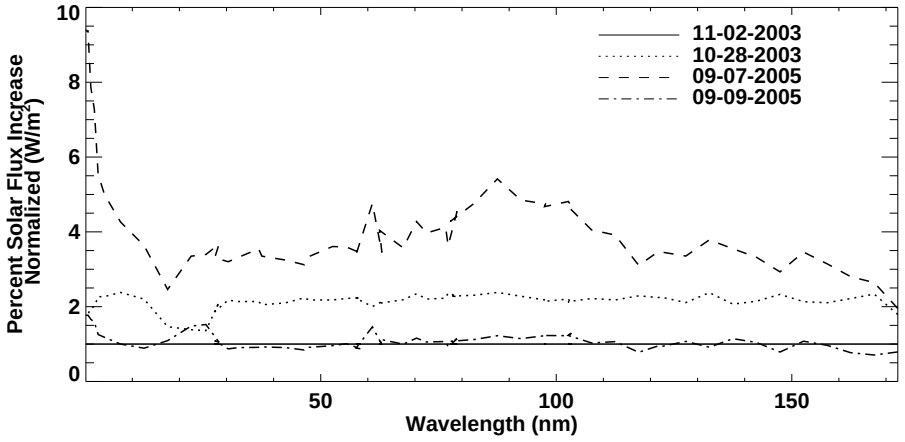

Figure 5.8: Percent difference between peak solar EUV flux and pre-flare EUV flux vs. wavelength for 4 solar flares, normalized to the 11-02-2003 flare.

upper atmosphere are an interesting topic for future studies.

CHAPTER VI

Thermospheric Observations During Flares

6.1 Introduction

In this chapter, data from several upper atmospheric instruments are presented to show that observations of thermospheric variables can capture perturbations that occur following the onset of a solar flare. Specifically, two time periods are discussed, during which multiple solar flares occurred within several days of one another. Chapter I outlines some of the issues with performing an analysis of the upper atmospheric response to solar flares using satellite measurements. Ideally, observations of mass density, neutral temperature, or the number densities of some of the important neutral species would be used for an in-depth statistical study to further support the results of the model. However, measurements of such quantities are quite rare for a number of reasons. For one, there are a limited number of instruments in orbit that make measurements of thermospheric quantities in general. This is due to the amount of funding for missions to do aeronomic research. In addition, low-uncertainty measurements of quantities such as temperature and mass density are difficult to obtain due to the tenuous nature of the thermosphere.

Chapter III demonstrated that the largest density perturbations in the thermosphere occur near solar zenith angles (SZA) of 0° and 180°, or near the sub- and anti-solar points. Therefore, it would be ideal to have many measurement datasets

for all of the large solar flares, where the measurements are taken at low SZAs and at time-scales of less than a few minutes. While there are thermospheric observations that sample low SZAs, the fact that there are really only a few instruments collecting data of interest to this study means that it is impossible to simultaneously have good geographical coverage, at high temporal resolution, for every solar flare that occurs. The measurements available from Champ, GUVI, and SABER do, however, allow for event-by-event analysis of a few solar flares, and so it is the goal of this chapter to show that in addition to the measurements presented in Chapter III, observations can capture the effects of solar flares on the thermosphere. Ultimately, this chapter demonstrates two main points: 1) There are observations that show that the thermosphere can be significantly affected by solar flares; and 2) the response of the thermosphere to solar flares is different on a case-by-case basis, and while observations may capture the perturbations that result from one solar flare, they may not observe any effect in the atmosphere for another. While a detailed data-analysis of solar flare events is an important study, and something the author would like to accomplish as part of the future work on this topic, this chapter further illustrates the extreme difficulty in performing such a study.

6.1.1 Datasets

In addition to the mass density data from the Champ satellite, which has already been discussed in this thesis, there are a few other instruments that have provided measurements during X-class solar flares.

The GUVI instrument has been providing altitude profiles of atomic oxygen and molecular oxygen and nitrogen since 2002. GUVI is an ultraviolet spectrograph that measures photons emitted by the gas in the thermosphere in a swath that is approximately 3000 km wide in a typical orbit that covers day, night, and auroral locations. It accomplishes this by performing cross-track scans of the Earth every 15 seconds. In

addition to performing a disk scan, the instrument is capable of viewing the Earth's limb between angles of 67.2° and 80° from nadir, which corresponds to tangent point measurements from 152 km to 592 km above the horizon, obtained from a distance of 1215 km. The instrument samples all latitudes every 90 minutes as a result of the orbital period of the TIMED satellite.

Also on-board the TIMED satellite, the SABER instrument has provided O_2, CO_2, NO, and other volume emission rates since 2002. SABER takes measurements of infrared emissions by sounding the atmosphere from the surface up to about 180 km at both day-side and night-side locations. It performs observations by scanning the Earth's limb once every 58 seconds, and collects measurements covering 15 longitude bands (that are all at the same solar local time) each day due to the TIMED satellite's 90 minute orbit.

6.2 Observations

The above mentioned instruments all began taking measurements around the beginning of 2002. Since then, there have been many large X-class flares. On two separate occasions, multiple flares occurred within 2 days of one another. Such events are ideal for comparison because each of the sets of flares in these instances will have formed under similar background solar conditions. Therefore, the spectral profiles should be similar between each of the flares in a set. The first set occurred between November 2, 2003 and November 5, 2003. During this time period there was an X8 flare on the 2^{nd} at 17:15 UT, an X3 and an X4 flare on the 3^{rd} at 1:20 and 9:50 UT, and an X18 flare on the 4^{th} at 19:40 UT. The second set occurred in September 2005: an X17 flare on the 7^{th} at 17:25 UT, an X5 flare on the 8^{th} at 21:00 UT, and an X3 followed by an X6 at 9:55 and 19:35 UT, respectively, on the 9^{th}. A summary of these flares is presented in Table 6.1, and the GOES data for these events are plotted in Figures 6.1 and Figures 6.2. Figures 6.3 and 6.4 show the locations of observations

Flare magnitude	Date	Time (UT)
X8	11/02/2003	17:15
X3	11/03/2003	01:20
X4	11/03/2003	09:50
X18	11/04/2003	19:40
X17	09/07/2005	17:25
X5	09/08/2005	21:00
X3	09/09/2005	09:55
X6	09/09/2005	19:35

Table 6.1: X-class solar flares during two time periods

up to 90 minutes after the flares, for the X8(left) and X18(right) flares that occurred in November 2003 and the X17(left) and X6(right) flares that occurred in September 2005.

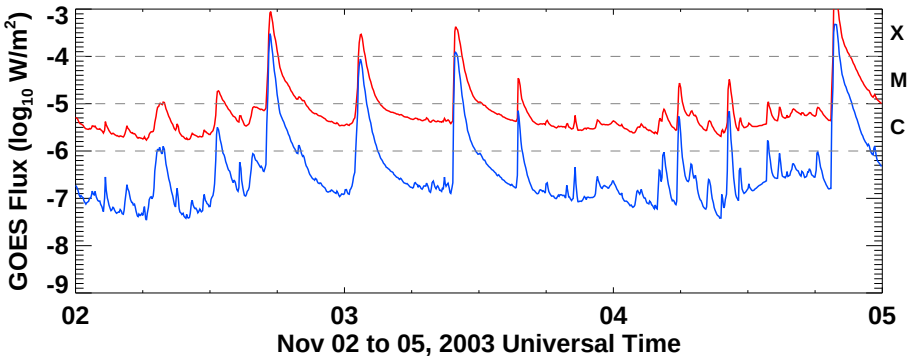

Figure 6.1: GOES data from November 2–5, 2003.

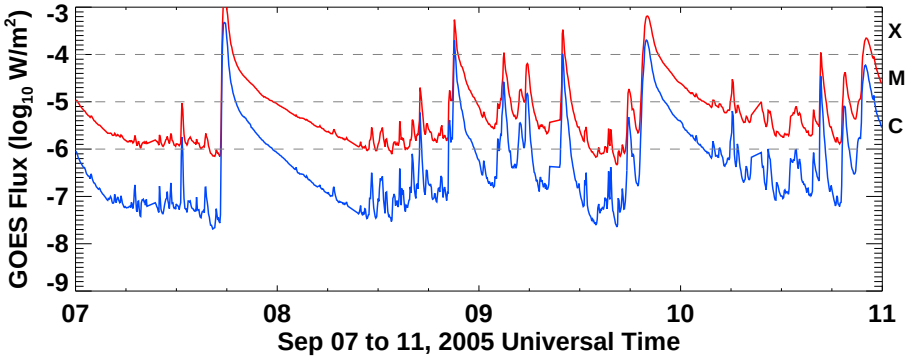

Figure 6.2: GOES data from September 7–11, 2005.

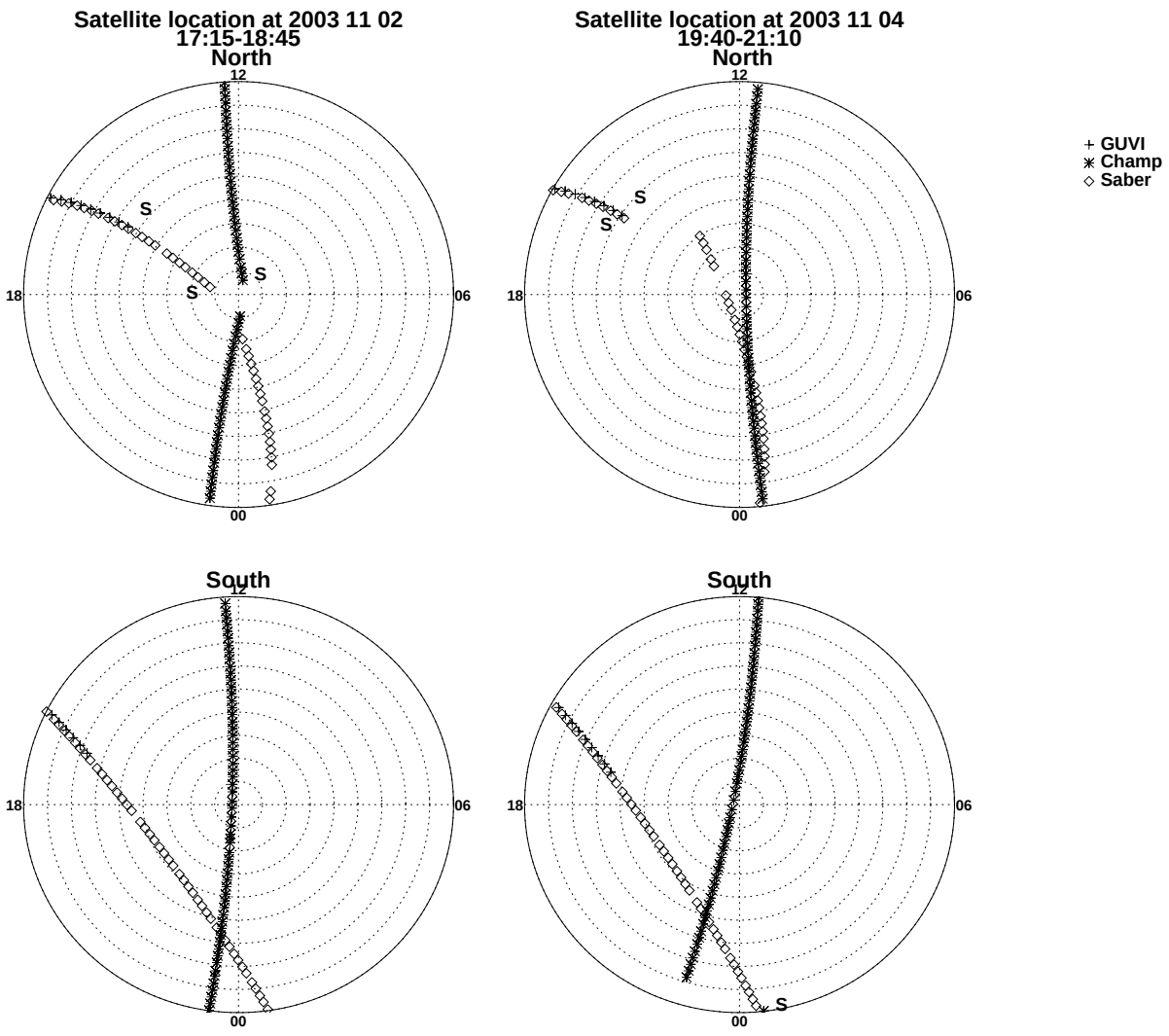

Figure 6.3: Observation locations for 11/02/2003 (left) and 11/04/2003 (right) flares for 90 minutes following the onset of the flares. The S characters denote the start of the orbit.

In Figures 6.5, 6.6, and 6.7, O_2 number density observations from GUVI, mass density from the Champ satellite, and O_2 volume emission rates from SABER are shown during the November 2003 events. In addition, GITM simulations have been performed for this time period for comparison purposes. As is the case for all the simulations performed in this thesis, high-latitude forcing has been held constant. The solar EUV flux is the only external driver that is allowed to vary, and it is specified by FISM. This means that any perturbations in the data due to other forcing, such

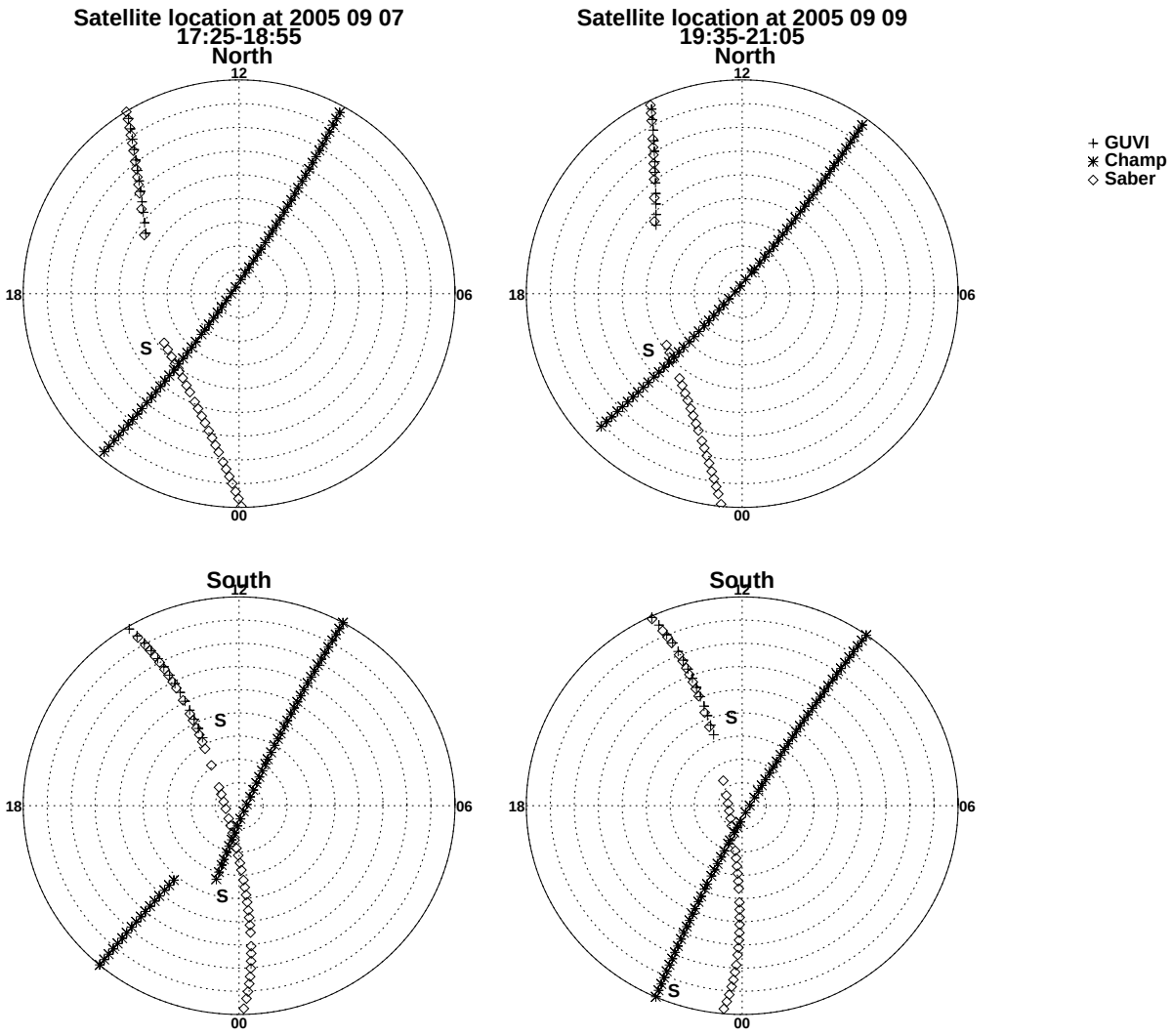

Figure 6.4: Observation locations for 09/07/2005 (left) and 09/09/2005 (right) flares for 90 minutes following the onset of the flares. The S characters denote the start of the orbit.

as geomagnetic, will not be captured by the model. During each of the simulations, GITM flies a virtual satellite through the model for Champ, GUVI, and SABER, and extracts data at the exact measurement locations.

The GUVI measurements shown in Figure 6.5 indicate that there is significant variability throughout the three day period. In particular, there are relatively short enhancements that occur at all altitudes just before 18 UT on the 2^{nd} as well as just prior to 20 UT on the 4^{th}. Both of these features correspond to the two largest

of the 4 flares that occur during this time period. In addition, there is a broader enhancement that takes place on the 3^{rd}. By looking at the $[O_2]$ at 156 km, one can see a clear jump in the density around 3 UT, and then another disturbance at about 8 UT. The cause of these features and the reason for the broad enhancement that lasts throughout much of the day is difficult to explain. It is possible that the density increase around 3 UT is due to the X-class flare that begins at 1:20, but the increase at 8 UT occurs prior to the next X-class flare.

In order to examine the possibility that geomagnetic activity is responsible for the response in the data, the D_{st} and Kp indices are shown in the bottom panels of Figure 6.5. D_{st} gives an indication of the strength of the inner magnetospheric current systems using observed perturbations of low-latitude ground-based magnetic fields, i.e., due to the ring current. Large negative values suggest that there is significant current density in the ring current, and thus it is likely that a geomagnetic storm is occurring. The Kp index is calculated based on global perturbations to the magnetic field, and large values indicate significant magnetic activity. There is clear activity that occurs on the 4^{th}, however, on November 3^{rd}, D_{st} is relatively small and constant, and Kp is always around 3. This means that the density perturbations observed in the GUVI data are not likely to be caused by geomagnetic forcing, and suggests that the flares are most likely to be partially responsible for the enhancement. Given the short time in between each of the flares, the observations suggest the possibility that perturbations launched by one flare are interacting with those launched by another. This sort of preconditioning is a topic of interest within the thermospheric community, especially due to the occurrence of geomagnetic storms following flares, sub-storms, or even other storms. This topic is outside the scope of the current work, but is anticipated to be the subject of future study.

Figure 6.6 shows orbit averaged mass density results as observed by Champ and the corresponding GITM results taken at the Champ satellite locations. The mass

density is enhanced due to the flare one the 2^{nd} by more than 15%. However, any perturbation that results from the flare on the 4^{th} is difficult to see since the thermosphere is still in a perturbed state as a result of the geomagnetic activity that occurs on earlier in the day. This geomagnetic activity does not have such large an effect on the SABER observations. In Figure 6.7, O_2 volume emission rate observations from SABER are shown along with GITM O_2 number density results from November 2–5 at 110 km. The SABER data show clear density enhancements following both the November 2^{nd} flare and the November 4^{th} flare. On the 2^{nd}, the emission rate increases by more than 20% and a perturbation of similar magnitude occurs on the 4^{th}. Unlike the GUVI observations, SABER does not show any perturbation throughout the 3^{rd}. This is probably a result of a combination of the SABER observations being lower in the thermosphere and the relatively low magnitude of the flares that occur on the 3^{rd}.

GUVI observations and GITM results during the September 2005 events are shown in Figure 6.8 at 156 and 387 km, along with the SZA of the measurement locations, and the D_{st} and Kp indices. Following the two largest flares that occur during this time period, the X17 on September 7, and the X6 on September 9, both the measurements and the model results indicate that the O_2 density is perturbed, at least at the higher altitude level. After the first flare, GUVI observations show that the orbit maximum $[O_2]$ is enhanced by more than 300%. After the flare on the 9^{th}, the orbit maximum density increases by more than an order of magnitude.

It should be noted that there is a sudden jump, or a sudden commencement, in the D_{st} index around 14 UT on the 9^{th} that is caused by an increase in the magnetopause current that results from a pressure impulse in the solar wind compressing the dayside magnetosphere. Following the sudden commencement, the D_{st} values decrease moderately. Also, throughout this time, Kp is around a value of 4. These are all signs that there is slightly enhanced geomagnetic activity occurring, and that the observed

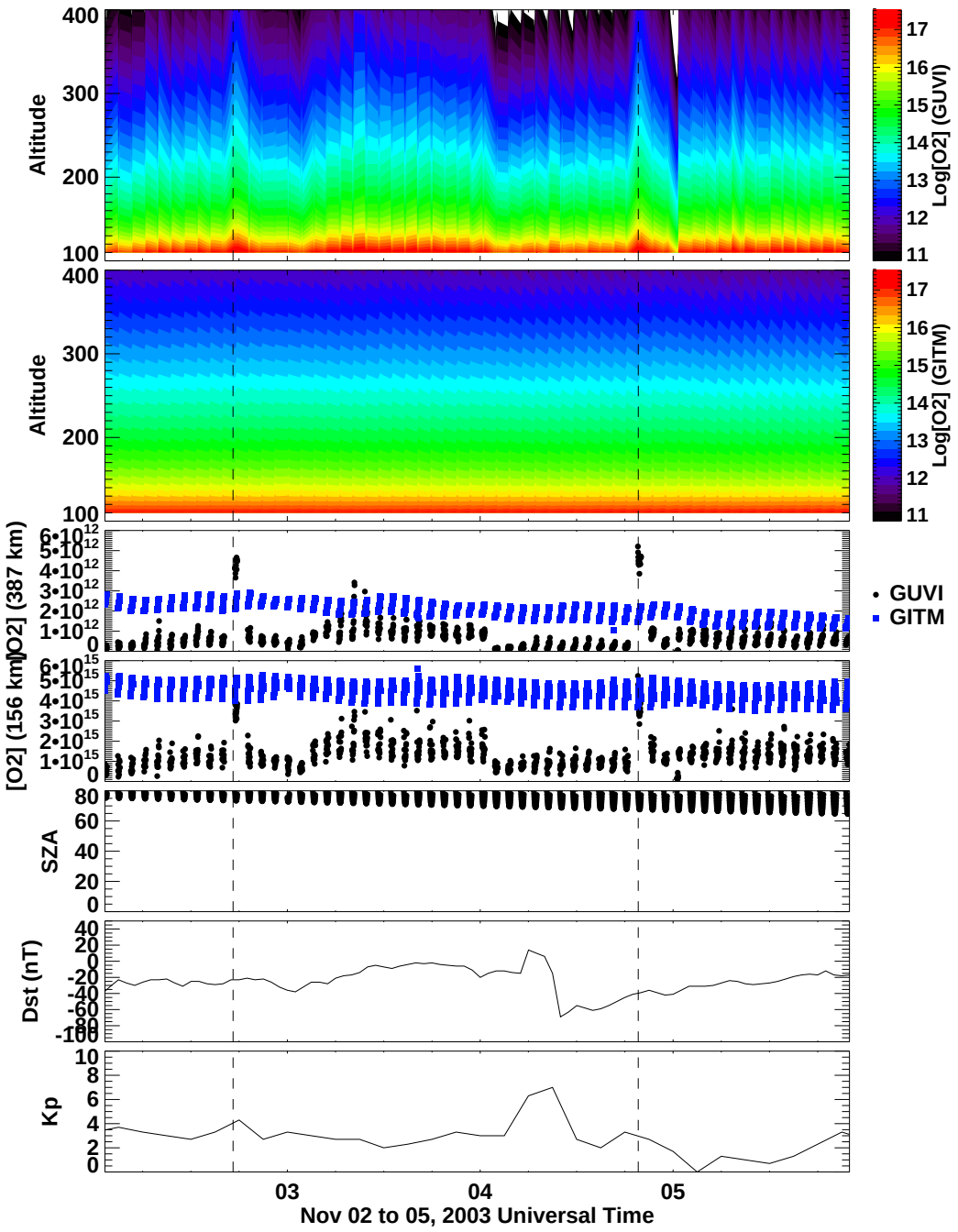

Figure 6.5: (Top) Altitude profile vs. time for the $[O_2]$ measurements from GUVI from November 2, 2003 though November 6, 2003. (2^{nd}) Altitude profile vs. time for the corresponding GITM results. (3^{rd} and 4^{th}) GUVI observations (black circles) and GITM results (blue circles) at 387 and 156 km respectively. The solar zenith angles of each measurement, the D_{st} index, and the Kp index are shown in the bottom 3 panels. The vertical lines indicate the start time of the two largest flares that occurred during this time period.

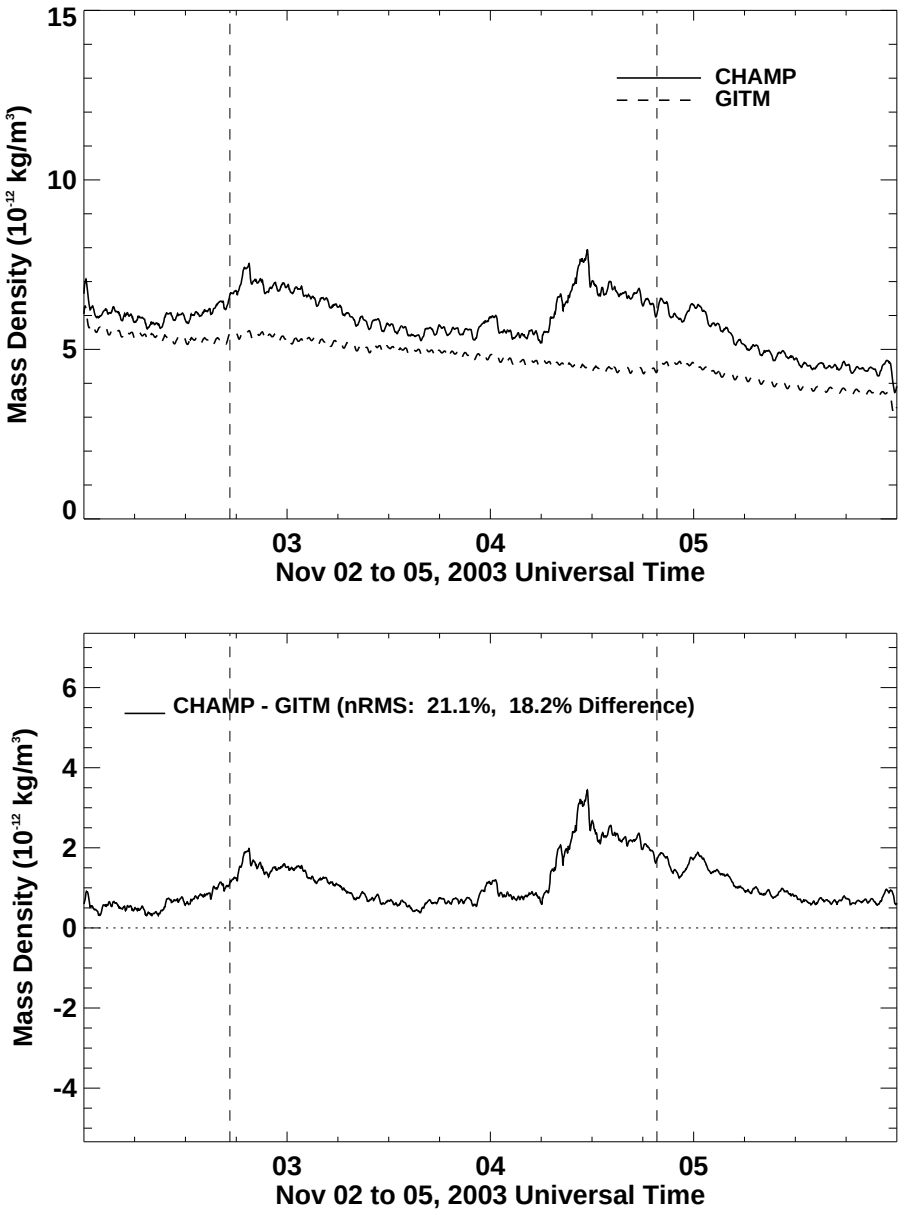

Figure 6.6: (Top) Orbit averaged density measurements from Champ (solid line) and model results from GITM (dashed line) near an altitude of 400 km from November 2, 2003 through November 6, 2003. (Bottom) Difference between the Champ measurements and the GITM results. The vertical lines indicate the start time of the two largest flares that occurred during this time period.

$[O_2]$ enhancement may be affected by this activity.

Despite Champ showing a significant perturbation during the November 2, 2003 flare, the mass density observations in Figure 6.9 show no response following the September 7^{th} flare, even though it is significantly stronger. In addition, Figure 6.9

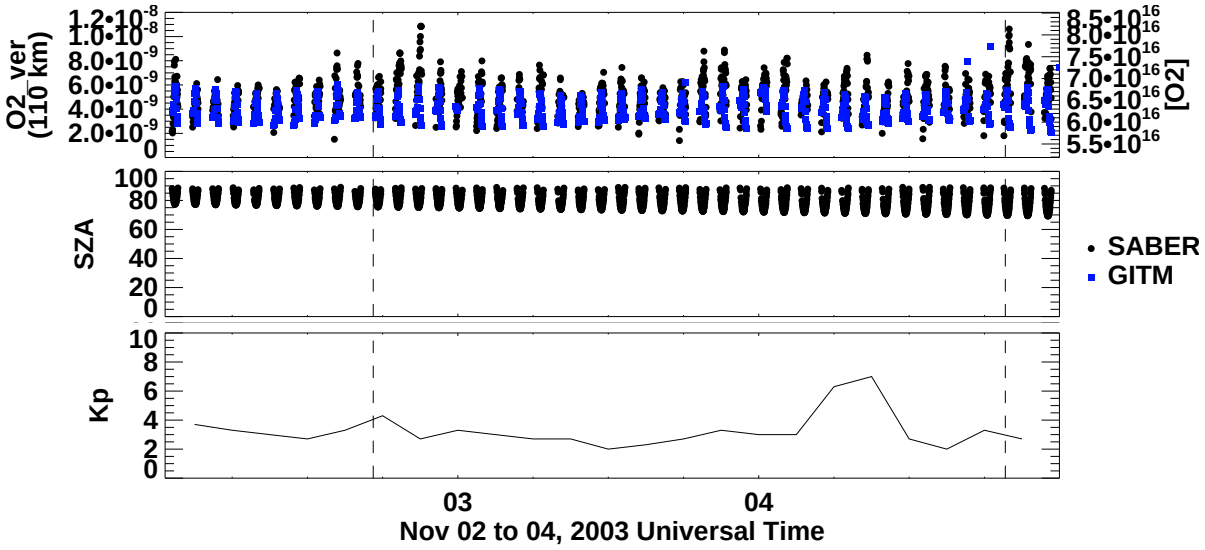

Figure 6.7: SABER O_2 volume emission rate data (black circles) and GITM [O_2] results (blue circles) at 110 km from November 2 through November 5, 2003. The solar zenith angle of the SABER measurement locations is also shown (middle) as is the Kp index (bottom) for reference. The vertical lines indicate the start time of the two largest flares that occurred during this time period.

further suggests that geomagnetic activity is affecting the thermosphere during the later half of the day on the 9^{th}. This is demonstrated by the steady increase in density beginning after noon and the lack of such and increase in the model results, which are shown as the dashed line in Figure 6.9. However, just after the onset of the flare on the 9^{th}, the Champ orbit averaged observations by just over 10%. GITM shows a similar increase in the density at this time. Given that the flare on the 7^{th} is significantly stronger than the one on the 9^{th}, it is strange that the observations show no perturbation on the second, but do capture a response on the 9^{th}. This may be do to the satellite being in the wrong place at the wrong time. Figure, 6.4 shows that on the 7^{th}, Champ is in an orbit that does not reach very low solar zenith angles, where the perturbation magnitudes are the largest, and therefore, most likely to be observed.

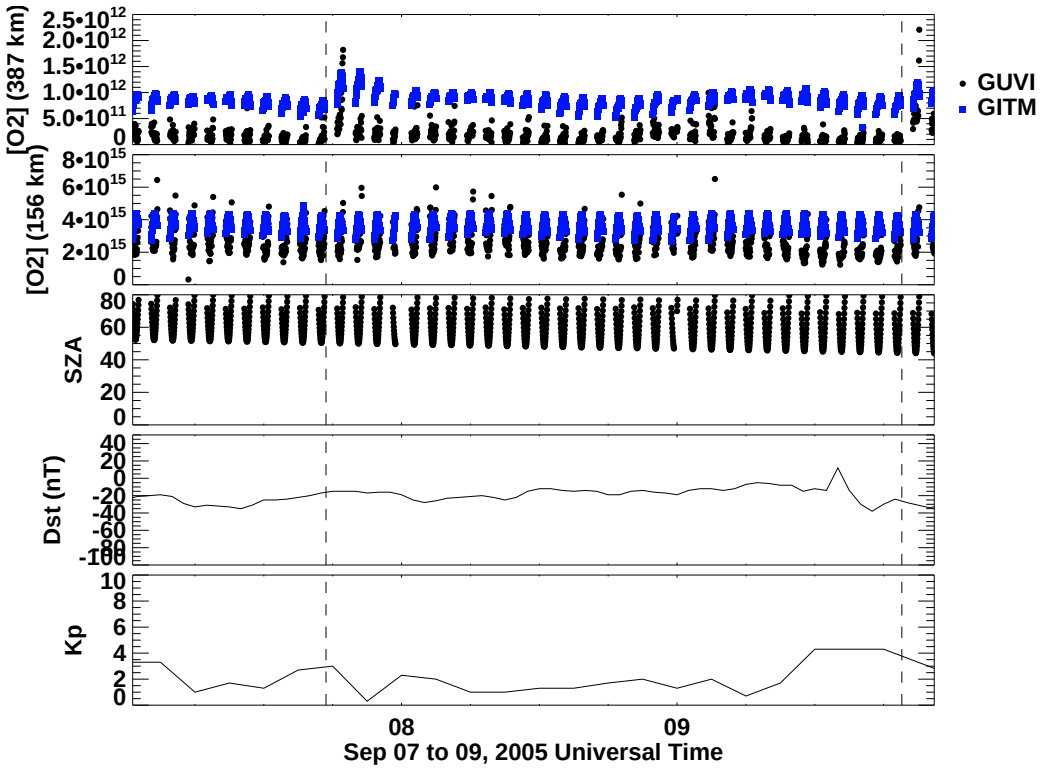

Figure 6.8: Similar to Figure 6.5 for September 7–10, 2005, except the altitude contour plots are not shown.

6.3 Difficulty with comparing model and data

Ideally, during time periods when one or more of the instruments show the thermosphere being affected by a solar flare, the GITM results would also show a response at a corresponding location within the model domain. This, however, is not always so. During the November 2003 events, GUVI (Figure 6.5) and SABER (Figure 6.7) both indicate that the thermosphere is disturbed during the orbit following the flares, at a range of altitudes. Conversely, GITM shows very little change in the $[O_2]$ at the measurement locations. This is also the case with the Champ mass density, as shown in Figure 6.6. The GITM results show a slight increase in the density coinciding with the two flares on the 2^{nd} and the 4^{th}. However, these enhancements are very small compared to the perturbations in the Champ observations. Figure 6.11 shows the global density enhancement as predicted by GITM following the flare on Novem-

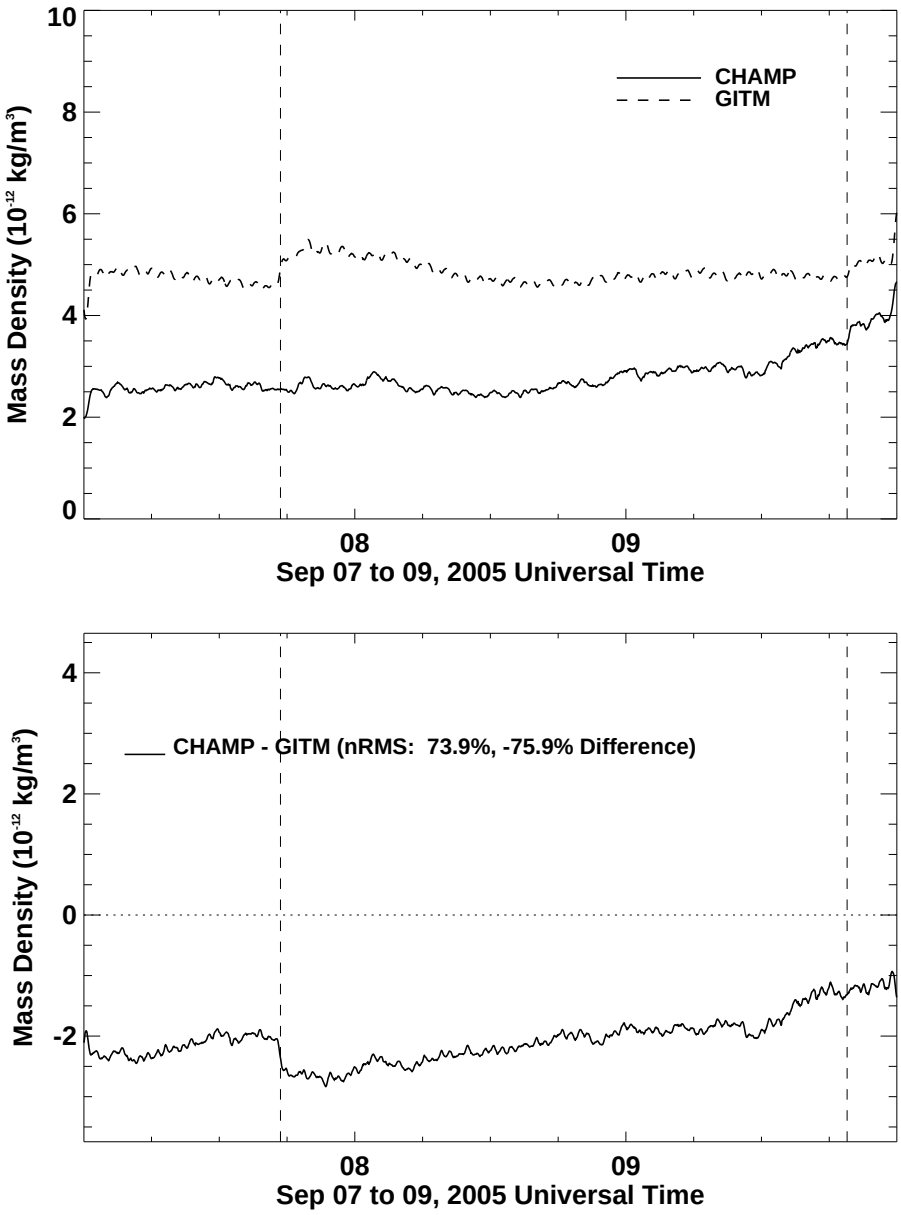

Figure 6.9: Similar to Figure 6.6 for September 7–10, 2005.

ber 2, 2003. The contour is taken at 19:30 UT, corresponding approximately with the time that the maximum occurs in the Champ observations. GITM indicates the maximum density perturbation at this time to be only 2.9%. Champ, however, observes a maximum density enhancement of more than 15%. In Chapter III, GITM showed that the maximum percent increase in density on the day-side following the Halloween flare was 15%. This is significantly smaller than the Champ observations

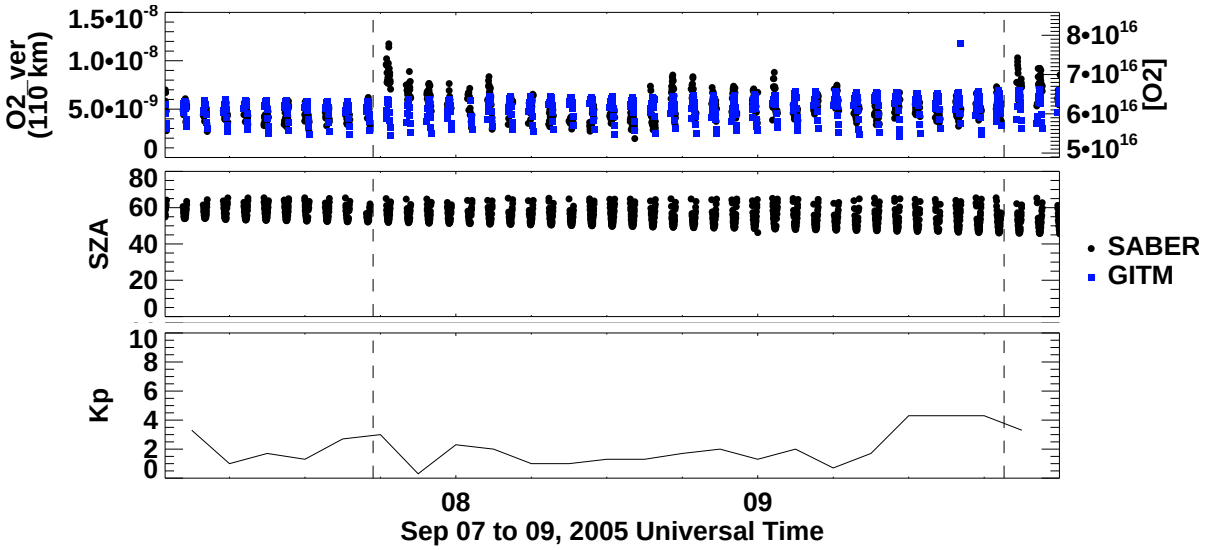

Figure 6.10: Similar to Figure 6.7 for September 7–10, 2005.

suggest (45%) and GITM again underestimates the magnitude of the response to these solar flares.

There are several possible reasons that GITM underestimates the response following a solar flare. As discussed in Chapter II, GITM uses many different parameters to account for physics that is too complicated or not well enough understood to be included in the model. Also, there is some uncertainty involved with the solar flux data, both SEE and FISM, being used to drive the model. Perhaps the most important reason that GITM underestimates the response has to do with how the model itself captures the incident energy. During a solar flare, it is typically the most energetic parts of the soft X-ray and EUV spectrum that experience the largest enhancement. Photons at these wavelengths are absorbed by the thermosphere below the 100 km level. Since the lower boundary of GITM is at 100 km, the additional energy being input into the system is not being captured within the model. GITM makes use of MSIS at the lower boundary, therefore it is theoretically possible that GITM would still be affected by the energy absorbed below 100 km, because MSIS is dependent on the solar flux, and perturbations in the temperatures could be capture by MSIS

during flare conditions. However, MSIS is driven by the $F_{10.7}$ proxy, which is only updated once per day, and does not capture solar flares. This means that GITM's lower boundary, set by MSIS, is not affected by the change in solar radiation during a solar flare. Therefore, any changes in the amount of solar radiation that is absorbed below 100 km has no effect on the model.

In addition to the possibility of GITM underestimating the response, a close look at the Champ observations suggest other factors may be influencing the observed density following the flare. Figure 6.12 shows a contour of the Champ day-side neutral density throughout November 2^{nd} as a function of Universal time and latitude. In the northern high-latitudes, the observations show a density enhancement that propagates southward beginning around 14:00 UT. This indicates that in addition to solar forcing, other external drivers have an effect on the thermospheric density at this time. Thus, the density increase measured by Champ is at least in-part due to sources of dynamic forcing besides the flare, which are not included in the model for this simulation.

Following the September 2005 flares, the model shows a larger response in the

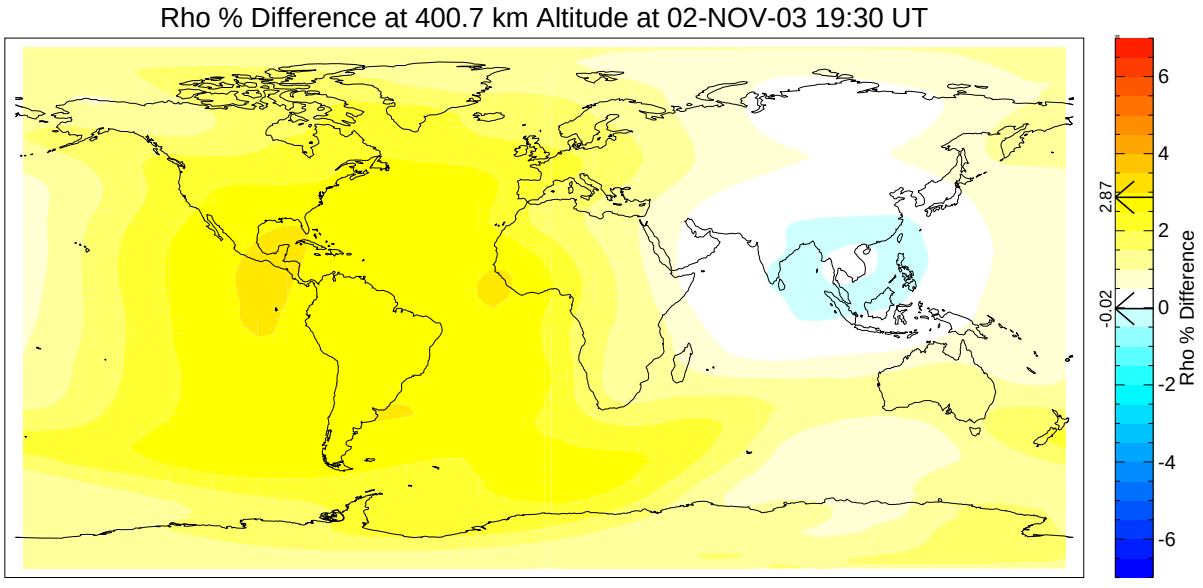

Figure 6.11: Neutral density perturbation on 11/2/2003 at 19:30 UT from GITM.

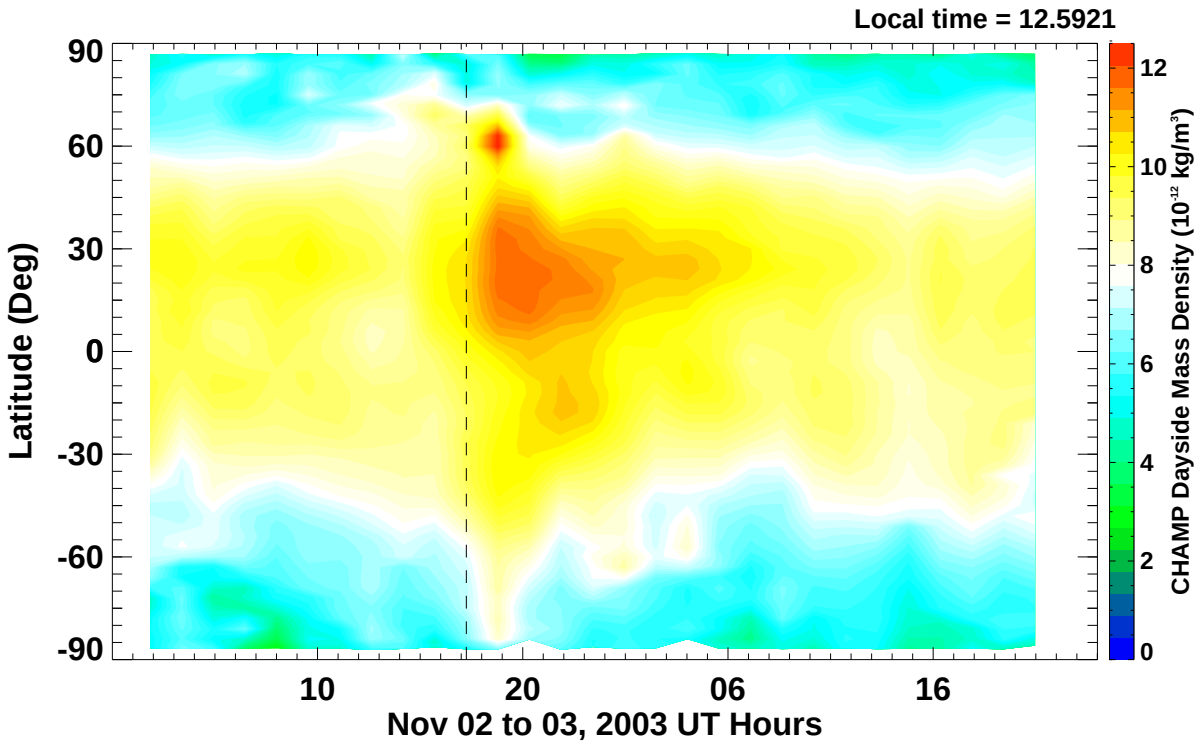

Figure 6.12: Champ neutral density throughout 11/2/2003.

$[O_2]$ results than it did for the November 2003 flares. GITM results show an orbit maximum increase at 387 km of 60% after the flare on the 7^{th}, and a 26% increase following the flare on the 9^{th}. As already discussed, GUVI also captures significant perturbations to the oxygen density during these time periods as well, but only at 387 km. Lower in the atmosphere, at 156 km, neither the model or GUVI show much of a perturbation following the onset of the flare. SABER, however, does show that there is a significant perturbation in the oxygen volume emission rate for several orbits following both the flare on the 7^{th} and the 9^{th} at 110 km, which the model does not capture. Given that SABER and GUVI are part of the same spacecraft, and, as shown in Figure 6.4, the two instruments sample the thermosphere in very similar locations, it is somewhat puzzling that one instrument captures the disturbance in the lower thermosphere while the other does not. This is further complicated by the fact that the GUVI and SABER instruments are in an orbit that reaches a lower SZA

in September 2005 than the orbit in November 2003 (Figure 6.3), yet, GUVI and SABER show disturbances following the 2003 events at all altitudes. The addition of energy to the thermosphere during a solar flare is greater at lower SZAs than at higher SZAs, therefore, the thermospheric response should also be greater at lower SZAs.

A comparison of the Champ observations between the 2003 and 2005 time periods indicates that the density response to flares is strongly dependent on solar zenith angle since, as shown in Figures 6.4 and 6.3, Champ samples lower SZAs during 2003. As discussed above, during the November 2003 events, Champ shows a perturbation, though it is washed out by the response of the system to a storm on the 4^{th}, following both of the flares. After the September 2005 events, Champ shows no perturbation at all (Figure 6.9). This is odd considering that, as just discussed, the GUVI [O_2] measurements show a perturbation at 387 km following the 2005 flares. This may be due to the fact that while the instruments are sampling similar solar zenith angles on the dayside, Champ is on the dusk side and GUVI is on the dawn side, so they are not sampling the same part of the thermosphere. However, things are made more confusing by GITM (which shows very little response to the 2003 events), showing a response of larger than 20% during the September 7, 2005 flare at the Champ location.

6.4 Discussion

This chapter makes use of measurements of mass density and oxygen number density and volume emission rates along with GITM results to provide an observational analysis of the thermospheric response to several solar flares. A summary of the observations and results are presented below.

- Following the November 2003 events,

- The observed [O_2] and O_2 volume emission rates are significantly enhanced at all altitudes during the orbit following the two largest flares.
- The Champ mass density results are perturbed following the flare on the 2^{nd}, but the response to the flare on the 4^{th} is washed out due to the thermosphere being in a perturbed state due to geomagnetic activity.
- GITM is affected by the flare, but the magnitudes of the perturbations are much smaller than the observations suggest, and difficult to distinguish from background fluctuations.

- Following the September 2005 events,
  - The observed [O_2] is enhanced at higher altitudes following the two largest flares, and GITM shows enhancements at the same locations and times.
  - The SABER O_2 volume emission rates are perturbed in the lower thermosphere following the two largest flares, but GITM is not perturbed at the same location and times.
  - Mass density observations show no response to the flare on the 7^{nd}, while GITM shows an enhancement, however, Champ observations do show a small enhancement to the flare on the 9^{th}, the magnitude of which is similar to the magnitude of the modeled perturbation.

The above results do not indicate that the thermosphere responds in a consistent manner to every solar flare. This behavior is not uncommon when using thermospheric measurements to study the response to transient events, especially flares. Several factors contribute to determine whether or not an instrument will detect a response following a solar flare and how strong the response will be. Another example is shown in Figures 6.13 and 6.14, where GUVI measurements of [O_2] and SABER measurements of NO volume emission rate are shown during an X7 flare that occurs

at 6:45 UT on January 20, 2005. The GUVI observations show a clear response to the solar flare during the orbit following the time at which the flare is launched. However, even though the SABER measurements are taken at relatively low SZA (38°–58°), there is little evidence to suggest that a flare has occurred in the NO volume emission rates.

Still, this study shows that observations of thermospheric mass density, oxygen densities, and oxygen emission rates can be significantly perturbed following a flare. Disturbances of several hundred percent can be observed in the oxygen densities in the day-side thermosphere. Unfortunately, when performing data analysis of solar flares, it is often that one instrument may measure perturbations to the system while another may not. In some cases, this may be because the instrument is at the wrong place at the wrong time. In other cases, it may be difficult to separate out the effects of other sources of dynamic forcing, such as high-latitude dynamics, in order to be able to quantify the response to the flare only. These issues, combined with the rarity of large solar flare events, makes statistical studies very difficult. Future "constellation" type missions will provide more extensive datasets with improved global coverage at higher time resolution. Such missions will make the data studies of solar flares much more tangible. In the meantime, better methods for separating out the effects of different drivers can make the data that is currently available more usable. Models are well suited for this, since there are many studies in the community that are focusing on studying how transient features such as storms affect the atmosphere. In the future, this knowledge can be applied to the datasets to remove the effects of the features other than those of interest, rendering many more usable observations of the system and increasing the size of the sample set for statistical studies.

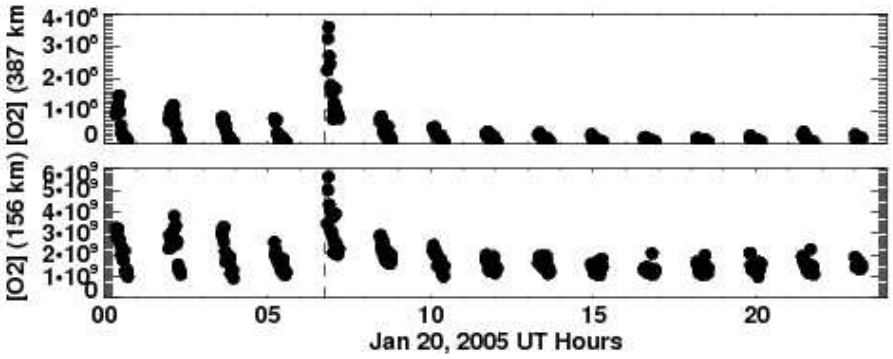

Figure 6.13: GUVI [O_2] observations at 387 (top) and 156 (bottom) on January 20, 2005

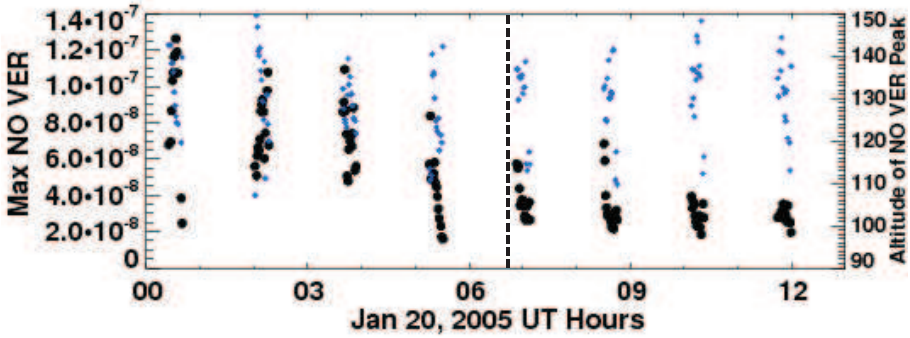

Figure 6.14: SABER NO volume emission rate observations on January 20, 2005. The measurements shown are obtained at SZAs between 38° and 58°.

CHAPTER VII

Conclusions

]The focus of this work is on describing the consequences of solar flares on the Earth's upper atmosphere, primarily through the use of the self consistent global circulation model, GITM. Specifically, this work discusses four main contributions to the aeronomy community.

1. During a solar flare, the thermospheric density can be significantly enhanced both on the day-side and the night-side, and the magnitude of the perturbation is dependent on altitude.

    - The increase in density is due to the absorption of excess solar radiation in the lower thermosphere, which causes the temperature to increase and therefore the atmosphere to expand. While most of the energy is being deposited below 200 km, enhanced upward velocities push dense air from below to higher altitudes.
    - At an altitude of 400 km, which approximately coincides with the altitude of the Champ satellite, GITM shows that the density can increase by almost 15% on the day-side in just over an hour.
    - As a result of the density perturbation, a traveling atmospheric disturbance (TAD) is launched which travels night-ward at the speed of sound plus the

background velocity. This TAD converges on itself in the midnight sector, and results in a density enhancement that is of the same magnitude as the day-side perturbation.

- The location of the night-side perturbation is determined by the background wind patterns. Specifically, the high-latitude convection patterns play a significant role on where the convergence will occur.
- Ultimately, localized perturbations of more than 5% can last 14 hours or more following a flare.

2. As a consequence of the neutral perturbations, the ionosphere can be highly affected in localized regions long after a flare occurs.

   - The neutral composition at F2 altitudes can be perturbed, resulting in changes in the O^+ recombination rate. This can cause significant enhancements of the peak electron density, and thus the TEC.
   - Strong vertical flows can develop on the night-side that can push the F2 peak to high altitudes, and in some cases out the top of the model.

3. Using synthesized solar flux measurements under theoretical conditions, the thermospheric response is characterized depending on the different features of a solar flare.

   - The manner in which the thermosphere responds to the total incident energy above background, flare magnitude, background-to-peak flux time, and decay time is quantified. GITM shows that:
     - The magnitude of the global response is linearly related on the total integrated energy above background incident into the atmosphere,
     - The magnitude of the global maximum perturbation is linearly depedent on energy, and also dependent on the flare magnitude.

- The decay time of a flare determines the time at which the maximum global perturbation will occur.
- The elapsed time between the background and maximum solar flux has little effect on the overall response of the system.

4. While in-depth statistical data analysis are shown to be extremely difficult, event based observations show that the neutral density can be perturbed by as much as 60% following a flare. Also, measurements of volume emission rates capture the response of the system to flares and can be used to show that the number density of O_2 can be enhanced by an order of magnitude at certain altitudes.

Ultimately, this work shows that large solar flares can play a significant role in determining the state of the upper atmosphere. While the perturbations from even the largest flares seen in the observations and model results are not as large as those that result from large geomagnetic storms, changes in neutral density of 60% can have a very significant effect on the velocity of a satellite in low-Earth orbit. In addition, because solar flares and geomagnetic storms are related and occur the most frequently during solar maximum, they often interact with the ionosphere-thermosphere system at similar times. Therefore, understanding how the thermosphere will react during a solar flare will allow work to be done in the future on the implications of preconditioning in the system. In other words, since multiple transient events may occur within hours of one another, the reponse of the thermosphere to repetitve events will be different than the response due to a single event, since the background state of the thermosphere affects the response. The possible effects of preconditioning were already very briefly discussed in Chapter VI, specifically in Figure 6.5. Global models, such as GITM, are well suited to begin to examine the effect of preconditioning on the system and theoretical studies have already begun to be performed using synthetic solar EUV data to examine the consequences of multiple solar flares being launched

on short time scales. Figure 7.1 shows a series of GITM simulations in which repetitve flares occur. For each simulation, a solar flare is launched on 1 of 6 time scales, from 1 hour to 18 hours. For example, the purple line shows the mass density global average percent difference at 400 km in response a solar flux that captures a solar flare occuring every hour beginning at 00 UT on the 21^{st} and ending at 12:00 UT on the 22^{nd}. The orange line shows the response to a solar flux that captures a solar flare occuring every 18 hours beginning and ending at the same times. Figure 7.1 shows that for repetitive events, the thermospheric density increases in a decaying manner as more and more energy is added to the system. Also, the thermosphere after a large solar flare seems to have a memory of roughly 12 hours, after which, if more energy is added to the system, the maximum global response will not continue to grow. This sort of preconditioning study is useful, also, to understand the difference between dynamic events that occur at solar maximum, when the background solar flux is high, vs. solar minimum, when the background flux is low. Ultimately, there must be some relationship between the background solar flux, background density, and the response to dynamic events, including solar flares and geomagnetic storms, and also transient events that are launched from the lower atmosphere. As the resolution of physics-based models becomes better, and the community's understanding of the system as a whole develops further, there will be increasing need for quantitative understanding of the response of the system to such dynamics at ever increasing scales. This work is part of that process, but as always, there is much more to do.

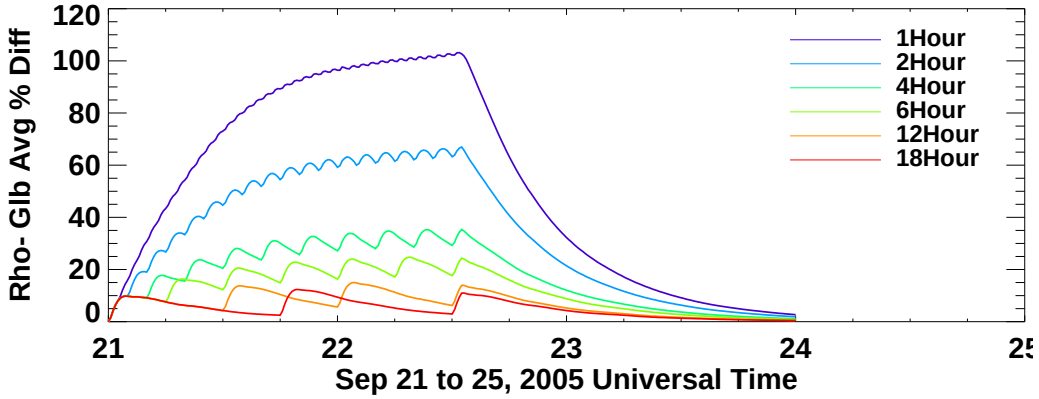

Figure 7.1: Density global average percent difference as the result of 6 different sets of repetitive solar flare events. Each event is made up of several solar flares that are launched every 1, 2, 4, 6, 12, and 18 hours, with the first flare beginning at 0 UT and the last one 36 hours later.

BIBLIOGRAPHY

BIBLIOGRAPHY

Afraimovich, E. L., A. T. Altynsev, V. V. Grechnev, and L. A. Leonovich (2001), Ionospheric effects of the solar flares as deduced from global GPS network data, *Advances in Space Research*, *27*, 1333–1338.

Blum, P. W., and K. G. H. Schuchardt (1978), Semi-theoretical global models of the eddy diffusion coefficient based on satellite data, *Journal of Atmospheric and Terrestrial Physics*, *40*, 1137–1142.

Brasseur, G., and D. Offermann (1986), Recombination of atomic oxygen near the mesopause Interpretation of rocket data, *J. Geophys. Res.*, *91*, 10,818–10,824, doi: 10.1029/JD091iD10p10818.

Brasseur, G., and Solomon (1986), *Aeronomy of the Middle Atmosphere*, Reidel, Hingham, Mass.

Brekke, A., J. R. Doupnik, and P. M. Banks (1974), Incoherent scatter measurements of E region conductivities and currents in the auroral zone, *J. Geophys. Res.*, *79*, 3773.

Burnside, R. G., C. A. Tepley, M. P. Sulzer, T. J. Fuller-Rowell, and D. G. Torr (1991), The neutral thermosphere at Arecibo during geomagnetic storms, *J. Geophys. Res.*, *96*, 1289–1301.

Chamberlin, P. C., T. N. Woods, and F. G. Eparvier (2007), Flare Irradiance Spectral Model (FISM): Daily component algorithms and results, *Space Weather*, *5*, 7005–+, doi:10.1029/2007SW000316.

Chandra, S., and A. K. Sinha (1973), The diurnal heat budget of the thermosphere, *Journal of Planetary and Space Sciences*, *21*, 593–604, doi:10.1016/0032-0633(73) 90072-X.

Chapman, S. (1931), The absorption and dissociative or ionizing effect of monochromatic radiation in an atmosphere on a rotating earth, *Proceedings of the Physical Society*, *43*, 26.

Christensen, A. B., et al. (1994), Global Ultraviolet Imager (GUVI) for the NASA Thermosphere-Ionsphere-Mesosphere Energetics and Dynamics (TIMED) mission, in *Proc. SPIE Vol. 2266, p. 451-466, Optical Spectroscopic Techniques and Instrumentation for Atmospheric and Space Research, Jinxue Wang; Paul B. Hays; Eds.*, edited by J. Wang and P. B. Hays, pp. 451–466.

Christensen, A. B., et al. (2003), Initial observations with the Global Ultraviolet Imager (GUVI) in the NASA TIMED satellite mission, *J. Geophys. Res.*, *108*, 16–1, doi:10.1029/2003JA009918.

Codrescu, M., T. Fuller-Rowell, R. Roble, and D. Evans (1997), Medium energy particle precipitation influences on the mesosphere and lower thermosphere, *J. Geophys. Res. in press.*

Codrescu, M. V., T. J. Fuller-Rowell, and J. C. Foster (1995), On the importance of E-field variability for Joule heating in the high-latitude thermosphere, *Geophys. Res. Lett.*, *22*, 2393.

Deng, Y., and A. J. Ridley (2006), Dependence of neutral winds on convection E-field, solar EUV, and auroral particle precipitation at high latitudes, *J. Geophys. Res.*, *111*, 9306, doi:10.1029/2005JA011368.

Deng, Y., A. D. Richmond, and A. J. Ridley (2008), Assessment of the non-hydrostatic effect on the upper atmosphere using a general circulation model (GCM), *Geophys. Res. Lett.*, *35*, doi: 10.1029/2007GL032,182.

Deng, Y., A. Maute, A. D. Richmond, and R. G. Roble (2009), Impact of electric field variability on Joule heating and thermospheric temperature and density, *Geophys. Res. Lett.*, *36*, 8105–+, doi:10.1029/2008GL036916.

Dickinson, R. E. (1984), Infrared radiative cooling in the mesosphere and lower thermosphere, *Journal of Atmospheric and Terrestrial Physics*, *46*, 995–1008.

Donnelly, R. F. (1976), Empirical models of solar flare X ray and EUV emission for use in studying their E and F region effects, *J. Geophys. Res.*, *81*, 4745–4753, doi:10.1029/JA081i025p04745.

Emery, B. A., I. G. Richardson, D. S. Evans, and F. J. Rich (2009), Solar wind structure sources and periodicities of auroral electron power over three solar cycles, *Journal of Atmospheric and Solar-Terrestrial Physics*, pp. 1–18, in press.

Evans, J. V. (1972), Ionospheric movements measured by incoherent scatter: A review, *Journal of Atmospheric and Terrestrial Physics*, *34*, 175–+.

Forbes, J. (2007), Dynamics of the thermosphere, *Journal of the Meteorological Society of Japan*, *85B*, 193–213.

Forbes, J. M., R. Gonzalez, F. A. Marcos, D. Revelle, and H. Parish (1996), Magnetic storm response of lower thermosphere density, *J. Geophys. Res.*, *101*, 2313–2320, doi:10.1029/95JA02721.

Foster, J. C., F.-P. S. Maurice, and V. J. Abreu (1983), Joule heating at high latitudes, *J. Geophys. Res.*, *88*, 4885.

Frahm, R. A., J. D. Winningham, J. R. Sharber, R. Link, G. Crowley, E. E. Gaines, D. L. Chenette, B. J. Anderson, and T. A. Potemra (1997), The diffuse aurora: A significant source of ionization in the middle atmosphere, *J. Geophys. Res.*, *102*, 28,203.

Fuller-Rowell, T. J., and D. Evans (1987), Height-integrated Pedersen and Hall conductivity patterns inferred from TIROS–NOAA satellite data, *J. Geophys. Res.*, *92*, 7606.

Fuller-Rowell, T. J., and D. Rees (1980), A three-dimensional, time-dependent, global model of the thermosphere, *J. Atmos. Sci.*, *37*, 2545.

Fuller-Rowell, T. J., and D. Rees (1992), Turbulent diffusion variability and implications for the upper thermosphere, *Advances in Space Research*, *12*, 45–56, doi:10.1016/0273-1177(92)90443-2.

Hall, C. M., C. E. Meek, A. H. Manson, and S. Nozawa (2008), Turbopause determination, climatology, and climatic trends using medium frequency radars at 52degN and 70degN, *Journal of Geophysical Research (Atmospheres)*, *113*, 13,104–+, doi: 10.1029/2008JD009938.

Hedin, A. (1991), Extension of the MSIS thermosphere model into the middle and lower atmosphere, *J. Geophys. Res.*, *96*, 1159.

Hernandez, G., R. G. Roble, E. C. Ridley, and J. H. Allen (1982), Thermospheric response observed over Fritz Peak, Colorado, during two large geomagnetic storms near solar cycle maximum, *J. Geophys. Res.*, *87*, 9181–9192.

Hinteregger, H. E., K. Fukui, and B. R. Gibson (1981), Observational, reference and model data on solar EUV from measurements on AE-E, *Geophys. Res. Lett.*, *8*, 1147.

Hundhausen, A. J. (1993), Sizes and locations of coronal mass ejections - SMM observations from 1980 and 1984-1989, *J. Geophys. Res.*, *98*, 13,177–+, doi: 10.1029/93JA00157.

Jeans, J. (1925), The Dynamical Theory of Gases, *4th Edition, Cambridge University Press*.

Jones, K. L., and H. Rishbeth (1971), The origin of storm increases of mid-latitude F-layer electron concentration., *Journal of Atmospheric and Terrestrial Physics*, *33*, 391–401.

Kamide, Y., and W. Baumjohann (1993), *Magnetosphere-Ionosphere Coupling*, Springer-Verlag Berlin Heidelberg New York. Volume 23.

Khazanov, G. V., M. W. Liemohn, T. S. Newman, M.-C. Fok, and R. W. Spiro (2003), Self-consistent magnetosphere-ionosphere coupling: Theoretical studies, *Journal of Geophysical Research (Space Physics)*, *108*, 1122–+, doi:10.1029/2002JA009624.

Killeen, T. L., et al. (1999), TIMED Doppler interferometer (TIDI), in *Proc. SPIE Vol. 3756, p. 289-301, Optical Spectroscopic Techniques and Instrumentation for Atmospheric and Space Research III, Allen M. Larar; Ed.*, edited by A. M. Larar, pp. 289–301.

Kim, Y., S. Eckermann, and H. Chun (2003), An overview of the past, present, and future of gravity-wave drag parametrization for numerical climate and weather prediction models: Survey article, *Canadian Meteorological and Oceanographic Society*, *41*.

Kivelson, M. G., and C. T. Russell (1995), *Introduction to Space Physics*, Cambridge University Press.

Kockarts, G. (1980), Nitric oxide cooling in the terrestrial thermosphere, *Geophys. Res. Lett.*, *7*, 137.

Kockarts, G. (1981), Effects of solar variations on the upper atmosphere, *ESLAB Symposium on Physics for Solar Variations*, *74*, 295–320.

Kockarts, G., and W. Peetermans (1970), Atomic oxygen infrared emission in the Earth's upper atmosphere, *Planet. Space Sci.*, *18*, 271.

Le, H., L. Liu, B. Chen, J. Lei, X. Yue, and W. Wan (2007), Modeling the responses of the middle latitude ionosphere to solar flares, *Journal of Atmospheric and Solar-Terrestrial Physics*, *69*, 1587–1598, doi:10.1016/j.jastp.2007.06.005.

Liu, H., H. Lühr, S. Watanabe, and C. Köhler, W. andManoj (2007), Contrasting behavior of the thermosphere and ionosphere in response to the 28 October 2003 solar flare, *Journal of Geophysical Research (Space Physics)*, *112*(A11), 7305–+, doi:10.1029/2007JA012313.

Lu, G., A. D. Richmond, B. A. Emery, and R. G. Roble (1995), Magnetosphere-ionosphere-thermosphere coupling: Effect of neutral winds on energy transfer and field-aligned current, *J. Geophys. Res.*, *100*, 19,643.

Lyon, J. G., S. H. Brecht, J. D. Huba, J. A. Fedder, and P. J. Palmadesso (1981), Computer simulation of a geomagnetic substorm, *Phys. Rev. Lett.*, *46*(15), 1038–1041, doi:10.1103/PhysRevLett.46.1038.

Marsh, D. R., S. C. Solomon, and A. E. Reynolds (2004), Empirical model of nitric oxide in the lower thermosphere, *Journal of Geophysical Research (Space Physics)*, *109*, 7301–+, doi:10.1029/2003JA010199.

Mayr, H. G., I. Harris, and N. W. Spencer (1978), Some properties of upper atmosphere dynamics., *Reviews of Geophysics and Space Physics*, *16*, 539–565.

Munro, R. H., J. T. Gosling, E. Hildner, R. M. MacQueen, A. I. Poland, and C. L. Ross (1979), The association of coronal mass ejection transients with other forms of solar activity, *Sol. Phys.*, *61*, 201–215, doi:10.1007/BF00155456.

Oberheide, J., and J. M. Forbes (2008), Tidal propagation of deep tropical cloud signatures into the thermosphere from TIMED observations, *Geophys. Res. Lett.*, *35*, 4816–+, doi:10.1029/2007GL032397.

Onsager, T. G., and M. Lockwood (1997), High-Latitude Particle Precipitation and its Relationship to Magnetospheric Source Regions, *Space Science Reviews*, *80*, 77–107, doi:10.1023/A:1004925720793.

Prölss, G. W., and M. J. Jung (1978), Travelling atmospheric disturbances as a possible explanation for daytime positive storm effects of moderate duration at middle latitudes, *Journal of Atmospheric and Terrestrial Physics*, *40*, 1351–1354.

Rees, M. H. (1989), *Physics and chemistry of the upper atmosphere*, Cambridge University Press, New York, NY, 10022, USA.

Reigber, C., H. Luhr, and P. Schwintzer (2000), CHAMP mission status and perspectives, in *Suppl to EOS, Transactions, AGU, 81(48), F307.*

Richards, P. G., and D. G. Torr (1984), An investigation of the consistency of the ionospheric measurements of the photoelectron flux and solar EUV flux, *J. Geophys. Res.*, *89*, 5625.

Richards, P. G., J. A. Fennelly, and D. G. Torr (1994), EUVAC: A solar EUV flux model for aeronomic calculations, *J. Geophys. Res.*, *99*, 8981.

Ridley, A. J. (2005), A new formulation for the ionospheric cross polar cap potential including saturation effects, *Annales Geophysicae*, *23*, 3533–3547.

Ridley, A. J., Y. Deng, and G. Toth (2006), The global ionosphere-thermosphere model, *J. Atmos. Sol-Terr. Phys.*, *68*, 839.

Roble, R. G., J. M. Forbes, and F. A. Marcos (1987), Thermospheric dynamics during the March 22, 1979, magnetic storm. I - Model simulations. II - Comparisons of model predictions with observations, *J. Geophys. Res.*, *92*, 6045–6081, doi:10.1029/JA092iA06p06045.

Roble, R. G., E. C. Ridley, and R. E. Dickinson (1987), On the global mean structure of the thermosphere, *J. Geophys. Res.*, *92*, 8745.

Roble, R. G., E. C. Ridley, A. D. Richmond, and R. E. Dickinson (1988), A coupled thermosphere/ionosphere general circulation model, *Geophys. Res. Lett.*, *15*, 1325.

Russell, J. M., M. G. Mlynczak, L. L. Gordley, J. J. Tansock, and R. W. Esplin (1999), Overview of the SABER experiment and preliminary calibration results, in *Proc. SPIE Vol. 3756, p. 277-288, Optical Spectroscopic Techniques and Instrumentation for Atmospheric and Space Research III, Allen M. Larar; Ed.*, edited by A. M. Larar, pp. 277–288.

Sauvaud, J. A., J. P. Treilhou, A. Saint-Marc, J. Dandouras, and H. Reme (1987), Large scale response of the magnetosphere to a southward turning of the interplanetary magnetic field, *J. Geophys. Res.*, *92*, 2365–2376, doi:10.1029/JA092iA03p02365.

Schunk, R. W., and A. F. Nagy (2000), *Ionospheres*, Cambridge Press, Cambridge University.

Sinha, A. K., and S. Chandra (1974), Seasonal and magnetic storm related changes in the thermosphere induced by eddy mixing, *Journal of Atmospheric and Terrestrial Physics*, *36*, 2055–2066.

Solomon, S. C., and L. Qian (2005), Solar extreme-ultraviolet irradiance for general circulation models, *J. Geophys. Res.*, *110*, doi:10.1029/2005JA011,160.

Solomon, S. C., C. A. Barth, and S. M. Bailey (2001), Auroral production of nitric oxide measured by the SNOE Satellite, *Geophys. Res. Lett.*, *26*, 1259.

Stolarski, R. S. (1976), Energetics of the midlatitude thermosphere, *J. Atmos. Terr. Phys.*, *38*, 863.

Sutton, E. K., J. M. Forbes, and R. S. Nerem (2005), Global thermospheric neutral density and wind response to the severe 2003 geomagnetic storms from CH AMP accelerometer data, *J. Geophys. Res.*, *110*, 9–+, doi:10.1029/2004JA010985.

Sutton, E. K., J. M. Forbes, R. S. Nerem, and T. N. Woods (2006), Neutral density response to the solar flares of October and November, 2003, *Geophys. Res. Lett.*, *33*, 22,101–+, doi:10.1029/2006GL027737.

Thayer, J. P., J. Lei, F. J.M., E. Sutton, and R. Nerem (2008), Thermospheric density oscillations due to periodic solar wind high speed streams, *J. Geophys. Res.*, *113*, A06,307.

Tinsley, B. A., R. R. Hodges, Jr., and R. P. Rohrbaugh (1986), Monte Carlo models for the terrestrial exosphere over a solar cycle, *J. Geophys. Res.*, *91*, 13,631–13,647, doi:10.1029/JA091iA12p13631.

Tobiska, W. K. (1991), Revised solar extreme ultraviolet flux model, *J. Atm. Terr. Phys.*, *53*, 1005.

Tobiska, W. K., T. Woods, F. Eparvier, R. Viereck, L. Floyd, D. Bouwer, G. Rottman, and O. R. White (2000), The SOLAR2000 empirical solar irradiance model and forecast tool, *J. Atm. Solar Terr. Phys.*, *62*, 1233.

Torr, D. G., M. R. Torr, J. C. G. Walker, L. H. Brace, H. C. Brinton, W. B. Hanson, J. H. Hoffman, A. O. Nier, and M. Oppenheimer (1976), Recombination of NO+ in the ionosphere, *Geophys. Res. Lett.*, *3*, 209–212, doi:10.1029/GL003i004p00209.

Torr, D. G., M. R. Torr, P. G. Richards, and V. J. Abreu (1981), Further quantification of the sources and sinks of thermospheric O/1D/ atoms, *Planet. Space Sci.*, *29*, 595–600, doi:10.1016/0032-0633(81)90107-0.

Torr, D. G., et al. (1979), An experimental and theoretical study of the mean diurnal variation of O^+, NO^+, O_2^+, and N_2^+ ions in the mid-latitude F_1 layer of the ionosphere, *J. Geophys. Res.*, *84*, 3360.

Torr, M., P. G. Richards, and D. G. Torr (1980), A new determination of the ultraviolet heating efficiency, *J. Geophys. Res.*, *85*(A12), 6819.

Torr, M. R., and D. G. Torr (1982), The role of metastable species in the thermosphere, *Reviews of Geophysics and Space Physics*, *20*, 91–144.

Tsurutani, B. T., et al. (2005), The October 28, 2003 extreme EUV solar flare and resultant extreme ionospheric effects: Comparison to other Halloween events and the Bastille Day event, *Geophys. Res. Lett.*, *32*, 3–+, doi:10.1029/2004GL021475.

Uritsky, V., M. Pudovkin, and A. Steen (2001), Geomagnetic substorms as perturbed self-organized critical dynamics of the magnetosphere, *Journal of Atmospheric and Solar-Terrestrial Physics*, *63*, 1415–1424, doi:10.1016/S1364-6826(00)00243-1.

Vickrey, J. F., R. R. Vondrak, and S. J. Matthews (1982), Energy deposition by precipitating particles and Joule dissipation in the auroral ionosphere, *J. Geophys. Res.*, *87*, 5184.

Walterscheid, R. L., G. Schubert, and D. G. Brinkman (2001), Small-scale gravity waves in the upper mesosphere and lower thermosphere generated by deep tropical convection, *J. Geophys. Res.*, *106*, 31,825–31,832, doi:10.1029/2000JD000131.

Weimer, D. R. (1995), Models of high-latitude electric potentials derived with a least error fit of spherical harmonic coefficients, *J. Geophys. Res.*, *100*, 19,595.

Weimer, D. R. (1996), A flexible, IMF dependent model of high-latitude electric potential having "space weather" applications, *Geophys. Res. Lett.*, *23*, 2549.

Winningham, J. D., D. T. Decker, J. U. Kozyra, A. F. Nagy, and J. R. Jasperse (1989), Energetic (above 60 eV) atmospheric photoelectrons, *J. Geophys. Res.*, *94*, 15,335–15,348, doi:10.1029/JA094iA11p15335.

Woods, T., and G. Rottman (2002), Solar ultraviolet variability over time periods of aeronomic interest, *Atmospheres in the Solar System: Comparative Aeronomy, Geophys. Monogr. Ser.*, *130*, 221.

Woods, T. N., G. J. Rottman, S. M. Bailey, S. C. Solomon, and J. R. Worden (1998), Solar Extreme Ultraviolet Irradiance Measurements During Solar Cycle 22, *Sol. Phys.*, *177*, 133–146.

Woods, T. N., F. G. Eparvier, J. Fontenla, J. Harder, G. Kopp, W. E. McClintock, G. Rottman, B. Smiley, and M. Snow (2004), Solar irradiance variability during the October 2003 solar storm period, *Geophys. Res. Lett.*, *31*, 10,802–+, doi:10.1029/2004GL019571.

Woods, T. N., F. G. Eparvier, S. M. Bailey, P. C. Chamberlin, J. Lean, G. J. Rottman, S. C. Solomon, W. K. Tobiska, and D. L. Woodraska (2005), Solar EUV Experiment (SEE): Mission overview and first results, *J. Geophys. Res.*, *110*, 1312–+, doi:10.1029/2004JA010765.

Zhou, X., and B. T. Tsurutani (2001), Interplanetary shock triggering of nightside geomagnetic activity: Substorms, pseudobreakups, and quiescent events, *J. Geophys. Res.*, *106*, 18,957–18,968, doi:10.1029/2000JA003028.